Ice shelf-ocean interactions in a general circulation model: melt-rate modulation due to mean flow and tidal currents

by

Veronique Dansereau

Submitted in partial fulfillment of the requirements for the degree of
Master of Science
at the
MASSACHUSETTS INSTITUTE OF TECHNOLOGY
and the
WOODS HOLE OCEANOGRAPHIC INSTITUTION

September 2012

Signature of Author

Joint Program in Physical Oceanography - MIT/ WHOI
August 27, 2012

Certified by

Patrick Heimbach
Principal Research Scientist in the Earth, Atmospheric and Planetary Science Department, MIT
Thesis Supervisor

Accepted by

Karl R. Helfrich
Senior Scientist, Woods Hole Oceanographic Institution
Chair of the Joint Program in Physical Oceanography

Acknowledgements

I thank my supervisor, Patrick Heimbach, for all his help and good advices regarding this research. I thank the National Science and Engineering Research Council of Canada for their financial support through the PGS Doctoral Research scholarship. I also thank Louis-Philippe Nadeau for his never-failing support over the past two years. Equally important was the company of Ginette, to whom I dedicate this thesis.

Ice shelf-ocean interactions in a general circulation model: melt-rate modulation due to mean flow and tidal currents

by

Veronique Dansereau

Submitted to
the Department of Earth, Atmospheric and Planetary Sciences at MIT
and to the Woods Hole Oceanographic Institution
on August 28, 2012
in Partial Fulfillment of the Requirements for the Degree of
Master of Science in Physical Oceanography

ABSTRACT

Interactions between the ocean circulation in sub-ice shelf cavities and the overlying ice shelf have received considerable attention in the context of observed changes in flow speeds of marine ice sheets around Antarctica. Modeling these interactions requires parameterizing the turbulent boundary layer processes to infer melt rates from the oceanic state at the ice-ocean interface. Here we explore two such parameterizations in the context of the MIT ocean general circulation model coupled to the z-coordinates ice shelf cavity model of Losch (2008). We investigate both idealized ice shelf cavity geometries as well as a realistic cavity under Pine Island Ice Shelf (PIIS), West Antarctica. Our starting point is a three-equation melt rate parameterization implemented by Losch (2008), which is based on the work of Hellmer and Olbers (1989). In this form, the transfer coefficients for calculating heat and freshwater fluxes are independent of frictional turbulence induced by the proximity of the moving ocean to the fixed ice interface. More recently, Holland and Jenkins (1999) have proposed a parameterization in which the transfer coefficients do depend on the ocean-induced turbulence and are directly coupled to the speed of currents in the ocean mixed layer underneath the ice shelf through a quadratic drag formulation and a bulk drag coefficient. The melt rate parameterization in the MITgcm is augmented to account for this velocity dependence.

First, the effect of the augmented formulation is investigated in terms of its impact on melt rates as well as on its feedback on the wider sub-ice shelf circulation. We find that, over a wide range of drag coefficients, velocity-dependent melt rates are more strongly constrained by the distribution of mixed layer currents than by the temperature gradient between the shelf base and underlying ocean, as opposed to velocity-independent melt rates. This leads to large differences in melt rate patterns under PIIS when including versus not including the velocity dependence. In a second time, the modulating effects of tidal currents on melting at the base of PIIS are examined. We find that the temporal variability of velocity-dependent melt rates under tidal forcing is greater than that of velocity-independent melt rates. Our experiments suggest that because tidal currents under PIIS are weak and buoyancy fluxes are strong, tidal mixing is negligible and tidal rectification is restricted to very steep bathymetric features, such as the ice shelf front. Nonetheless, strong tidally-rectified currents at the ice shelf front significantly increase ablation rates there when the formulation of the transfer coefficients includes the velocity dependence. The enhanced melting then feedbacks positively on the rectified currents, which are susceptible to insulate the cavity interior from changes in open ocean conditions.

Thesis Supervisor: Patrick Heimbach
Title: Principal Research Scientist in the Department of Earth, Atmosphere and Planetary Sciences at MIT

Table of Contents

List of Tables

List of Figures

1 Introduction

Satellite data that have become available since the early 1990s, including interferometric SAR (InSAR) from ERS-1/2, laser altimetry from ICESat-1, and gravimetry from GRACE, reveal large changes of the Greenland and Antarctic ice sheets in terms of increased flow speed, thinning, and mass loss. These changes are mostly confined to the ice sheets' marine margins, suggesting an important role of the ocean as a trigger. In a recent study combining ICESat satellite laser altimetry analysis with surface firn modeling, Pritchard et al. (2012) suggested that increased basal melt acts as the primary control of Antarctic ice sheet mass loss through reduction in buttressing and acceleration of glacier flow. An important point stressed in their work is the strongly regional distribution of Antarctic ice-shelf thinning. Between 2003 and 2008, thinning was the most rapid (up to 6.8 m/yr) along the Amundsen and Bellingshausen Sea coasts. During this period, a positive contribution to glacier mass balance by the thickening of the firn layer and increased influx from glacier tributaries was observed over these regions and ice shelf fronts either maintained their position or advanced. Pritchard et al. (2012) therefore concluded that the regional thinning there must be caused by increased basal melt driven by ice shelf-ocean interactions.

Thinning by basal melt implies the availability of ocean heat. For the ice shelves of the Amundsen and Bellingshausen Seas, this heat is provided by the incursions of relatively warm, salty Circumpolar Deep Waters (CDW) sitting at depth across the continental shelf (Thoma et al., 2008; Jacobs et al., 2011; Pritchard et al., 2012). With temperatures reaching over 1°C, these waters are warmer than that over most other regions of the Antarctic continental shelf (Jacobs and Hellmer, 1996) by more than 2°C. In particular, the strongest thermal forcing is observed at the base of Pine Island Ice Shelf (PIIS), West Antarctica (Rignot and Stanley, 2002; Joughin et al., 2010; Jacobs et al., 2011; Pritchard et al., 2012). At its deepest point, the grounding line of PIIS reaches depths greater than 800 meters. Because of the pressure dependence of the freezing point, CDW there can be up to 4°C above the ice shelf base temperature and hence trigger fast melting (Jacobs and Hellmer, 1996).

Recently, many studies have focussed on making reliable estimates of the total melt rates under PIIS, which is particularly important to assess the contribution of the ice shelf to sea level rise. However, other studies have indicated that estimates of the spatial pattern of melt rates are critical as well for reliable predictions of ablation rates (Payne et al., 2007; Jacobs et al., 2011). Jacobs et al. (2011) in particular suggested that the distribution of melting has a greater impact than its areal average on the cavity shape. Their observational study indicated an increase between 1999 and 2004 of about 6% in the difference in temperature between the ice interface and the ocean just below that is consistent with a warming of CDW outside the cavity. The authors pointed out that this warming is small compared to the 77% increase in the strength of the circulation under PIIS and the 50% increase in meltwater production observed over the same period. These results suggest that the internal cavity dynamics is at least as important and perhaps dominant over conditions of the far field ocean in controlling the ice shelf mass balance. Jacobs et al. (2011) justified this through a feedback between increased melting, steepening of the ice shelf base at the grounding line, retreat of the grounding line downstream of grounding sills, changes in cavity circulation and access of warm waters to deeper reaches of the ice shelf base.

Major lines of research in the field of ice shelf-ocean interactions are currently concerned with the questions of (1) the connection between basin-scale water mass variability (e.g., CDW, in the Southern Ocean) and sub-ice shelf water mass properties, (2) circulation within the sub-ice shelf cavity and its impact on ice shelf melt rates, (3) boundary layer processes at the ice-ocean interface and their impact on melt rate magnitudes, (4) the relationship between cavity geometry, cavity circulation, and melt rate magnitudes. All these issues are crucial in developing models or model parameterizations which are suitable for climate simulations.

The ocean circulation inside ice shelf cavities is governed to a large extent by phase change processes occurring within a shallow ocean boundary layer at the ice shelf base. Turbulent mixing is identified as the critical process by which the ocean currents and sensible heat content are translated into the phase changes that control both the mass balance of the ice shelf and the buoyancy forcing on the cavity circulation (Holland and Jenkins, 1999; Jenkins et al., 2010b). From a modeling perspective, most approaches lack the ability to resolve the turbulent boundary processes. Hence turbulence closure schemes, i.e. parameterizations of these fluxes are required to infer melt rates. Since deployment of necessary instrumentation right at the base of hundreds of meters thick ice shelves is a serious technological challenge, turbulent fluxes near the ice-ocean interface have not yet been directly measured (Jenkins et al., 2010b) and the parameterizations in use remain highly uncertain.

The turbulence closure employed in most models is based on a standard approach in which fluxes are related to spatial gradients of temperature and salinity via bulk transfers velocities γ. The simplest (and earliest) parameterizations use constant heat and freshwater turbulent transfer velocities γ_T and γ_S for heat and freshwater (eg., Hellmer and Olbers, 1989; Determann and Gerdes, 1994; Grosfeld and Gerdes, 1997), which amounts to assuming a temporally and spatially uniform ocean velocity at the ice shelf base. The only direct forcing on melt rates in this case is the gradient in temperature between the ice interface at the local freezing point and the ocean just below that drives the diffusive heat fluxes through the ocean-boundary layer. With this formulation, melt rates are strongly constrained by the distribution of the shelf base depth which sets the pressure freezing point. On the other hand, ocean currents are the dominant physical driver of the turbulence responsible for the heat and salt transfers at the ice shelf base. Tides in particular are though to be a major source of turbulent kinetic energy in ice shelf cavities (MacAyeal, 1984a,b,c, 1985; Holland, 2008; Jenkins et al., 2010b; Mueller et al., 2012; Makinson et al., 2012). In the constant turbulent transfer velocities parameterization of melt rates, ocean currents have no direct control on distribution of phase changes.

A more realistic parameterization of the turbulent heat and salt exchanges consists in letting γ_T, γ_S depend on a friction velocity, which is defined in terms of the kinematic stress at the ice-ocean interface and directly related to current velocity through a quadratic law involving a constant drag coefficient (Jenkins, 1991; Holland and Jenkins, 1999; Jenkins et al., 2010b). Such a parameterization is inspired from formulations employed in models of sea ice-ocean interactions and is motivated by relatively extensive measurements of turbulence underneath sea ice (McPhee et al., 1987). Because no such observations are yet available for shelf ice, parameter values used in this velocity-dependent formulation, in particular, the drag coefficient, have been adopted from the sea ice modeling community. The use of this parameterization begs important questions:

- what determines the magnitude of the velocity in the boundary layer and how does it relate to the buoyant melt water plume rising from the shelf base to the surface,
- what is the role of tides in modulating ocean current velocities and the spatial distribution of melt rates in the cavity,
- how are the boundary layer velocity, hydrographic properties and melt rate distribution influenced by the large and smaller scale cavity circulations,
- which role plays cavity geometry, i.e., the slope of the ice shelf base and of the bedrock, in the redistribution of melt rates in the cavity,
- to which extent are the parameters originally inferred from sea ice measurements suitable for sub-ice shelf conditions.

This study addresses these questions in the context of the MIT ocean general circulation model (MITgcm), the first z-coordinate ocean model enabling representation of circulation in sub-ice shelf cavities. The implementation uses the hydrostatic and Boussinesq approximations, along with partial cells to accurately represent both bottom and ice shelf topographies. Both idealized and realistic configurations of the ice shelf cavity underneath Pine Island Glacier are investigated. The melt rate parameterization originally implemented in the MITgcm (Losch, 2008) is based on constant turbulent transfer velocities for both temperature and salinity. The starting point of this work is therefore the implementation of a velocity-dependent form of the turbulent transfer velocities parameterization that follows the work of Jenkins (1991) and Holland and Jenkins (1999).

Preliminary goals of this modeling work are to identify differences in melting patterns associated with the use of a velocity-dependent versus a velocity-independent formulation of the turbulent heat and salt exchanges through the ice-ocean boundary layer and to understand the physical processes responsible for circulation changes resulting from the choice of either parameterization in both the idealized ice shelf and realistic PIIS model setups. In particular, we aim to identify potential feedback mechanisms between ablation rates, circulations, meltwater plume velocities, cavity geometry and transfer coefficients. Topographical constraints on the melt rates and cavity circulation have been discussed notably by Determann and Gerdes (1994) and Grosfeld and Gerdes (1997) and more extensively by Little et al. (2008), however only in the context of a velocity-independent melt rate parameterization. It is reasonable to think that feedbacks between these constraints and the dynamics-thermodynamics processes in the cavity would be modified or at least enhanced when coupling directly melt rates and ocean velocities. This hypothesis is verified here by comparing idealized simulations in which the ice shelf bathymetry and bedrock topography are varied. At small scales, the impact of surface roughness on melt rates and the cavity circulation is another unknown, which requires sensitivity experiments of the associated drag coefficient (McPhee et al., 1987). Here, these experiments are conducted using first the idealized and secondly the more realistic PIIS cavity configuration, to identify possible differences in the model's response to changes in frictional drag associated with more complex ice shelf and bedrock topography. Lastly, the modulating effects of tides on the melt rates and cavity circulation are investigated. In the case of 'cold' ice shelves that enter in contact with High Salinity Shelf Waters (HSSW) of about $-1°C$ in temperature such as Filchner-Ronne Ice Shelf (FRIS) (King et al., 2011; Makinson et al., 2011, 2012), Ross Ice Shelf (MacAyeal, 1984a,b,c, 1985; Holland, 2008), Larsen C Ice Shelf (King et al., 2011; Mueller et al., 2012), such modulating impacts are relatively well documented. However, much less is known about the impacts of tides on 'warm' ice shelves forced with strong buoyancy fluxes such as that of the Amundsen and Bellingshausen Seas. Both the particular case of PIIS and the general case of 'warm' ice shelves are addressed here by conducting experiments in which the PIIS model forced with realistic tidal currents and others in which the idealized model is forced with tidal currents of varying amplitude.

We begin in section 2 by reviewing the theory of the velocity-dependent and velocity-independent parameterizations of ablation rates. The topographical constrains on the cavity dynamics identified in earlier studies are mentioned and the processes by which tides can modulate the melt rates and cavity circulations are described. In the following section (3), the MIT general circulation model and its ice shelf cavity component are described along with the specific model setups used in this study. Results are presented in section 4 for (4.1) the comparison of simulations using the velocity-dependent and velocity-dependent melt rate parameterizations, (4.2) the drag coefficient sensitivity experiments, (4.3) the shelf base and bedrock topography sensitivity experiments and (4.4) the tidally forced experiments. The main observations and conclusions drawn from this study are summarized in section 5.

2 The three-equation model

In regional-scale three-equations ice shelf cavity models, ice-ocean thermodynamics interactions are formulated in terms of the physical properties over three distinguished regions: the ice shelf, the boundary layer, at the ice shelf base, and the ocean mixed layer.

The boundary layer can be divided conceptually into two regions based on the physical process locally governing turbulent mixing. Closest to the ice interface, over a layer a few millimeters to a few centimeters thick referred to as the 'interfacial' or 'viscous' sublayer (Jenkins, 1991; Holland and Jenkins, 1999; Jenkins et al., 2010b), turbulent diffusivity is suppressed and hence turbulent transfers are dominated by molecular diffusion. Just outside this sublayer lies a layer a few meters thick over which turbulent diffusivity resulting from the proximity of the moving ocean to the ice boundary is the primary source of mixing. Because seawater has a high molecular Prandtl number and a very high Schmidt number, temperature and salinity gradients between the ice shelf base and the far field are largely confined to the viscous sublayer and transfers through the ice ocean-boundary layer show relatively little sensitivity to the treatment of mixing outside this layer (McPhee et al., 1987). However, as typical regional-scale three-equation models resolve neither this layer nor the viscous sublayer, hydrographic properties over the boundary layer are assumed uniform and equal to the properties of the ocean at the ice shelf base. Just outside the boundary layer lies a mixed layer typically tens of meters thick. Ocean properties over this region are not affected by the presence of the ice interface but are well mixed under the influence of rotation and buoyancy processes. Hydrographic conditions of the mixed layer are sometimes referred to as the 'far-field' conditions (Holland and Jenkins, 1999). Table 1 list the variables and constants relevant to the thermodynamic processes in these three model constituents.

The fundamental underlying assumption of the three-equation formulation of ice shelf-ocean interactions is that phase changes at the ice-ocean boundary occur in thermodynamic equilibrium (Jenkins, 1991; Jenkins et al., 2010b; Holland and Jenkins, 1999, 2001; Hellmer and Olbers, 1989; Determann and Gerdes, 1994; Grosfeld and Gerdes, 1997). This constrains the ice-ocean interface to be at the local freezing point, thereby allowing the temperature and salinity at the ice shelf base to be always related by an expression for the freezing point as a function of salinity and pressure. This requirement links balances of heat and salt at the interface and and closes a three-equation system formed by :

1. **a heat conservation equation;**

   Conservation of heat at the ice-ocean interface requires that the divergence of the heat flux be balanced by the sources or sinks of latent heat associated with freezing or melting, Q^T_{latent}. The flux of heat is the sum of two contributions: the diffusion of heat across the ice-ocean boundary layer, driven by gradients of temperature between the mixed layer and the local freezing point, Q^T_M and the molecular conduction of heat through the ice shelf, which is induced by the gradient of ice temperature at the base of the shelf, Q^T_I. The heat conservation equation therefore reads:

   $$Q^T_I - Q^T_M = Q^T_{latent}, \tag{1}$$

   with

   $$Q^T_{latent} = -L_f \rho_M m,^1 \tag{2}$$

   where L_f is the latent heat of fusion/melting of ice, ρ_M, the ocean mixed layer density and m, the melt rate.

[1] Q^T_M, Q^T_{latent} and Q^T_I have dimensions of heat flux per unit volume (J ms^{-1} m^{-3} or Wm^{-2}).

2. **a salt conservation equation;**

   Conservation of salt requires that the freshwater (brine) flux associated with the phase changes at the ice shelf base, Q^S_{brine} be balanced by the diffusive flux of freshwater (salt) at the ice-ocean interface. In theory, pockets of salt get entrapped when seawater is refreezing as marine ice, resulting in a non-zero ice shelf salinity. However, observations revealing very low salinities[2] of marine ice at the base of ice shelves suggest that setting the ice salinity S_I to zero is a reasonable approximation. The flux of freshwater (salt) at the ice-ocean interface is the sum of the molecular diffusive flux of freshwater (salt) into the ice Q^S_I, and of the diffusive freshwater (salt) flux through the ice-ocean boundary layer driven by the gradient of salinity between the ocean mixed layer and the ice shelf base, Q^S_M:

$$Q^S_I - Q^S_M = Q^S_{brine},$$

   with the freshwater (salt) flux at the ice shelf base being the flux of freshwater (brine) produced (rejected) by melting of ice of salinity S_I (refreezing of water of salinity S_B),

$$Q^S_{brine} = \rho_M m(S_I - S_B). \tag{3}$$

   Q^S_I, the salt diffusivity through ice, being practically zero Holland and Jenkins (1999), the salt conservation equation simplifies to

$$Q^S_M = \rho_M m S_B.^3 \tag{4}$$

   The melt rate, m, in equations (2) and (3) is expressed in terms of the thickness of the ablated or accumulated ice layer at the base of the ice shelf per unit of time.

3. **an expression for the freezing point temperature:**

   The freezing point of sea water is, to first order, a linear function of pressure. It is also a weakly non-linear function of salinity. Some models solve the three-equation system expressing the non-linear relationship between T_B and S_B (eg., the Ice-Shelf Ocean Model Intercomparison Project (ISOMIP) models), but many others (eg., Hellmer and Olbers, 1989; Jenkins, 1991; Holland and Jenkins, 1999, 2001; Holland and Feltham, 2006; Little et al., 2008; Losch, 2008; Jenkins et al., 2010b; Mueller et al., 2012) instead use a simpler linearized function for $T_B(p_B, S_B)$ of the form

$$T_{freeze} = T_B(p_B, S_B) = aS_B + bp_B + c, \tag{5}$$

   with a b and c being empirical constants. In particular, the model of Losch (2008) uses such a linearized equation, with a salinity coefficient $a = -0.0575°\text{C psu}^{-1}$, a pressure coefficient $b = -7.61 \cdot 10^{-4}°\text{C Pa}^{-1}$, and $c = 0.0901$.

In ice shelf-ocean coupled models, mixed layer properties are calculated through the specific formulation of the ocean model. Ice shelf properties are either prescribed (as done here) or calculated through coupling with a dynamic ice sheet model. The three remaining unknowns that need to be solved for are

- the temperature at the ice-ocean interface, T_B,
- the salinity at the ice-ocean interface, S_B,

[2] 0.025 psu (Eicken et al., 1994)

[3] Q^S_M has dimensions of a flux of mass of salt per unit volume (psu $\cdot$ kg ms^{-1} m^{-3}).

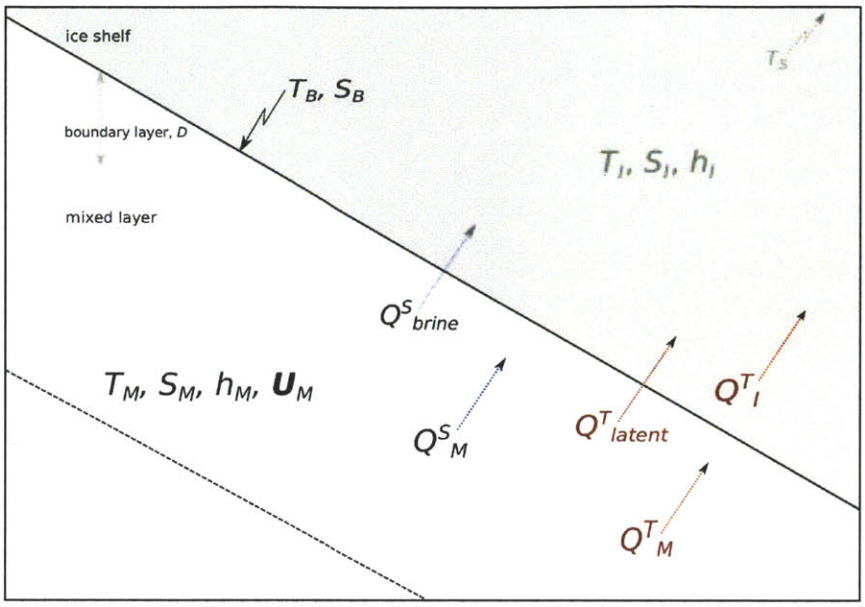

Figure 1: Schematic representation of the heat and salt balances at the base of an ice shelf, as formulated in the model of Holland and Jenkins (1999). The diagram represents an ice shelf of thickness h_I (dark grey shaded area), an ice-ocean boundary layer of thickness D at the ice shelf base and a mixed layer outside the boundary layer with depth equal to one vertical level ($\Delta z = 20$ m in the present model configuration). In the MITgcm model with ice shelf component of Losch (2008) used here, the sign convention is such that a positive (upward) heat flux through the boundary layer leads to melting (latent heat flux into the ice shelf) and a conductive heat flux into the ice shelf (upwards). Melting results in a downward (negative) freshwater flux (or positive upward brine flux) trough the mixed layer.
Adapted from Holland and Jenkins (1999).

- the melt rate, m.

In the three-equation model, the ice-ocean interaction problem is therefore reduced to estimating the diffusive heat and freshwater fluxes, Q_M^T and Q_M^S, resulting from spatial gradients of temperature and salinity between the ocean mixed layer and the ice interface. These fluxes are parameterized in terms of the gradients in mixed layer temperature and salinity at the ice shelf base and of the thermal and salinity diffusivity $\kappa_M^{T,S}$:

$$Q_M^T = -\rho_M c_{p\,M} \kappa_M^T \left.\frac{\partial T_M}{\partial z}\right|_B ,$$

$$Q_M^S = -\rho_M \kappa_M^S \left.\frac{\partial S_M}{\partial z}\right|_B ,$$

where ρ_M and $c_{p\,M}$ are the constant density and heat capacity of the mixed layer respectively. When assuming a laminar boundary layer, the heat and salinity gradients at the ice shelf base can take the simple form

$$\frac{T_B - T_M}{D},$$

and

$$\frac{S_B - S_M}{D}$$

with D the thickness of the boundary layer. This formulation is obviously inadequate for the turbulent ice-ocean boundary layer, in which the temperature and salinity profiles, hence the heat and salt diffusivities, are variable. However, the turbulence-induced variability of the diffusivities are easily parameterized through the

use of a non-dimensional Nusselt number, Nu [4] :

$$Q_M^T = -\rho_M c_{pM} \frac{\mathrm{Nu}\kappa_M^T}{h}(T_B - T_M), \tag{6}$$

$$Q_M^S = -\rho_M \frac{\mathrm{Nu}\kappa_M^S}{D}(S_B - S_M). \tag{7}$$

The factors $\frac{\mathrm{Nu}\kappa_M^T}{D}$ and $\frac{\mathrm{Nu}\kappa_M^S}{h}$ have dimensions of velocity and are referred to respectively as the turbulent heat and salt exchange velocities, γ_T and γ_S (hereinafter, $\gamma_{T,S}$). Differences between three-equation models reside in the level of sophistication with which these exchange velocities are parameterized. Below we discuss the two main approaches currently taken to formulate $\gamma_{T,S}$.

2.1 Parameterizations of the turbulent heat and salt transfers

2.1.1 Velocity-independent parameterization

Turbulent heat and salt transfers are set by turbulence in the ocean mixed layer occurring because of the proximity of the moving ocean to the ice interface. The turbulent transfer velocities γ_T and γ_S are therefore expected to depend on the ocean currents in the mixed layer underneath the ice shelf. The simplest approach used to parameterize the transfer velocities attributes constant values to both γ_T and γ_S, hence implicitly assumes a constant mixed layer velocity. It was first used in a three-equation model by Hellmer and Olbers (1989), who set γ_T and γ_S to 10^{-4} ms^{-1} and $5.05 \cdot 10^{-7}$ ms^{-1}. The difference between the values of exchange velocity accounts for the presence of the viscous sublayer at the ice interface, i.e., for the dominance of molecular diffusion over turbulent diffusion in the viscous sublayer, and for the fact that molecular diffusion of heat is more rapid than that of salt. The three-equation model with constant turbulent exchange velocities has been extensively used in the ice shelf-ocean modeling community, notably by Determann and Gerdes (1994), Grosfeld and Gerdes (1997) and more recently by Little et al. (2008), Losch (2008) and Schodlock et al. (2012) .

However, since ocean currents underneath the ice shelf provide the primary source of turbulent kinetic energy for mixing, a more realistic parameterization should allow the exchange velocities to vary quantitatively as a function of the velocity of ocean currents. Jenkins et al. (2010b) analyzed current measurements underneath an ice shelf and demonstrated that the flow velocities in the mixed layer are highly variable in space and time. This implies that the exchange velocities are both site and time dependent. Making reliable model predictions using such parameterization would therefore require spatial and time-specific model tuning against observed melt rates (Jenkins et al., 2010b). Since extensive melt rates measurements are currently not available for most ice shelves, this makes the velocity-independent formulation impractical for numerical predictions.

Moreover, many modeling studies (eg. MacAyeal, 1984b, 1985; Jenkins, 1991; Holland and Feltham, 2006; Holland et al., 2008) suggested that the response of the ice shelf basal melt rate to changes in temperature of the open ocean is above-linear. Holland et al. (2008) explained this response physically by demonstrating that both the temperature difference across the boundary layer and the mixed layer current speed should increase linearly with the ocean thermal forcing. The reasoning behind this statement is that a larger $T_M - T_B$ increases melt rates, thereby enhances the salinity difference between the mixed layer underneath the ice shelf and the far field. The resulting increase in baroclinicity drives in a linear augmentation of mixed layer velocity. The parameterization of the diffusive heat flux Q_M^T presented in the previous section is consistent with a

[4] Ratio of the convective to conductive heat transfer across a boundary: using Nu = 1 amounts to making the the laminar flow assumption. For turbulent flows, the Nusselt number is always greater than one.

linear dependence on $T_M - T_B$ and γ_T. Therefore direct coupling of the exchange velocities and mixed layer currents is necessary for the recovery of an above-linear response of ice shelf ablation rates to changes in ocean temperatures (Holland et al., 2008; Payne et al., 2007), which might have great implications in long-term climate predictions.

2.1.2 Velocity-dependent parameterizations

More recently, other authors such as Jenkins (1991); Holland and Jenkins (1999, 2001); Holland and Feltham (2006); Holland (2008); Holland et al. (2008); Mueller et al. (2012) included an explicit parameterization of the boundary layer in their ice-shelf ocean interactions models that takes into account both the relative importance of the turbulent and molecular diffusion of heat and salt within the boundary layer and the generation of turbulence by ocean currents. Their velocity-dependent closure schemes for turbulent transfers allowed $\gamma_{T,S}$ to be a function of the frictional drag at the ice shelf base through a friction velocity, u_*, related to the velocity of ocean currents in a simple quadratic drag law of the form:

$$u_*{}^2 = C_d U_M^2, \tag{8}$$

with C_d a dimensionless drag coefficient and $U_M = \sqrt{u_M^2 + v_M^2 + w_M^2}$, the magnitude of the mixed layer current velocity.

In terms of the friction velocity, the exchange velocities are expressed as

$$\gamma_T = \Gamma_T u_* \tag{9}$$

and

$$\gamma_S = \Gamma_S u_*, \tag{10}$$

where Γ_T and Γ_S (hereinafter, $\Gamma_{T,S}$) are turbulent transfer coefficients for heat and salt respectively. Formulations for these transfer coefficients were suggested notably by Jenkins (1991) and Holland and Jenkins (1999).

The parameterization of Jenkins (1991) follows that proposed by ? for a hydraulically smooth interface:

$$\Gamma_T = \frac{1}{2.12 \ln(C_d^{1/2}\mathrm{Re}) + 12.5\ \mathrm{Pr}^{2/3} - 9}, \tag{11}$$

$$\Gamma_S = \frac{1}{2.12 \ln(C_d^{1/2}\mathrm{Re}) + 12.5\ \mathrm{Sc}^{2/3} - 9}, \tag{12}$$

where the first and second terms in the denominator of both equations represent the turbulent and molecular diffusive transfers respectively, with Re the Reynolds number and Pr and Sc, the molecular Prandtl and Schmidt numbers. Using the definition of the Reynolds number and equation (8) for the friction velocity, the product $C_d^{1/2}\mathrm{Re}$ can be rewritten as

$$C_d^{1/2} Re = \frac{u_*}{U_M} \frac{U_M D}{\nu} = \frac{u_* D}{\nu}$$

with ν the kinematic viscosity of seawater. Holland and Jenkins (1999) later added an additional level of complexity to this formulation and parameterized the effects of rotation and of melting/refreezing on the stability of the boundary layer. They also assumed a hydraulically smooth ice-ocean interface and followed the

work of McPhee et al. (1987) for the expression of $\Gamma_{T,S}$:

$$\Gamma_{T,S} = \frac{1}{\Gamma_{Turb} + \Gamma_{Mole}^{T,S}} \tag{13}$$

with

$$\Gamma_{Turb} = \frac{1}{k}\ln(\frac{u_* \xi_N \eta_*^2}{f h_\nu}) + \frac{1}{2\xi_N \eta_*} - \frac{1}{k} \tag{14}$$

and

$$\Gamma_{Mole}^{T,S} = 12.5(\mathrm{Pr},\mathrm{Sc})^{2/3} - 6, \tag{15}$$

where k is the Von Karman's constant, f is the Coriolis parameter, ξ_N is a dimensionless stability constant, h_ν is the thickness of the viscous sublayer, estimated as $h_\nu = 5\frac{\nu}{u_*}$. In their formulation of $\gamma_{T,S}$, buoyancy-induced mixing associated with melting/freezing is parameterized through the inclusion of the stability parameter η_* introduced by McPhee (1981):

$$\eta_* = \sqrt{1 + \frac{\xi_N u_*}{f L_o R_c}}, \tag{16}$$

with R_c is the critical flux Richardson number and L_o, the Obukhov length, which is negative for a destabilizing ($\eta_* < 1$) and positive for a stabilizing ($\eta_* > 1$) buoyancy flux. Holland and Jenkins (1999) argued that direct freezing onto the ice shelf base is limited. Therefore they did not consider the effect of destabilizing buoyancy flux on the freezing rate. In the case of a destabilizing buoyancy flux, they thus set $\eta_* = 1$. Other values of parameters and constants used in the formulations of Jenkins (1991) and Holland and Jenkins (1999) are listed in table 1.

One possible caveat of both velocity-dependent parameterizations of Jenkins (1991) and Holland and Jenkins (1999) is the assumption of a hydraulically smooth interface, which is probably correct where the ice shelf base is melting but is likely wrong over regions of refreezing (Holland and Jenkins, 1999). Confidence in this assumption is however helped by the work of McPhee (1992) and McPhee and Morison (1999), who measured turbulent transfers underneath sea ice with a wide variety of roughness characteristics and found that turbulent transfers are seemingly independent of the roughness of the ice-ocean interface. Nonetheless, the roughness characteristics of ice shelf interfaces are yet relatively unknown and there are currently only very few observational evidence supporting the direct applicability of findings from sea ice studies to the ice shelf problem (Jenkins et al., 2010b).

One also notes that using a parameterization of the form (8) for the friction velocity inconveniently includes the unknown dimensionless drag coefficient C_d in the expression of the the turbulent transfer coefficients, such that it is impossible to estimate u_*, C_d and $\Gamma_{T,S}$ independently of one another from equations (8) and (13) alone. However, because seawater has a high Prandtl and very high Schmidt number (i.e., the molecular terms are strongly dominant in the expressions of $\Gamma_{T,S}$), transfer coefficients are only very weakly dependent on the friction velocity. Thus it can be expected that constant values are applicable over a wide range of C_d. Hence in the velocity-dependent formulations of Jenkins (1991) and Holland and Jenkins (1999), the strongest impact of the interfacial roughness is on the transfer of momentum through the boundary layer, not on the transfer of heat nor salt.

Another important limitation of these velocity-dependent parameterizations is that current observations do not provide enough information to allow estimating the unknown drag and turbulent transfer coefficients independently (Jenkins et al., 2010b). One can only place constraints on the product of both coefficients, i.e., on the turbulent exchange velocities $\gamma_{T,S}$. The drag coefficient is the least well constrained of the three

unknowns by observations (Jenkins et al., 2010b). A constant value is usually employed, although roughness characteristics underneath ice shelves are likely to be spatially variable (Nicholls et al., 2006). MacAyeal (1984a,b) first used values suggested by Ramming and Kowalik (1980) for open waters ($C_d = 2.5 \cdot 10^{-3}$) and ice shelf covered waters ($C_d = 5.0 \cdot 10^{-3}$) in a barotropic model of the thermohaline and tidal circulation beneath Ross Ice Shelf, hence attributed the same value of drag coefficient to the seabed and ice shelf base. Following MacAyeal (1984a,b), Jenkins (1991) also employed $C_d = 2.5 \cdot 10^{-3}$ at the ice shelf base in his velocity-dependent parameterization of $\gamma_{S,T}$, which he integrated in a one-dimensional plume model applied to a flow line on Ronne ice shelf. Holland and Jenkins (1999) and Holland and Feltham (2006) later argued that the ice interface should be attributed a smaller drag coefficient than that of seabed to reflect the generally accepted view that ice shelf bases are smoothen by the effects of melting and ice pumping. Hence they adopted a lower value of $1.5 \cdot 10^{-3}$. Holland and Feltham (2006) demonstrated that this drag coefficient is reasonable by fitting their plume model results to observation of basal refreezing. More recently, Jenkins et al. (2010b) tuned the drag coefficient in their model starting from the value originally employed by MacAyeal (1984a,b) and found the best agreement between melt rates simulated using the velocity-dependent parameterization of Jenkins (1991) and two independent series of measurements of ablation rates at the base of Ronne ice shelf for $C_d = 6.2 \cdot 10^{-3}$. They nevertheless made the important point that the drag coefficient is perhaps the most tempting parameter to adjust in models using such a velocity-dependent formulation of the melt rates and that the tuning might actually compensate for other theoretical deficiencies of the model.

Jenkins et al. (2010b) moreover pointed out that the necessity for turbulent transfers parameterizations with the level of complexity of that of Jenkins et al. (2010b) or Holland and Jenkins (1999) cannot be proven from currently available observations. A much simpler formulation which implicitly parameterizes the rate-limiting effect of salt diffusivity on the thermal forcing through an effective friction velocity was notably introduced by McPhee (1992); McPhee and Morison (1999) and presents the advantage of reducing the three-equation formulation to a two-equation formulation. This parameterization showed to produce melt rates agreeing with the three-equation formulation within 10% under typical thermal forcing and ocean currents magnitudes (Holland and Jenkins, 1999) and produced a fit to observed conditions underneath Ronne ice shelf as good as the tuned three-equation model of Jenkins (1991). While there are yet no observational evidence that one formulation is more appropriate than the other, it is nevertheless expected from theory that an explicit salt flux treatment would be applicable to a broader range of ablation rates and ocean conditions. Hence in the following, we favor a full three-equation formulation of melting at the base of ice shelves.

2.2 Topographic and tidal forcing of ice shelf cavity circulation

2.2.1 Rotational and cavity geometry constraints

Many authors investigated the ocean circulation and melt rate distribution underneath ice shelves by modeling ice-ocean interactions in a cavity of idealized morphology typical to the Southern Hemisphere (a north-south oriented ice shelf with base depth decreasing monotonically southward from a vertical ice shelf front a few hundred meters deep to a grounding line 1 or 2 km deep, as sketched in figure 2). A common result of these studies is the set up of a so-called 'ice pump' overturning circulation controlled by buoyancy forcings. In ice cavities, the depression of the freezing point temperature of seawater with pressure at the rule-of-thumb rate of one degree Celsius per kilometer depth induces a temperature gradient between the ocean and ice shelf base that drives a transfer of heat from the ocean to the ice interface. Because the difference between the ocean and local freezing point temperature increases with depth and since typical temperature profiles of the ocean

in front of ice shelves place the warmest waters at the ocean bottom, maximum melt rates are expected at the deepest reaches of the grounding line. There, the (almost) fresh meltwater mixes with the ambient ocean to form a buoyant plume that rises along the ice shelf base, in the direction of the freezing point gradient. When the plume reaches the level at which its temperature corresponds to the local freezing temperature, it becomes supercooled and can form frazil ice. Upon ascent, brine rejection from refreezing increases the density of the cold plume and thereby causes sinking near the ice shelf front. This descending branch warmed by latent heat release closes the overturning circulation underneath the ice shelf and eventually supplies heat for melting at the grounding line.

Two other recurrent results of such idealized modeling studies are maximum melt rates along the south eastern boundary of the cavity, where warm waters first reach the ice shelf base at the grounding line (eg. Determann and Gerdes, 1994; Grosfeld and Gerdes, 1997; Losch, 2008), and the concentration of refreezing at the western boundary, along the path of the rising buoyant plume (eg., Determann and Gerdes, 1994; Grosfeld and Gerdes, 1997; Holland and Feltham, 2006; Holland and Jenkins, 2001; Holland et al., 2008; Losch, 2008). This spatial distribution of phase changes cannot be explained by the 'ice pump' circulation itself (Little et al., 2008), nor the fact that melting and refreezing in more realistic models can actually occur at locations other than the grounding line (Payne et al., 2007; Mueller et al., 2012). Many modeling studies suggested that rotation and cavity geometry are very important controls in that matter (eg., Determann and Gerdes, 1994; Holland and Feltham, 2006; Holland et al., 2008; Payne et al., 2007; Little et al., 2008; Mueller et al., 2012). Theory actually supports this idea, as conditions of weak stratification, steep bedrock topography and sloped ice interface likely enhance the importance of the barotropic mode with respect to the baroclinic modes of cavity circulation. A strong influence of the distribution of background potential vorticity[5] on the horizontal cavity circulation is therefore to be expected in these secluded parts of the ocean.

In particular, Little et al. (2008) investigated interactions between buoyancy forcings and ice shelf cavity geometry through a series of idealized model simulations and extensively discussed the main dynamical constraints on the cavity circulation. They were able to explain the melting/refreezing pattern described above by applying the theory behind the two-layers shallow water model to an idealized cavity geometry. Their model setup is represented in figure 2, which shows a zonally uniform cavity forced with opposing north-south mass fluxes separated by an unforced interior region. In this framework, the two isopycnal layers represent the warm and dense inflowing water at depth and the meltwater plume underneath the ice shelf respectively. Dissipation occurs through bottom, lateral and ice shelf base drag and/or viscosity.

In steady-state, the 2-layers shallow water mass conservation equations are:

$$\nabla \cdot (h_1 \mathbf{u_1}) = -S,$$

$$\nabla \cdot (h_2 \mathbf{u_2}) = S,$$

with $h_1 = z_T(x,y) - \eta(x,y)$ and $h_2 = \eta(x,y) - z_B(x,y)$, the thickness of the top (1) and bottom (2) layers separated by the isopycnal interface $\eta(x,y)$ and S a mass source term representing melting and refreezing. Here, this term is negative for melting and positive for refreezing and the resulting mass loss/gain is of opposite sign in each layer (a positive flux of mass into the upper layer is a negative source of mass from the lower layer). The momentum equation in each layer reads:

$$\mathbf{f} \times \mathbf{u_1} = \frac{1}{\rho_1} \nabla \mathbf{p_1} + \mathbf{F_1},$$

[5] controlled by both rotation and water column thickness

$$\mathbf{f} \times \mathbf{u_2} = \frac{1}{\rho_2} \nabla \mathbf{p_2} + \mathbf{F_2},$$

with p_1 and p_2 the pressure and $\mathbf{F_1}$ and $\mathbf{F_2}$, the dissipation term in the upper and lower layer respectively.

By cross-differentiating the x and $y-$components of the momentum equations and substituting the result in the mass conservation equations, one obtains the shallow water potential vorticity equation for each layer:

$$h_1 \mathbf{u_1} \nabla q_1 = q_1 S - h_1 \mathbf{k} \cdot (\nabla \times \mathbf{F_1}),$$

$$h_2 \mathbf{u_2} \nabla q_2 = -q_2 S - h_2 \mathbf{k} \cdot (\nabla \times \mathbf{F_2}),$$

where $q_1 = \frac{f}{h_1}$ and $q_2 = \frac{f}{h_2}$, the background potential vorticity in each layer.

Important features of the cavity circulation predictable from this conceptual model are:

- When all sources and forcings terms are zero, i.e., the RHS of equation (2.2.1) and (2.2.1) is zero, as in the interior portion of the cavity, the flow in each layer is geostrophic and along contours of potential vorticity, f/h. As Little et al. (2008) pointed out, water column thickness likely dominates over planetary vorticity in setting the overall background potential vorticity gradient underneath ice shelves, because of the relatively limited horizontal extent of cavities and their steep bedrock and ice shelf base topographic features.

- Introducing a mass source ($S \neq 0$, i.e., a source of PV) in the conservation equation initiates a geostrophic flow. If neglecting any other forcing and dissipation, the momentum equation in the first layer becomes

  $$h_1 \mathbf{u_1} \nabla q_1 = q_1 S.$$

  Considering a zonally-uniform ice shelf under which water column dominates over planetary vorticity in setting the overall background potential vorticity gradient, the momentum equation

  $$\frac{1}{h_1}(-uf\frac{\partial h_1}{\partial x}, vh_1\frac{\partial f}{\partial y} - vf\frac{\partial h_1}{\partial y}) = q_1 S,$$

  can be simplified as

  $$v\frac{\partial h}{\partial y} = -S.$$

  This simple relation indicates that melting ($S < 0$) induces a northward flow along the gradient of water column thickness, and a southward flow against the gradient of water column thickness. Underneath an ice shelf with a southward gradient of potential vorticity (water column thickness increasing northward), this sets up a cyclonic circulation in the lower layer around a region of melting, and an anticyclonic circulation around a region of refreezing. The reversal of the sign of the mass source in the upper layer (layer 1) induces opposite circulations there. Closing of the circulation also implies geostrophic zonal jets carrying the water transported by the meridional currents from and to the forced regions (Little et al., 2008). Hence in the case of an ice shelf cavity with water column thickness decreasing southward (as in figure 2, with melting concentrated at the grounding line) one should expect a swift westward current along the grounding line linking the southward flow that brings warm water at depth along the eastern wall and the northward current along the western cavity wall.

- In the unforced interior region, a buoyancy-induced density gradient is set by the opposite regions of melting and refreezing. For cavities with orientation and geometry similar to that shown in figure 2, this gradient between mass sources and sinks must be balanced by a meridional flow (across-background

potential vorticity contours) over the interior part of the cavity. Such ageostrophic transport can however occur only where advection of potential vorticity is dissipated. If neglecting interior viscosity, top and bottom drag as a first order approximation, steady meridional transport will therefore occur at lateral boundaries where there is viscous drag. The Taylor-Proudman theorem predicts that for a poleward water column thickness gradient, eastern-intensification of the meridional return current will occur. On the other hand, if water column thickness decreases poleward, the return current will be along the western boundary. Holland and Feltham (2006) also examined the effects of both Coriolis force and ice shelf basal topography on the concentration of buoyant plumes underneath ice shelves. They showed that when including rotation in an idealized plume model, the buoyant plume becomes rapidly in geostrophic balance and hence flows along contours of water column thickness, such that its upslope propagation and subsequent supercooling are limited. In their model, upslope propagation and refreezing was only possible when including a bathymetric feature running perpendicular to the contours of water column thickness such as a vertical cavity wall that could block geostrophic current and steer the plume flow.

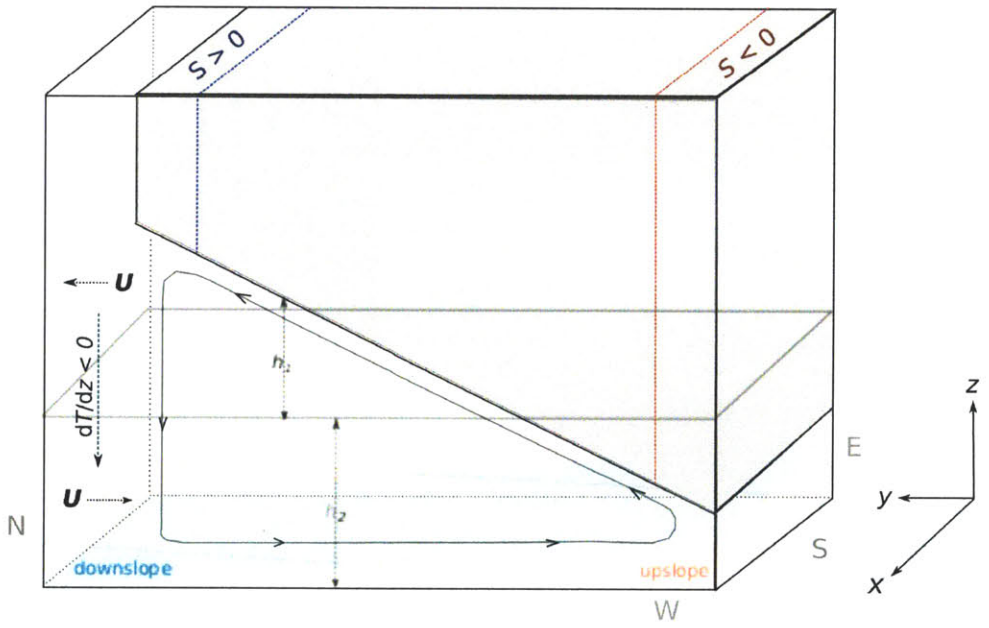

Figure 2: Schematic representation of a typical idealized cavity setup, used for instance by Determann and Gerdes (1994); Grosfeld and Gerdes (1997); Holland and Feltham (2006); Holland and Jenkins (2001); Holland et al. (2008); Holland (2008); Losch (2008). In particular, this setup is used in the 2-layers isopycnic model of Little et al. (2008). In this model, the surface layer has a depth $h_1(y)$ and the bottom layer has a depth of $h_2(y)$.
Adapted from Little et al. (2008).

This idealized 2-layers theory can be extended to a more generic multi (n)-layer model, in which case the shallow water potential vorticity equation in each layer is :

$$h_n \mathbf{u_n} q_n = -q_n(-1)^n S - h_n \mathbf{k} \cdot (\nabla \times \mathbf{F_n}), \tag{17}$$

and the limit of $n \to \infty$ represents a more realistic continuous stratification. To determine the extent to which theoretical findings described above apply in this general case, Little et al. (2008) compared a dynamic-only 2-isopycnic layers model to a more realistic dynamic-thermodynamic 10-isopycnic layers model using a velocity-independent melt rate parameterization. The experiments were performed in an idealized closed ice shelf cavity in which they varied the ice shelf base steepness and used bedrock slopes of different signs (see

figure 2). Comparison of all simulations highlighted important dynamical constraints on the ice shelf basal melt and cavity circulation:

- Locations of melting and refreezing remained unaltered when varying the bedrock topography. Therefore, buoyancy fluxes instead of bathymetry are likely the strongest control of the cavity circulation at depth and on the distribution of phase changes. This suggests that, where contact of warm waters with the ice shelf results in melting, the potential vorticity gradient remains positive as a result of the sink of mass there, regardless of the gradients in bathymetry. The cyclonic circulation set up around regions of basal melt diverts southward flow of warm waters at depth to the east, hence constraining the maximum rates of melting to the south-eastern corner of the cavity. From there, melt rates magnitude decreases westward, as ambient waters mixed with increasing volumes of cold meltwater flow westward in the southern branch of the cyclonic circulation.

- The flow in the mixed layer underneath the ice shelf is primarily driven by the meridional density gradient set up between the regions of melting to the south and refreezing to the north. Hence mixed layer currents are predominantly geostrophic and thus constrained by the distribution of background potential vorticity, which in typical ice shelf environments, is dominated by water column thickness. The gradient of water column thickness in the upper layers is set by the topographic profile of the ice shelf base. In the idealized cavity used by Little et al. (2008) (see figure 2), it is consistent with a western intensification of northward flow against potential vorticity contours. The concentration of refreezing in the northward-flowing meltwater plume along the western boundary is therefore attributed to shelf base topography, while preferential melting along the eastern boundary is due to the buoyancy-forced circulation at depth.

- In all simulations performed, the vertically-integrated volume transport underneath the ice shelf was characterized by an extensive cyclonic gyre. This suggests that the cyclonic flow at depth dominates over the mixed layer (interior) transport in setting the overall circulation, hence that buoyancy fluxes dominate over cavity geometry in determining the sign of the circulation.

- The strength and direction of the overturning circulation is determined by the location and magnitude of buoyancy fluxes. Comparison of experiments using a gently sloping versus a steep ice shelf suggests that the freezing point gradient along the ice shelf base is the dominant constraint on the strength of the overturning circulation. Because the projection of the pressure dependent freezing point gradient along ice interface increases with the horizontal angle of the shelf base, overturning is expected to be stronger under steeper ice shelves. Consequently, melt rates are likely to be stronger along steeper slopes.

This last point in particular was extensively investigated in other modeling studies. Determann and Gerdes (1994) justified theoretically that the slope of the ice shelf base determines the potential for melting/refreezing and hence the mass exchange through the ice-shelf ocean boundary by considering the balance between advection of heat and surface heat flux at the ice-ocean interface. They explained that, the surface freshwater flux being proportional to the velocity and the horizontal temperature gradient at the ice shelf base, fastest melting occurs where velocities are large and where temperature changes rapidly, hence along a steep rather than a gently sloping ice interface (velocities will also be larger where temperature changes rapidly, by thermal wind balance). Holland et al. (2008) later compared simulated melt rates underneath ice shelves of different idealized shapes and found that melting is overall more vigorous for ice shelves with a linear rather than a curved (concave) base depth profile. They explained their result by the fact that the linear profiles used were steeper on average then the curved ones. Walker and Holland (2007) let the shape of the ice interface in their model evolve in time under melting and refreezing and found that melt rates decreased as the shelf base

slope evolved from a near-linear initial profile into a more concave form. Holland et al. (2008) also noted that changing the slope of the seabed does not significantly modify melting conditions and the circulation in the cavity, supporting the suggestion of Little et al. (2008) that buoyancy fluxes dominate over bathymetric constraints in setting the melt rate locations and cavity circulation at depth. These studies therefore all agree on the following two points:

- The strength of the overturning circulation and potential for melting and refreezing are determined by the ice shelf steepness,
- The horizontal circulation is initiated by buoyancy forcings. Its structure is controlled mainly by the location of maximum melt rates and to a lesser extent by the water-depth distribution underneath the ice shelf.

One important aspect of cavity geometry not discussed by Little et al. (2008), whose investigations were restricted to interior cavity dynamics, is the presence of an ice shelf front and its influence on exchanges between the cavity and the open ocean. The ocean-cavity geometry dynamical interactions were investigated notably by Grosfeld and Gerdes (1997), who coupled the three-dimensional model of Determann and Gerdes (1994) to an open ocean model forced by both wind stresses and surface buoyancy fluxes associated with sea ice production. Outside the cavity, they kept the bedrock bathymetry constant such that vertically integrated torque was non-zero only underneath the ice shelf-covered part of the domain. They noticed that when the ocean in front of the ice shelf was covered with ice of thickness equal to the ice shelf front depth, the vertically-integrated flow underneath the ice shelf could extend outside the cavity because of the combined effects of inertia and friction, thereby allowing exchanges between the cavity an open ocean. However in the case of an open ocean in front of the ice shelf, the abrupt water column thickness change at the ice shelf front and associated potential vorticity jump caused the western-intensified boundary current to immediately turn eastward when reaching the shelf edge, thereby restricting the extend of the the cavity circulation and inhibiting barotropic communications between the cavity and open ocean. This in turn constricted the descending branch of the overturning circulation associated with refreezing within the plume to the interior side of the ice shelf front. Deep mixing associated with brine rejection by sea ice production in front of the ice edge also coincided with the descending branch of the overturning circulation and further isolated the cavity circulation. Grosfeld and Gerdes (1997) therefore concluded that the potential vorticity barrier induced by the presence of the ice shelf front limits the sensitivity of the cavity dynamics to external forcings and open ocean hydrography. They also noticed that this secluding effect was enhanced in the presence of a bathymetric sill oriented parallel to the shelf edge, which is a common feature of ice shelf cavities. On the other hand, they found that barotropic exchanges across the ice edge and ventilation of the cavity were possible if the bedrock bathymetry was such that contours of potential vorticity crossed the ice shelf front. Underneath ice shelves, this only happens when the meridional walls are sloping towards the interior of the cavity, or where deep troughs in the continental shelf cross the ice shelf edge.

Grosfeld and Gerdes (1997) (and Determann et al., unpublished) extended their modeling effort to a realistic Filchner-Ronne Ice Shelf cavity setup and found most dynamical constrains on the cavity circulation described above in overall agreement with their results. Weak stratification in the Weddell Sea indeed constrained the cavity flow in their simulations to conserve potential vorticity and caused the distribution of melting and refreezing to be controlled by the dominant horizontal barotropic circulation. Schodlock et al. (2012) recently modeled the circulation underneath the Pine Island Ice Shelf using two different sea floor bathymetry data sets from BEDMAP and from the NASA IceBridge program. The large differences between the two simulated melt rate patterns and the 25% higher mean melt rate obtained using the IceBridge data, which reveal a

trough enabling warm open ocean (CDW) waters to reach the grounding line, supports a strong topographical constraint on the cavity dynamics. Grosfeld and Gerdes (1997) moreover pointed out that in the absence of bathymetric features enabling cross-ice edge barotropic transport, exchanges between the cavity and the open ocean are restricted to short timescale fluctuations of the ocean circulation, such as tides. However, the short periods and magnitudes of tidal current fluctuations restricts tidal transport across the ice shelf edge to short distances. Some processes must therefore enable the oscillating flow to interact with the time-independent barotropic or thermohaline circulations in order for cavity dynamic to be affected by tides on wider scales.

2.2.2 Tidal forcing on the cavity

Many studies suggest that tidal forcing can be an important if not dominant control on the intensity and location of thermodynamic processes even under remote parts of ice shelf cavities. MacAyeal (1984a; 1984b; 1984c) first hypothesized that, because ice shelf cover prevents air-sea contact, fluctuations such as tidal currents should be the principal source of small-scale turbulence and turbulent kinetic energy in the ice shelf-covered ocean. MacAyeal studied in detail the case of Ross Ice Shelf, under which tides are the strongest form of ocean motion. He found that tidal currents are largest in parts of the cavity where the water column is shallow, which often coincide with the location of the grounding line. In these regions, tidal currents can contribute significantly to mixing. He suggested that destruction of stratification by tidal mixing accelerates the melt rates, either by bringing the deepest and warmest cavity waters in contact with the ice or by eroding the cold and fresh film that insulates the ice shelf base once melting is set up. Jenkins et al. (2010b) more recently suggested that inclusion of tidal forcing in ice shelf cavity models generate a large time variability in melt rates. Makinson et al. (2012) analyzed three-dimensional ice shelf motion fields from nine GPS deployed on this ice shelf and showed that over 96% of its horizontal displacement variance occurs at the diurnal and semi-diurnal frequencies, suggesting tides as the main drivers the ice shelf motion. Recently, Makinson et al. (2011) forced an isopycnic cavity model of the Filchner-Ronne Ice Shelf with realistic tides by prescribing sea surface elevation predictions from the Circum-Antarctic Tidal Simulation (CATS02.01) model. Inclusion of tides in their model increased the kinetic energy production underneath the ice shelf by three to four orders of magnitude. The largest production reached 1 Wm^{-2} and induced full water column mixing at the ice shelf front, enabling for the first time the reproduction of the intense melt rates observed there. The cavity-averaged increase in melt rate resulting from the inclusion of tides in this model was about two folds, with local increases in refreezing and melting of six-fold and three-fold respectively. The time-independent cavity circulation was intensified and most importantly, fluxes across the ice shelf edge doubled in his model, thereby suggesting that tides can promote exchanges between the open ocean and ice shelf cavities. In the following paragraphs different processes by which tidal fluctuations can interact with the steady barotropic and thermohaline cavity circulation to induce such important modulations of the cavity dynamic are discussed. Brief theoretical descriptions of each phenomena are given and important results of studies in which they were investigated are mentioned.

Tidal rectification

Tidal rectification is the process by which periodic flow generates time-independent currents in the presence of spatial gradients in friction. The process is predictable from the simple one layer shallow water, f-plane model when forced with only periodic barotropic currents (no wind stress) and in which dissipation through bottom and/or ice shelf base drag is allowed. Here it is described in the context of an idealized meridionally-sloping ice shelf in a domain with no along-water depth (zonal) variations (as in figure 2). The effects of flexure

and motion of the ice shelf on tidal propagation are ignored[6] and the following assumptions are made:

1. The tidal flow is linear.

2. Sea-level variations are much less than the total water column thickness, i.e., $\eta << h$. This approximation is generally valid underneath ice shelves as the free surface elevation tidal signal is typically of about 1 m (Padman et al., 2002) and the typical water column thickness in the cavity varies between 100 m and 1 to 2 km.

3. The contribution of the time-variability of sea surface elevation to the total depth-integrated transport is negligible. From the continuity equation

$$\frac{\partial \eta}{\partial t} + \frac{u(\eta + h)}{x} = 0$$

this assumption implies

$$\frac{\eta}{h} << \frac{U}{\omega L},$$

where U and L are horizontal and tidal velocity scales for the cavity. Hence, the ratio $\frac{\eta}{h}$ is much less than the ratio of tidal excursion[7] to the length scale of depth variation. Assuming for instance an across-h tidal current of 0.1 ms^{-1} underneath an ice shelf 100 km in extent where variations in bathymetry scale between 10 and 50 kilometers, the ratio $\frac{U}{\omega L}$ is of about 0.1 to 0.45 for semi-diurnal tides and twice as big for diurnal tides, hence most likely two orders of magnitude higher than the ratio of $\frac{\eta}{h}$.

4. Frictional stresses at the bottom and along the shelf base can be represented by a linear drag law of the form $\frac{r}{h}\mathbf{u}$, with r the friction parameter and $\frac{r}{h}$, the inverse friction time scale. Here, we assume r is constant everywhere, i.e., spatial gradients in friction are induced by the gradients in water column thickness, not by spatial changes in roughness characteristics of the ice shelf base or ocean bottom[8].

Within these assumptions, the shallow water system is described by the following x and y momentum and mass conservation equation:

$$\frac{\partial u}{\partial t} + u\frac{\partial u}{\partial x} - fv = -g\frac{\partial \eta}{\partial x} - \frac{ru}{h(x)} \tag{18}$$

$$\frac{\partial v}{\partial t} + u\frac{\partial v}{\partial x} + fu = -\frac{rv}{h(x)} \tag{19}$$

$$\frac{\partial (uh)}{\partial x} = 0 \tag{20}$$

with η the free surface elevation, h, the undisturbed water column thickness, which varies only in the x-direction and f the Coriolis parameter. The current velocity $\mathbf{u}$ can be partitioned as

$$\mathbf{u} = \bar{\mathbf{u}}(\mathrm{x}) + \hat{\mathbf{u}}(\mathrm{x}, \mathrm{t})$$

[6]These effects are likely negligible at the center of the cavity but might have significant impacts within several kilometers of coasts (MacAyeal, 1984a)

[7]the range of horizontal tidal movement of individual water columns

[8]Tidal rectification would also arise if water column thickness was constant everywhere but shelf base and/or seabed roughness characteristics varied in space.

with $\bar{\mathbf{u}}$ the non-tidal, time-independent flow (which varies only in the x direction) defined as

$$\bar{\mathbf{u}} = \frac{1}{T}\int_0^\infty \mathbf{u}\, dt$$

and $\hat{\mathbf{u}}(x,t)$ a tidal perturbation flow such that

$$\frac{1}{T}\int_0^\infty \hat{\mathbf{u}}\, dt = 0$$

where T is the tidal period. The partitioning divide the system of equations into two systems for the tidal and time-averaged flows.

The mass conservation and y-momentum equations for the tidal flow are

$$\frac{\partial \hat{v}}{\partial t} + f\hat{u} = \frac{r}{h}\hat{v} \tag{21}$$

$$\frac{\partial(\hat{u}h)}{\partial x} = 0 \tag{22}$$

where the assumption of a linear tidal flow has been used. The conservation equation implies that the transport can only vary in time, not in x. Assuming a time-periodic solution for the transport, the solution for the cross-h flow reads

$$\hat{u} = \frac{a}{h}\cos\omega t$$

with a, an arbitrary constant in both time and x. Similarly, one can assume a solution of the form

$$\hat{v} = b\cos\omega t + c\sin\omega t,$$

for the along-h flow. b and c are constant that are solved for by inserting the solutions for both components of the tidal flow in the y-momentum equation. Doing so, one obtains for $\hat{v}$

$$\hat{v} = -\frac{fa}{\omega h(1+\frac{r^2}{\omega^2 h^2})}[\frac{r}{\omega h}\cos\omega t + \sin\omega t].$$

This solution indicates that in the absence of drag, i.e., when the first term in square brackets is zero, $\hat{v}$ is perfectly out of phase with $\hat{u}$ and hence $\overline{\hat{v}\hat{u}} = 0$. In the presence of drag, the non-linear term $\overline{\hat{v}\hat{u}} \neq 0$ and there is a cross-h variation in tidal velocity that induces a non-zero time-averaged momentum flux. The resulting tidally-rectified flow $\bar{v}$ can be inferred from the time-averaged conservation and y-momentum equations:

$$\overline{\hat{u}\frac{\partial \hat{v}}{\partial x}} + f\bar{u} = -\frac{r}{h}\bar{v}$$

$$\frac{\partial(\bar{u}h)}{\partial x} = 0$$

Considering that the time-independent transport must be finite, hence go to zero at the coast ($x = 0$) and as $x \to \infty$, and that $h \neq 0$ constrains the time-independent cross-h transport $\bar{u}$ to be zero everywhere. From the solution for $(\hat{u}, \hat{v})$, one then obtains

$$\bar{v} = -\frac{a^2 f}{\omega^2 h^3}\frac{\partial h}{\partial x}\frac{1}{(1+\frac{r^2}{\omega^2 h^2})^2}. \tag{23}$$

Equation (23) highlights important characteristics of the tidally-rectified flow, $\bar{v}$:

- Tidally-rectified currents are strong where tidal currents are fast.
- Tidally-rectified currents are parallel to depth contours. Where isobaths are blocked by the ice shelf base or the cavity wall, the flow is forced to converge into an intensified boundary layer flow.
- Since $\bar{v} \propto \frac{\partial h}{\partial x}$, the time-independent flow is faster along steep slopes. Strong tidal rectification is also expected at jumps in water column thickness, for instance, at the ice shelf edge.
- Since $\bar{v} \propto \frac{1}{h^3}$, tidally-rectified currents are stronger in shallow waters.
- As $\bar{v} \propto -f\frac{\partial h}{\partial x}$, the flow is in the direction of Kelvin wave propagation. That is, the along-h flow has shallow water column thicknesses to the right in the Northern Hemisphere and to the left in the Southern hemisphere. Currents will therefore be anticyclonic about shallow h, as over sills, and cyclonic about depressions of the seabed.

The generation of residual time independent currents by tidal fluctuations under an ice shelf cavity was investigated in details by MacAyeal (1984c) in the realistic context of Ross Ice Shelf. The author gave a more general description of tidal rectification including advection terms, a quadratic parameterization of bottom drag and viscous dissipation, as done in many ice shelf cavity numerical models. The governing equations in this case are

$$\frac{\partial \mathbf{u}}{\partial t} = -\mathbf{u}\cdot\nabla\mathbf{u} - g\nabla\eta - \mathbf{f}\times\mathbf{u} + \frac{\tau}{h}, \tag{24}$$

$$\frac{\partial \eta}{\partial t} = -\nabla\cdot(h\mathbf{u}), \tag{25}$$

with $\tau = -C_d|\mathbf{u}|\mathbf{u} + h\nu\nabla^2\mathbf{u}$ the frictional dissipation term. Partitioning of this system into a time-independent and periodic tidal free surface elevation and current component leads to the following systems of equations for the mean flow:

$$g\nabla\bar{\eta} + \mathbf{f}\times\bar{\mathbf{u}} = -\overline{\hat{\mathbf{u}}\cdot\nabla\hat{\mathbf{u}}} - \bar{\mathbf{u}}\cdot\nabla\bar{\mathbf{u}} - \frac{\overline{\tau}}{h}, \tag{26}$$

$$\nabla\cdot(\overline{h\mathbf{u}}) = -\nabla\cdot\overline{\hat{\eta}\hat{\mathbf{u}}}. \tag{27}$$

As in the very simplified case described previously, net time-averaged tidal momentum ($\overline{\hat{\mathbf{u}}\cdot\nabla\hat{\mathbf{u}}}$) and mass ($\nabla\cdot\overline{\hat{\eta}\hat{\mathbf{u}}}$) fluxes remain in the presence of frictional dissipation. These fluxes force the time-independent circulation.

Both the models described above are barotropic models, and yet one can question the relevance of barotropic theory in the more general case of a stratified fluid. Brink (2011) recently investigated the phenomenon of tidal rectification in a stratified ocean using the Regional Oceanic Modeling System (ROMS) primitive equations numerical model in a coastal ocean break setup. The most striking difference between his results in a stratified versus a barotropic ocean is the intensification of rectified mean momentum at the seabed, which leads to 'trapping" of strong currents near the bottom boundary layer and to a strong decrease of the time-mean flow towards the surface. Except in the bottom boundary layer, the time mean flow in his stratified model is still generally along-isobaths. In upper layers, the mean flow appears fairly barotropic. Moreover, the general parameter dependence is similar in the barotropic and baroclinic cases. In a weakly stratified environment, such as a typical ice shelf cavity, one can therefore expect tidally-rectified currents to be in overall agreement with barotropic theory.

In the numerical simulations of Ross Ice Shelf of MacAyeal (1984c), a scan for areas over which both the gradients in water column thickness and tidal currents were strong showed the locations of significant tidal rectification, in agreement with theory. These areas were concentrated along the ice shelf front and in the

vicinity of a sill. MacAyeal (1984c) obtained time-independent barotropic circulations around these regions on the order of 0.015 m/s and 0.005 m/s respectively, that is at least 5% as strong as the local tidal currents. He moreover pointed our that even weak tidally-rectified currents can be efficient at promoting heat exchanges between the open ocean and the cavity interior and accelerating melt rates if collocated with critical areas such as locations of inflow of shelf waters. In the simulations of MacAyeal (1984a), the strongest tidally-rectified flows occurred along the ice shelf front and increased heat exchanges with the open ocean such that to accelerate basal melting by 0.5 m/yr over about 10% of the ice shelf area, that is, to produce melt rates O(10) times higher than the ice shelf average. Recently, Mueller et al. (2012) reported that tidally-rectified flows underneath Antarctic ice shelves can reach up to 10% of the magnitude of the local tidal currents. In their simulations of the circulation underneath Larsen C Ice Shelf, they obtained the largest melt rates over the regions of strongest tidally-induced time-average barotropic currents, which occurred over shallow areas with large spatial gradients in water column thickness. Comparison of a simulation forced only by thermodynamic processes and others also forced with realistic tidal currents showed that the maximum time-averaged flows in the unforced case were only 1/5 as strong as in the tidally-forced cases.

Tidal fronts and mixing

Typical profiles of ocean density in ice shelf cavities show a stably stratified environment, as cold waters mixed with fresh meltwater form the surface layers and warm but salty waters, the deep ocean layers (Jacobs and Hellmer, 1996). However, as mentioned by Holland (2008) and Jenkins et al. (2010b), indications of well-mixed layers are common in sub-ice shelf mooring measurements. Destruction of the stratification in the cavity can occur only where the rate of production of turbulent mechanical energy is important enough to overcome the stratifying buoyancy flux due to melting. Such turbulence can be generated at the seabed and ice shelf base by the proximity of tidal currents or in the wake of buoyant plumes. In the first case, the resulting hydrographic transition between stratified and well mixed areas is referred to as a tidal front. In theory, the position of a tidal front underneath an ice shelf cavity dominated by tidal dynamics can be predicted by equating the rate of energy dissipation by tidal currents and the rate of decrease of gravitational potential energy by stratifying buoyancy fluxes. As shown in figure 3, this position should be the meeting point of the bottom boundary layer and of the surface mixed layer underneath the shelf base.

In a barotropic model, the rate at which energy is transferred from the large-scale tidal flow to small-scale turbulence by frictional processes at both the seabed and the ice shelf base can be parameterized using a quadratic law of the form

$$\tau = C_d|\hat{\mathbf{U}}| \cdot \hat{\mathbf{U}}$$

with $\hat{\mathbf{U}}$, the depth-averaged tidal flow and C_d the sum of the prescribed bedrock and shelf base drag coefficients. In reality, only a small fraction of this energy transfer actually contributes to increasing the gravitational potential energy of the water column through mixing. The effective turbulent power is estimated as

$$P_T = \alpha\bar{\rho}C_d|\hat{\mathbf{U}}|\hat{\mathbf{U}} \cdot \hat{\mathbf{U}} \tag{28}$$

where $\bar{\rho}$ is the ocean density (uniform in a barotropic model) and α is a dimensionless efficiency coefficient between zero and one (MacAyeal, 1984a). Assuming meltwater has zero salinity, which as mentioned the 3-equations model description above, is a reasonable approximation, and density is a linear function of salinity only, the power required to maintain a well-mixed water column of depth h subjected to a meltwater flux is given by

$$P_B = \frac{1}{2}m\bar{\rho}\beta Sgh \tag{29}$$

where β is the haline contraction coefficient of seawater, S the ocean salinity, m the melt rate, h the water column thickness and S, g the acceleration due to gravity. Equating equations (28) and (29) provides an estimate of the maximum melt rate m_{max} for which well-mixed conditions and the maintenance of a stable ice front are possible:

$$m_{max} = \frac{2\alpha C_d |\hat{\mathbf{U}}| \hat{\mathbf{U}} \cdot \hat{\mathbf{U}}}{\beta S g h} \tag{30}$$

From this expression of the critical melt rate, theoretical predictions can be made about the sensitivity of the tidal front position to the cavity geometry and forcings:

- As the maximum melt rate allowing de-stratification is inversely proportional to the water column thickness h, well mixed conditions are more likely in parts of cavities where the water column is very thin. For ice shelves of typical morphology, that is, with water column thicknesses decreasing inwards, well-mixed conditions are therefore to be expected near the grounding line. Additionally, tidal mixing should become more vigorous towards the grounding line as tidal velocities generally increase in shallow areas of the cavity. The combination of strong tidal currents and low power required to maintain shallow waters de-stratified makes the tidal front position very sensitive the water column thickness and ice shelf draft gradient.

- As m_{max} is proportional to $|\hat{\mathbf{U}}|\hat{\mathbf{U}} \cdot \hat{\mathbf{U}}$, the well mixed areas underneath the ice shelf should be larger for stronger tidal currents. However, increasing tidal currents will also accelerate the melt rates and hence the stratifying buoyancy fluxes. As the melt rate varies linearly with $|\hat{\mathbf{U}}|$ (or U_M) in the melt rate parameterizations of Jenkins (1991) and Holland and Jenkins (1999) and the critical melt rate varies like $\hat{U}^3$, the increase in m_{max} should dominate over the acceleration in melting.

- Melting underneath the ice shelf should increase linearly with ocean temperature and salinity, because of the depression of the pressure freezing point (or T_B) with salinity, but more more slowly with salinity than with temperature. Larger ocean temperatures and salinity are therefore expected to limit the extent of well mixed regions underneath the ice shelf by reducing the water column thickness that can be mixed by the action of tidal currents.

- The critical melt rate should increase linearly with the drag coefficient C_d at the ice shelf base and/or sea bottom. According to the velocity-dependent melt rate parameterizations of Jenkins (1991) and Holland and Jenkins (1999), the melt rate also increases with the drag coefficient, but in a sub-linear manner. Hence increasing C_d should result in a net spread of well mixed conditions in the cavity.

- As the critical melt rate is linearly proportional to the efficiency coefficient, the extent of well mixed conditions should increase with α. This dependence was recognized by Holland (2008) as a major flaw of this simple model, since the value of α is in practice very poorly constrained. He reported the use of coefficients varying between 0.5% and 1.5% in different models of tidal fronts.

MacAyeal (1984a) used the definition of the critical melt rate above to estimate the position of tidal fronts underneath Ross Ice Shelf. He calculated m_{max} from the water column thickness and spatial distribution of ocean properties predicted by a barotropic cavity model forced with tidal surface elevation signals and compared the critical melt rate to the simulated melt rates, reaching at most 0.05 to 0.5 m/yr. His estimates of the extent of well mixed conditions underneath Ross Ice Shelf exceeded 100 km. MacAyeal (1984a) therefore suggested that stirring of the water column by tidal currents might by an efficient mechanism by which warm deep water are brought into contact with the ice shelf base and an important trigger of the thermohaline cavity circulation. Holland (2008) later investigated the impact of tidal front formation on the circulation

and melt rates underneath ice shelves using a 1-dimensional model and a highly idealized cavity geometry represented in figure 3. The only forcings considered in this modeling exercise was the generation of turbulence by a spatially uniform and steady flow at the mean tidal speed and buoyancy fluxes from velocity-dependent melting at the ice shelf base. Tidal front formation was assumed a priori, starting from the grounding line and the outward-most tidal front position was calculated by comparing the actual melt rates and the critical melt rates given by equation (30) and by converting the critical water column thickness h into horizontal length using the prescribed water column thickness gradient. Using hydrographic conditions and a water column thickness gradient representative of the conditions beneath the eastern portion of Ross Ice Shelf, he obtained comparatively larger melt rates and hence predicted well mixed areas one order of magnitude less extensive than that simulated by MacAyeal (1984a). Sensitivity experiments in which he varied the tidal currents, ocean forcing, drag coefficient and ice shelf base depth gradient were in good agreement with the predictions from theory listed above. However, for most realistic scenarios of forcing and cavity geometry, he found that tidally mixed areas near grounding lines remained small, unless refreezing conditions coincided with both very small water column thickness gradients and vigorous tidal currents. Furthermore, his model indicated that over well-mixed portions of the cavity, the melt rate actually decreased towards the grounding line. He therefore concluded that melting must be mostly controlled by entrainment of heat into upper layers, for instance, by the upwelling meltwater plume, rather than by tidal mixing. He also pointed out that tidal mixing should actually insulates grounding lines from warm water offshore, in the sense that melting underneath stratified parts of the ice shelf tend to vary over-linearly with the increase in far field ocean temperature (Holland et al., 2008), but over well mixed regions, it varies linearly with ocean temperature. His findings are therefore directly opposite to that of MacAyeal (1984a). Furthermore, Holland (2008) hypothesized that the contribution from tidal turbulence must be especially negligible compared to turbulence induced by buoyant plume flows in promoting basal melting beneath ice warm shelves, which are forced with large basal temperature gradients and relatively weak tidal currents.

Topographic vorticity waves

Another mechanism by which the effect of tidal currents can be amplified underneath ice shelves is the generation of topographic Rossby waves. Such perturbations arise from forced across-isobath (or across-water column thickness) displacement of the water column and therefore can be expected at sharp jumps in water column thickness, such as the ice shelf front, and along prominent sills. When forcing a cross-water column thickness flow, conservation of potential energy induces a wave that propagates in the along-isobath (along-water column thickness) direction with shallow depth to the left, in the southern hemisphere. In the case of a topographic barrier, i.e., along the ice shelf front, the minimum forcing period that can support these waves is given by

$$\frac{1}{\omega} \geq f \frac{h_2/h_1 - 1}{h_2/h_1 + 1}, \tag{31}$$

where h_1 and h_2 are the water column thicknesses on the interior and exterior side of the ice edge respectively (MacAyeal, 1984a). In polar latitudes, this means that only diurnal tides are expected to excite topographic Rossby waves. MacAyeal (1984a) modeling study of Ross Ice Shelf indicated that the production by tides of strong periodic barotropic currents with large horizontal shear could effectively stir the water column over some parts of the Ross Ice Shelf cavity.

In a stratified ocean, barotropic tides can also generate periodic baroclinic flows by interaction with steep topographic features. Underneath ice shelf, the the generation of strong baroclinic tides is likely to promote mixing and melting, thereby enhancing the effect of tides on the cavity dynamics (Mueller et al., 2012).

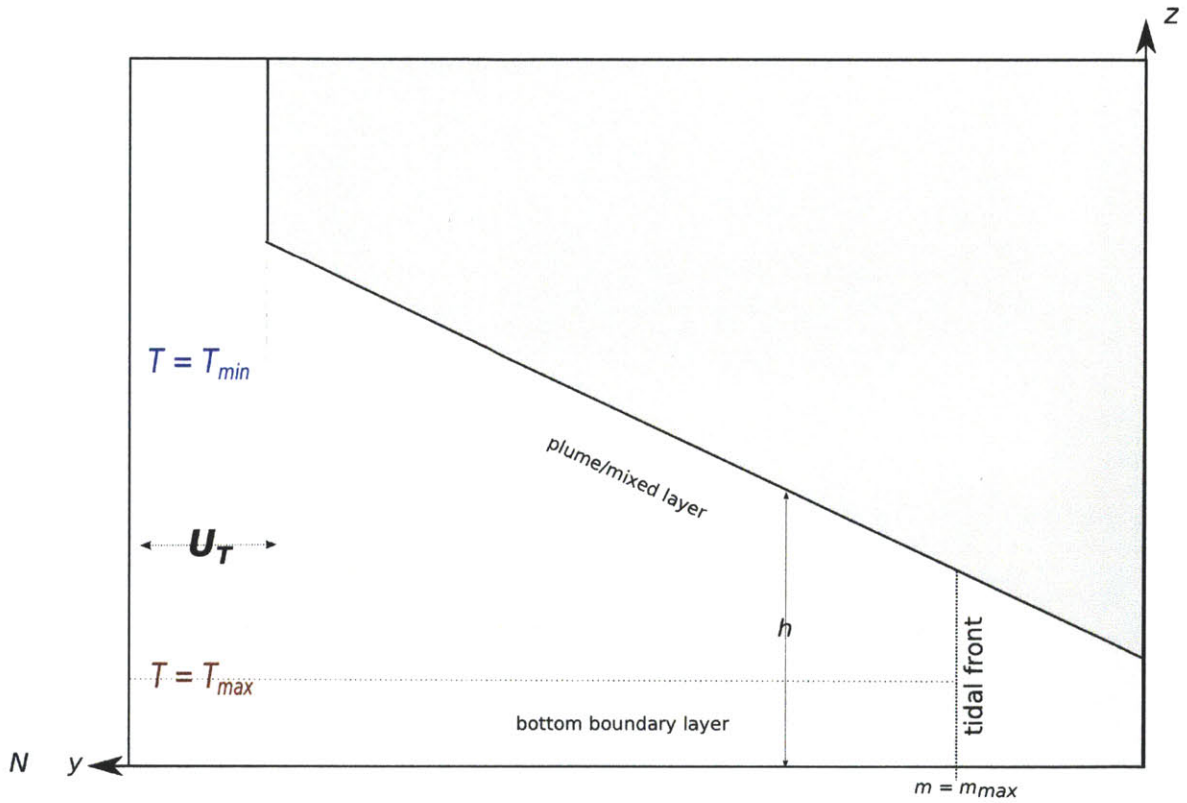

Figure 3: Schematic representation of tidal front formation in a meridionally-oriented ice shelf cavity which has a stably stratified interior and potential temperature increasing with depth. The tide front location coincides with the point at which the mixed layer, or plume, underneath the ice shelf meets the layer at depth that is well mixed by bottom frictional effects. At this point, the melt rate underneath the ice shelf is equal to the maximum melt rate m_{max} for which tidally-induced turbulence keeps the water column of depth $h(y)$ well mixed (equation 30).
Adapted from Holland (2008).

Parameter	Symbol	Value
Ice shelf		
thickness	h_I	
surface temperature	T_s	$-20.0°$C
bulk salinity	S_I	0 psu
ice density	ρ_I	917 kg m^{-3}
heat capacity	c_{p_I}	2000J kg^{-1} K^{-1}
molecular thermal conductivity	κ_I^T	$1.54 \cdot 10^{-6}$m^{2}s^{-1}
Surface temperature	T_S	$-20°C$
Ice-ocean boundary layer		
thickness	D	
temperature	T_B	
salinity	S_B	
pressure	p_B	
Ocean mixed layer		
thickness	Δz	20 m
temperature	T_M	
salinity	S_M	
water density	ρ_M	
specific heat capacity	c_{p_M}	3998J kg^{-1} K^{-1}
Latent heat of fusion	L_f	334000J kg^{-1}
Latent heat flux	Q^T_{latent}	
Brine flux	Q^S_{brine}	
Diffuisve heat flux through the BL	Q^T_M	
Diffusive salt flux through the BL	Q^S_M	
Diffusive heat flux through the ice shelf	Q^T_I	
Diffusive salt flux through the ice shelf	Q^S_I	0
Melt/refreezing rate	m	
Transfer velocities parameterizations		
Turbulent transfer velocity for heat	γ_T	
Turbulent transfer velocity for salt	γ_S	
stability parameter	η_*	1.0
Von Karman's constant	κ	0.4
stability constant	ξ_N	0.052
kinematic viscosity of sea water	ν	$1.95 \cdot 10^{-6}$ m^{2}s^{-1}
Coriolis parameter	f	
Prandlt number	Pr	13.8
Schmidt number	Sc	2432
Model parameters		
Advection scheme		3^{rd} order direct space-time
Vertical advection and diffusion		Implicit for T and S
Equation of state		Jackett and McDougall (1995)
Vertical viscosity		10^{-3}m^{2}s^{-1}
Laplacian viscosity		0.2
Bi-harmonic viscosity		0.02
Vertical diffusion		$5 \cdot 10^{-5}$m^{2}s^{-1}
Horizontal diffusion		10 m^{2}s^{-1}
Quadratic bottom drag		$2.5 \cdot 10^{-3}$
Quadratic shelf base drag	C_d	$1.5 \cdot 10^{-3}$ (default)
Minimum partial cell factor		0.1 (1/8°), 0.3 (1/32°)
Reference ocean density,	ρ_{ref}	1000 kg m^{-3}

Table 1: 3-equation model parameters and constants

3 The model and experimental setup

3.1 The MITgcm and ice shelf cavity model

We use the MIT general circulation model (MITgcm) of Marshall et al. (1997). The current implementation of this finite-volume grid-point algorithm solves the Boussinesq hydrostatic form of the Navier-Stokes equations for an incompressible fluid on an Arakawa C-grid. MITgcm is coupled to the ice-shelf cavity model of Losch (2008). The original version of this model uses the exact same three-equation formulation of the thermodynamic processes at the ice interface as Hellmer and Olbers (1989). The current modified version includes the velocity-dependence of the heat and salt turbulent transfer velocities as formulated by Holland and Jenkins (1999). There are only two differences between the present parameterization and to the full formulation recommended by Holland and Jenkins (1999):

- In the current model, the effects of buoyancy fluxes on the stability of the boundary layer are neglected. Hence, the second term on the RHS of equation (16) for the stability parameter η_* is assumed small and η_* is set to 1. Holland and Jenkins (1999) found that this approximation modified the melt rates by less than 10% under conditions of moderate friction velocities and thermal driving.

- The heat flux through the ice shelf, Q_I^T is parameterized by neglecting advection, i.e., by considering only vertical diffusion of heat through the ice. In this case the gradient in ice temperature at the base of the shelf is linear and can be estimated as

$$\left.\frac{\partial T_I}{\partial z}\right|_B = \frac{T_S - T_B}{h_I},$$

  with T_S the (constant) surface temperature of the ice shelf and h_I, the local thickness of the ice shelf. The full expression for the heat flux trough the ice is therefore

$$Q_I^T = -\rho_I c_{pI} \kappa_I^T \frac{T_S - T_B}{h_I},$$

  with ρ_I the density of freshwater ice and κ_I^T, the molecular thermal conductivity. This approximation is widely used in sea-ice modeling and usually preferred in velocity-dependent ice shelf models. However, (Holland and Jenkins, 1999) pointed out that highly non-linear temperature profiles were actually observed for thick ice shelves, and so the linear approximation should not be as good for ice shelf modeling that it is in sea ice models. They compared melt/freezing rates obtained using this linear approximation and a more complex formulation that accounts for the effects of a constant vertical advection of heat through the ice. Under freezing conditions the two formulations produced the same results. Under melting conditions, i.e., when the mixed layer is at or above the freezing temperature, the inclusion of constant vertical advection reduced the melt rates by about 10%.

As in the model of Holland and Jenkins (1999), it is assumed that all phase changes occur at the ice-ocean boundary. The formation of sea ice in front of the ice shelf is not simulated. The formation of frazil ice through supercooling in the water column is not parametrized either. Although this process is thought to be the dominant mechanism of ice shelf basal growth and to account for 10 times more ice formation than direct refreezing (Holland and Feltham, 2006), neglecting it in the present model configuration is not expected to affect the cavity dynamics greatly. Frazil ice formation actually accelerates the plume slightly by increasing

its buoyancy when it becomes supercooled. However, as will be discussed in section 4, regions over which the plume refreezes underneath our 'warm' idealized and realistic PIIS ice shelves are very limited.

The main particularity of the cavity model of Losch (2008) is the use of geopotential height coordinates (the so called 'z-coordinates'), together with a partial cells method (Adcroft et al., 1997) to represent the seabed and the ice shelf base topography. While isopynic coordinates are a natural choice for density-driven flows and hence are extensively used in ice shelf cavity models, this z-coordinate model presents the advantage of being easily implemented within global circulation ocean models that are formulated in height coordinates. Also, it does not necessitate including a non-isopycnic layer to admit ice-ocean interface buoyancy forcing (Losch, 2008) or making adjustments to the cavity geometry to avoid numerically induced errors at sharp topographic features, unlike σ-coordinates models.

On the other hand, an important trade-off in the choice of z-coordinates is the loss of resolution of the ice shelf base topography. While σ-coordinates conveniently turn the ice shelf base and bedrock into coordinate surfaces, z-coordinates intersect the ice and seabed interfaces. The resulting 'jumps' between vertical levels induce noise in the model solution in different ways.

Part of the noise is associated with density differences between cells that intersect the ice shelf base and hence are affected by melting/refreezing and their unaffected neighbors (see Losch (2008) for a more detailed explanation). The induced density gradients generate geostrophic currents along the ice shelf base and the resulting singularities in ocean velocities can induce noise in the overturning thermohaline circulation. This effect is more important for large vertical cell thickness and is therefore reduced when using a partial cell treatment and high vertical resolution.

Grid-scale waves are another common source of noise in z-coordinates models. These occur because the necessary averaging of the Coriolis term on C-grids induces incorrect group velocities for some short waves that can feed short-scale perturbations when energy is generated at the grid-scale, for instance near topography. The net result is persistent noise. A more extensive description of sources of noise in solutions of the z-coordinates ice cavity model is made by Losch (2008).

z-coordinates models are also known to have difficulty representing the flow of positively or negatively buoyant plumes along slopes when topographic features are not sufficiently resolved (Losch, 2008) and necessitate intermediate to high horizontal and vertical resolutions to produce results similar to that of isopycnic models. In particular, Losch (2008) demonstrated that the melt rates underneath the ice shelf depend strongly on the vertical resolution of its z-coordinates model and found that a layer thickness of maximum 100 meters was required in the idealized ISOMIP cavity configuration[9] to resolve the ice shelf-ocean processes. Calculated mean melt rate did not significantly vary when increasing the vertical resolution beyond 100 meters.

Moreover, the partial cell treatment of ice shelf base topography in the z-coordinates model requires that hydrographic properties and current velocities underneath the ice shelf be vertically averaged over a fixed-depth mixed layer when calculating both the friction velocity u^* and the thermal forcing. The solution for the melt rate and streamfunction are otherwise noisy. This effect can be understood by considering again a grid cell intersecting the ice shelf base, hence partially dry and in immediate horizontal contact with fully wet cells. Since temperature tendencies in the model are proportional to the heat flux per grid-cell *wet* volume, temperature in fully wet grid cells will vary more slowly than in neighboring cells with a non-zero dry fraction. Therefore, the mixed layer temperature will relax more quickly to the local freezing point in cells with a large dry fraction. The diffusive heat flux through the boundary layer Q_M^T being proportional to the temperature difference between the mixed layer and ice shelf base, $T_M - T_B$, melt rates will be lower in partially dry cells than in wet cells. The same effect also applies to salt tendencies and results in jumps in the melt rate pattern

[9] an ice shelf with morphology represented in figure 2, with draft monotonically increasing from 200 to 700 meters, hence very similar to the current idealized configuration

along the ice shelf base where topography intersects a vertical layer. Consequently, where the ice shelf base intersects a grid cell, the mixed layer properties (T_M, S_M and $\mathbf{U_M}$) need to be averaged over a the depth of one vertical layer. The averaging scheme is described in details by Losch 2008. The inclusion of a velocity-dependent parameterization of the turbulent transfers necessitates extra averaging steps for the ocean current velocities underneath the ice shelf. Because the velocity components are defined on a C-grid, u_M and v_M needs first to be averaged horizontally, taking into account the ocean filled fraction of horizontally adjacent cells. Similarly, w_M needs to be averaged vertically. The resulting velocity components are collocated with T_M and S_M at the center of the grid cell just underneath the ice shelf. If the fixed thickness boundary layer intersects the grid cell immediately below the cell underneath the interface, horizontal averaging is also applied to this grid cell. The boundary layer averaging scheme that is then applied to the resulting mixed layer current components is identical to that used for the scalar T_M and S_M.

The extension of the fixed thickness boundary layer into cells not immediately adjacent to the ice shelf base results in an artificial increase of vertical mixing in the mixed layer (Losch, 2008). Because over most parts of the cavity, the temperature and salinity in the grid cells subject to melting at the shelf base is lower than that of the cell just below, the averaging increases T_M and S_M, allowing warmer and saltier water to be in contact with the ice. The net effect is an increase in simulated mean melt rates. The same is also true for ocean currents: averaging increases mixed layer currents speeds over most of the ice-covered part of the domain, thereby increasing the friction velocity and with it, the melt rates. The difference in melt rates associated with the use of the boundary layer scheme are illustrated in figures 4 for velocity-dependent experiments performed in an idealized cavity configuration. The averaging of temperature and salinity and of mixed layer currents account for a maximum of about 30% and 60% of the difference in melt rates respectively over the regions of fastest melting. Larger differences occur over regions of very slow melting[10]. The patchy spatial distributions of figure 4 are indicative of the noise present in the model solutions when no averaging of the mixed layer properties are performed. Although the differences show in figure 4 are significant in some places and result in a stronger circulation in the cavity, the structure of the circulation (not shown) and spatial patterns of melting are preserved under the averaging scheme. And while artificially increasing both the melt rate and circulation might seem undesirable, one can think that this boundary layer scheme mimics to very first order the effects of entrainment of warm water from below by the turbulent plume. The entrainment process is actually though to be an important factor on the buoyancy of the meltwater plume and the on melt rate especially at depth, where the ambient waters are the warmest (MacAyeal, 1984a, 1985; Jenkins, 1991; Holland and Feltham, 2006; Payne et al., 2007; Holland, 2008), and it is not explicitly parameterized in the present formulation of thermodynamic ice-ocean interactions.

In the present model, the inconveniences of the use of z-coordinates for representing ice shelf cavities mentioned above have been addressed in the following ways. The configuration uses a spherical polar grid at the $1/8°$ or $1/32°$ resolution (equivalent to a cell width of approximately 4 km and 1 km respectively) with 50 vertical levels of 20 meters each, such that the ice shelf topography is well resolved. Boundary layer averaging effectively reduces the noise associated with the partial-cell treatment. Biharmonic viscosity is used to damp the noise in the velocity fields associated with excitation of grid-scale waves. Weak stationary noise patterns still remain but do not affect the numerical stability of the solution.

The two model versions using the velocity-independent or velocity-dependent parameterization of the turbulent transfers velocities are referred to in the following as the 'velocity-independent' and the 'velocity-dependent' model respectively. Simulations using the two formulations are compared to identify the effect of including the

[10]The differences are overall lower for velocity-independent experiments and obviously in these cases, applying the scheme to ocean currents underneath the ice shelf does not significantly impact the melt rates.

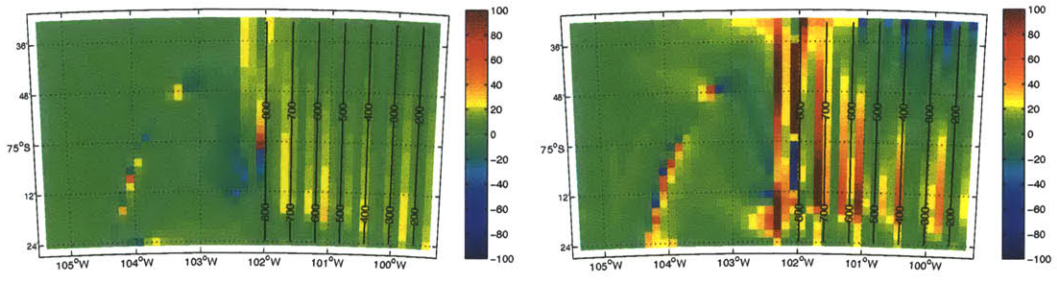

(a) no ML averaging scheme for T, S

(b) no ML averaging scheme

Figure 4: Difference in melt rates between experiments using the mixed layer averaging scheme for temperature, salinity and ocean currents and simulations using (a) no averaging scheme of temperature and salinity and (b) no averaging scheme at all, calculated using the velocity-dependent parameterization of the turbulent transfer velocities. Positive percent differences indicate that the averaging scheme results in higher melt rates. The maximum melt rates occur over the southeastern portion of the cavity and along the southern boundary. There, differences in melt rates attributed to averaging of temperature and salinity and to the full boundary layer scheme reach about 30% and 60% respectively.

transfer of ocean momentum in the formulation of turbulent heat and salt exchanges at the ice-ocean interface on the magnitude and spatial distribution of the melt rates. Two types of experiments are performed, one using a highly idealized ice shelf cavity, the other a realistic configuration of the cavity underneath Pine Island Ice Shelf in the Amundsen Sea embayment.

3.2 Realistic experiments

In the realistic experiments, the model domain is delimited by the 102°20′ W and 99°22′ W meridians and the 74°30′ S and 75°27′ S parallels and covers an area encompassing the Pine Island Glacier ice shelf. The portion of the cavity south of about 75°50′ S is is referred to in the following as PIIS proper and is more extensively analyzed than the area to the north, which is much less dynamically active (Payne et al., 2007). The ice shelf topography and the bathymetry of the sea floor are obtained from Timmermann et al. (2010). Ice draft and cavity bathymetry over PIIS in this data was interpolated form the AUTOSUB data of Jenkins et al. (2010a). The sea floor reaches a maximum depth of about 1000 meters and the ice shelf draft varies between 200 m at the ice shelf front and about 900 meters at the grounding line. Another important feature of this data set is the presence of a sill of about 300 meters in height oriented in the southwest-northeast direction and approximately half-way between the ice shelf front and the deepest reaches of the grounding line in the southeastern corner of PIIS proper (see figure 5). The northern, southern and eastern boundaries of the realistic domain are closed. Time-independent vertical profiles of the zonal ocean velocity, ocean potential temperature and salinity are prescribed at the western open boundary (solid curves on figures 6a, 6b and 6c respectively). These are the same profiles as recently used in the MITgcm ice shelf modeling study of Heimbach and Losch (2012) (from M. Schroeder, personal communication). They are estimated from in situ data provided by five hydrographic stations located along the ice shelf front and are uniform in the meridional direction. Relatively fresh and cold water leaves the cavity at the surface and warm, salty water enters the cavity at depth.

3.3 Idealized experiments

The idealized model configuration serves to examine the effects of including the ocean velocity-dependence in the turbulent ice-ocean transfers on the melt rates and ocean circulation underneath the ice shelf. The ice shelf topography and bathymetry in these experiments are also varied in order to investigate the feedbacks between thermodynamic processes and both ice shelf topography and bathymetry of the sea floor.

The rectangular domain is delimited by the 105°30′ W and 99°22′ W meridians and by the 74°30′ S and 75°27′ S parallels. Its eastern half is covered by a meridionally-uniform ice shelf and the western half is an open ocean that exchanges neither heat nor mass with the atmosphere above and serves as a sponge layer between prescribed open boundary conditions and the cavity interior. The cavity geometry is representative of the typical ice shelf morphology (characterized by a near-vertical ice shelf front a few hundreds of meters tall, separated from a 1 km deep grounding line by a steady base slope of 0.5 m/km) and scaled to be consistent with the specific case of PIIS. In experiments in which neither ice shelf topography nor the bathymetry is varied, the ice shelf base depth increases monotonically from 200 meters at the ice shelf front to 900 meters depth at the grounding line. The seabed is flat and at a depth of 1000 meters. The southern, northern and eastern boundaries are closed. At the western open boundary, time independent and meridionally uniform profiles of zonal velocity, ocean temperature and salinity are prescribed (dashed curves on figures 6a, 6b and 6c respectively). These profiles were chosen to be consistent in magnitude and shape with the climatological profiles used in the realistic experiments and hence to represent the conditions at the mouth of a typical 'warm' ice shelf, i.e., an ice shelf in contact with CDW. In particular, the sinusoidal profile of zonal velocity insures a zero net volume flux at the open boundary. The circulation and melt rates are relatively not sensitive to the specific magnitude of the zonal current prescribed at the open boundary as long as it does not significantly exceeds the magnitude of the barotropic circulation in the cavity.

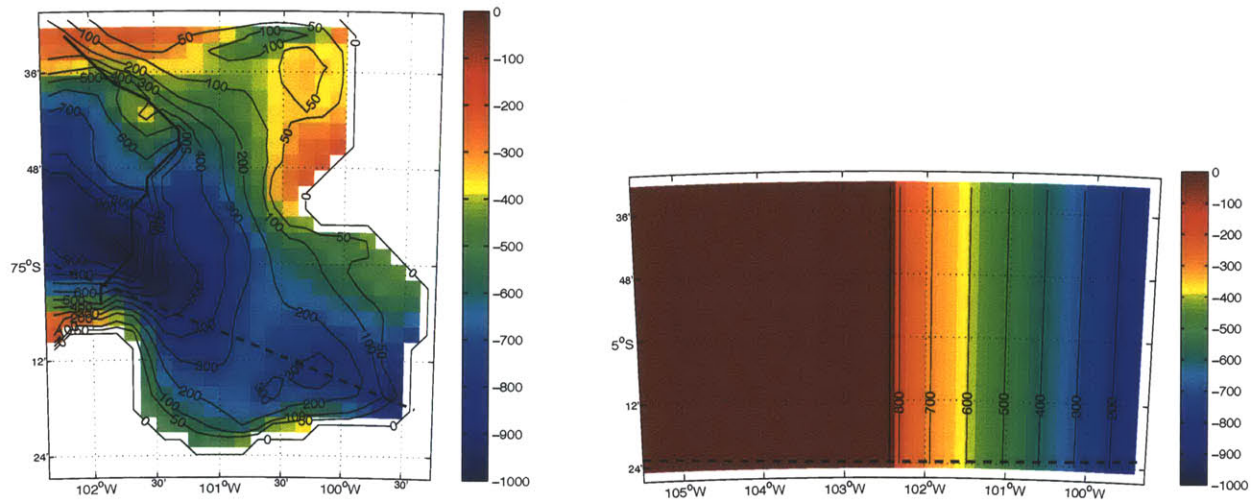

(a) Realistic setup

(b) Idealized setup

Figure 5: (a) Geometry of the ice shelf cavity in the realistic experiments. Shading is used for the bathymetry (m) and contours show the water column thickness (m). (b) Geometry of the idealized cavity. Shading indicates the depth of the ice shelf base (m) and contours, the water column thickness (m). The solid black line indicates the ice shelf front in both cases. Cross-sections of hydrographic properties shown in the following are taken along the dashed black lines (unless stated otherwise).

3.4 Initial and boundary conditions

As in most ice cavity models, the ice shelf base is maintained fixed regardless of the melting and refreezing in both the idealized and realistic simulations (eg., MacAyeal, 1984a,b,c, 1985; Jenkins, 1991; Determann and Gerdes, 1994; Grosfeld and Gerdes, 1997; Holland and Feltham, 2006; Payne et al., 2007; Holland and Jenkins, 1999; Schodlock et al., 2012; Mueller et al., 2012). This implies that the ice shelf is continuously replenished by snow accumulation and by the flow of the ice sheet upstream, an assumption somewhat justified by comparing the time scales of the ocean circulation in the cavity and of the slowly moving ice shelf (Holland and Jenkins, 1999). The weight of the ice shelf is provided at the top of the water column as an additional boundary condition. It is computed by integrating a time-independent density profile ρ^* corresponding to the sea-water replaced by ice, from $z = 0$ to a reference ice-shelf draft. Underneath the ice shelf, the sea-surface height η is the deviation from this reference ice shelf draft. The pressure anomaly used to compute pressure gradients in the model is obtained by subtracting the depth-dependent contribution $-g\rho_{ref}z$, where ρ_{ref} is a reference density calculated from the total pressure. Non-hydrostatic contributions to the pressure anomaly are neglected. A convective adjustment scheme parameterizing vertical convection is used in case of unstable conditions.

The boundary conditions prescribed at the western open boundary in both the realistic and idealized experiments are illustrated in figures 6a, 6b and 6c. When tidal forcing is added, the open boundary conditions include a time-evolving zonal barotropic tidal current. They are read every time step and repeated over each tidal cycle. The response of the idealized cavity to tidal currents of various amplitudes is investigated. In the realistic experiments, the prescribed barotropic tidal currents are based on the outputs of the Circum-Antarctic Tidal Simulation (CATS02.01) model developed by Padman et al. (2002). This shallow water model is forced with sea surface height tidal signals from the global inverse model TPXO6.2 and astronomical forcing (and tuned to data using a linear benthic drag coefficient). It covers the entire circum-Antarctic ocean up to the 58°S parallel, with a resolution of $\frac{1}{4}^\circ \times \frac{1}{12}^\circ$, that is, approximately 10 km, and includes ice shelf cavities. A meridionally uniform zonal tidal current consistent with the model output at 74.8°S and 102.375°W is employed. This location corresponds to the midpoint along the open ocean part of the western boundary in the realistic experiments. The CATS02.01 prediction of the eight dominant tidal signals at this location is shown in figure 6d over a 24 hours cycle. The total diurnal and semi-diurnal signals are shown in figure 6e (solid curves). The amplitude of these signals over the 24 hours period shown in figure 6e was employed to construct mono-periodic diurnal and semi-diurnal tidal currents for forcing of the realistic simulations. The use of such idealized mono-periodic tidal signals simplifies the investigation of the cavity's response to the two principal tidal frequencies.

It is also important to note that we choose to use the forward CATS02.01 model although CADA10, which assimilates TOPEX/Poseidon satellite radar altimetry and coastal and benthic tide gauges data, is also available for the Circum-Antarctic region. This is because CADA10 is known to be generally not as good at CATS02.01 because it employs out-of date bathymetry and coasts data (CATS (2012), `www.esr.org/polar_tide_models/Model_CATS0201.html`). Moreover, Padman et al. (2002) point out that tide data is particularly sparse in the Pine Island Bay. At 74.8°S and 102.375°W, the zonal tidal current amplitude outputs from the two models differ within a few percents only.

All idealized, realistic, tidally forced and unforced simulations are started from rest. The initial temperature and salinity profiles are uniform both meridionally and zonally, and correspond to the western open boundary profiles. A spinup of three years is performed to reach steady state melt rate and hydrographic conditions (see figure 7). Monthly averaged fields corresponding to the last month of the spinup are analyzed (the results do not differ by the choice of snapshot or monthly averaged fields since the model is in steady state after the spinup). For simulations forced with tides, 2-hourly snapshots are analyzed over a 2.5 days period following

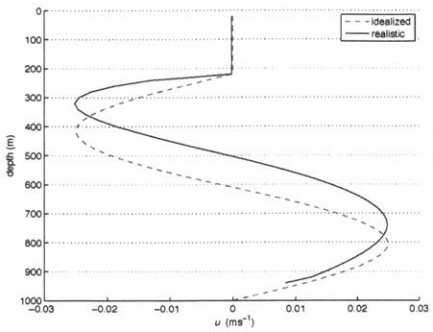

(a) u-velocity (ms^{-1})

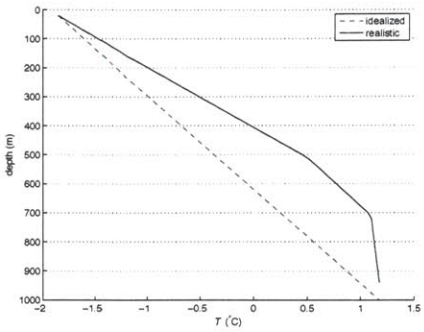

(b) Temperature (°C)

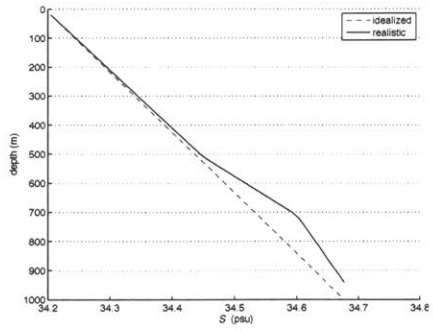

(c) Salinity (psu)

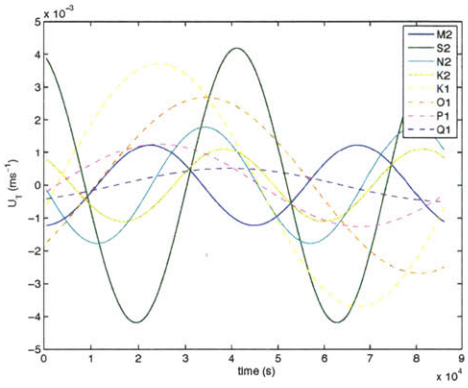

(d) tidal signals at 74.8°S, 102.375°W from CATS02.01

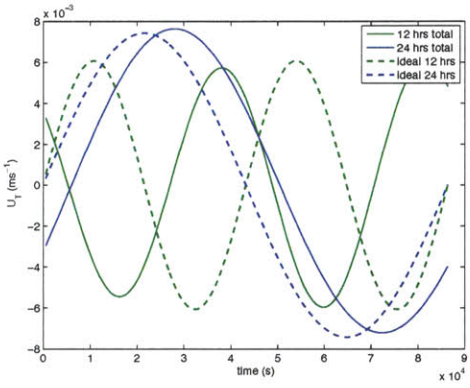

(e) tidal forcings for realistic model simulations

Figure 6: Vertical profiles of (a) zonal velocity, (b) temperature and (c) salinity prescribed as the western open boundary conditions in the idealized and realistic experiments. Profiles are all uniform in the meridional direction. (d) 24 hours time series of the main tidal signals at 74.8°S and 102.375°W from the CATS02.01 tidal model. (e) Sum of the diurnal ('24 hrs total', plain blue line) tidal signals and of the semi-diurnal ('12 hrs total', plain green line) principal tidal signals shown in (d). The dashed blue and green curves are the idealized mono-periodic diurnal and semi-diurnal tidal signals constructed using the amplitude of the 'total' diurnal and semi-diurnal signals respectively and are used as the tidal forcings in the realistic experiments.

the 3-years spinup. All simulations presented in the following were run with the $\frac{1}{8}^\circ$ resolution instead of the higher ($\frac{1}{32}^\circ$) resolution model. This choice was made in order to minimize computational costs and run times. Table 2 summarizes the characteristics of each set of experiments performed and indicates in which part of the Results section (section 4) it is discussed.

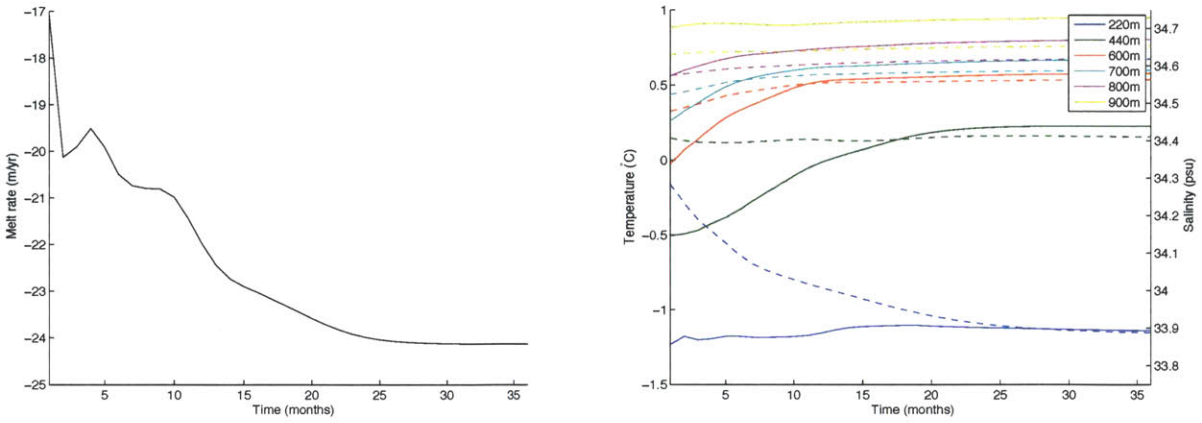

(a) m (b) T, S

Figure 7: Evolution during model spinup of the monthly mean and area averaged (a) melt rate, (b) potential temperature (solid lines) and salinity (dashed lines) at 6 depth levels underneath the ice shelf. The 3-years spinup shown here uses the $1/8^\circ$ resolution model in the idealized cavity setup.

Section	setup	$\gamma_{T,S}$ formulation	C_d	bathymetry	shelf base slope	tidal forcing
4.1						
4.1.1	idealized	vel-dep. & index.	default	flat	default	—
4.1.2	realistic	vel-dep. & indep.	default	—	—	—
4.2						
4.2.1	idealized	vel-dep.	1/16 to 16 × default	flat	default	—
4.2.2	realistic	vel-dep.	1/16 to 16 × default	—	—	—
4.3						
4.3.1	idealized	vel-dep. & indep.	4 × default	flat	gentle, default, steep	—
4.3.2	idealized	vel-dep. & indep.	4 × default	flat, downslope, upslope	default	—
4.4						
4.4.1	idealized	vel-dep. & indep.	4 × default	flat	default	$\omega = 12\text{hr}^{-1}, 24\text{hr}^{-1}$
	realistic	vel-dep. & indep.	default	—	—	$\omega = 12\text{hr}^{-1}, 24\text{hr}^{-1}$
4.4.2	idealized	vel-dep. & indep.	4 × default	flat	default	$\omega = 24\text{hr}^{-1}$
	realistic	vel-dep. & indep.	default	—	—	$\omega = 24\text{hr}^{-1}$
4.4.3	idealized	vel-dep.	4 × default	sill/trough	default	$\omega = 24\text{hr}^{-1}$
4.4.4	idealized	vel-dep. & indep.	4 × default	flat	default	$\omega = 24\text{hr}^{-1}$
	realistic	vel-dep. & indep.	1, 4, 16 × default	—	—	$\omega = 24\text{hr}^{-1}$

Table 2: Description of the model simulations performed in each sub-section of section 4. For each set of experiments, the cavity setup, formulation of the turbulent exchange velocities, value of the drag coefficient, characteristics of the bathymetry and ice shelf base slope and frequency of tidal forcing used are given.

4 Results

4.1 Comparison of the velocity-dependent and velocity-independent parameterizations

4.1.1 Idealized experiments

As mentioned in the theory section (2), most models of ice shelf-ocean interactions in an idealized cavity with north-south orientation, as represented in figure 2, place maximum melt rates along the grounding line and over the eastern position of the cavity (e.g., MacAyeal (1984a,b); Hellmer and Olbers (1989); Jenkins (1991); Determann and Gerdes (1994); Grosfeld and Gerdes (1997); Holland and Jenkins (2001); Holland and Feltham (2006); Holland et al. (2008); Little et al. (2008); Losch (2008), and many others). This is where inflowing warm waters at depth first reach the ice shelf base, hence where the largest differences between the in situ ocean mixed layer temperature and freezing point temperature ($T_M - T_B$) occur. According to equation (6), the diffusive heat flux through the boundary layer is directly proportional to this temperature gradient. Scaling appropriate to the ice shelf cavity environment indicates that Q_M^T is the dominant forcing term on melt rates (Holland and Jenkins, 1999). Hence high melt rates are indeed expected over areas of large temperature gradients across the ice-ocean boundary layer.

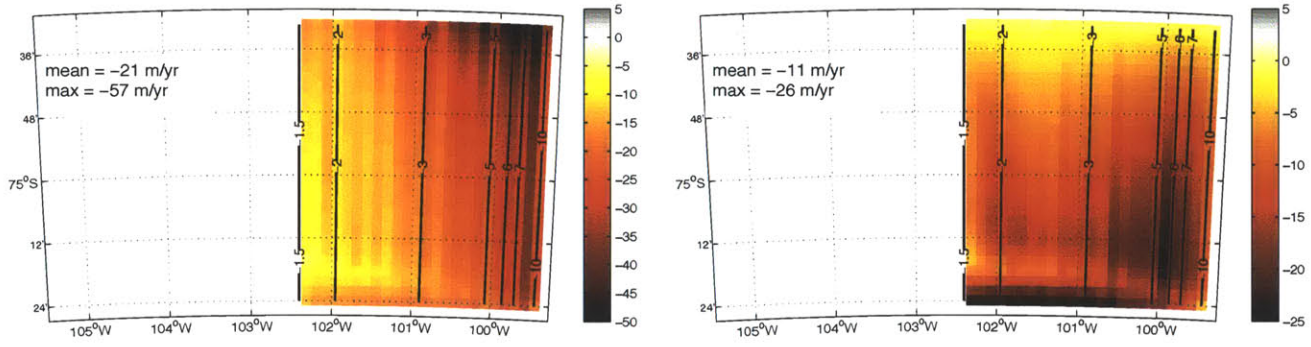

(a) velocity-independent $\gamma_{T,S}$

(b) velocity-dependent $\gamma_{T,S}$

Figure 8: Melt rate simulated using (a) the velocity-independent and (b) the velocity-dependent parameterization of the turbulent exchange velocities in the idealized cavity setup. Black contours show the distribution of background potential vorticity f/h (in $10^7 \mathrm{m}^{-1}\mathrm{s}^{-1}$). The maximum and cavity-averaged melt rates are given in the top left corner of each panel. Different scales are used to clearly bring out the spatial pattern of melting in both cases.

Figure 8a for the melt rates underneath an idealized ice shelf show that the present model is consistent with the results of these previous modeling studies when employing the velocity-independent parameterization of Hellmer and Olbers (1989) for the turbulent exchange velocities. Maximum melt rates are found along the grounding line over the northeastern corner of the cavity. In the present east-west oriented domain, this is where the warmest waters first reach the ice shelf base and hence where the largest temperature gradients across the boundary layer occur (as shown in figures 11a and 11b for the thermal forcing, $T_M - T_B$). The sign of the zonally-integrated overturning transport in the cavity (see figure 9c) suggests that meltwater mixes with ambient water at this location and forms a fresh buoyant plume that rises along the ice shelf base. This cold and fresh meltwater plume is clearly distinguished on zonal cross sections of potential temperature and salinity

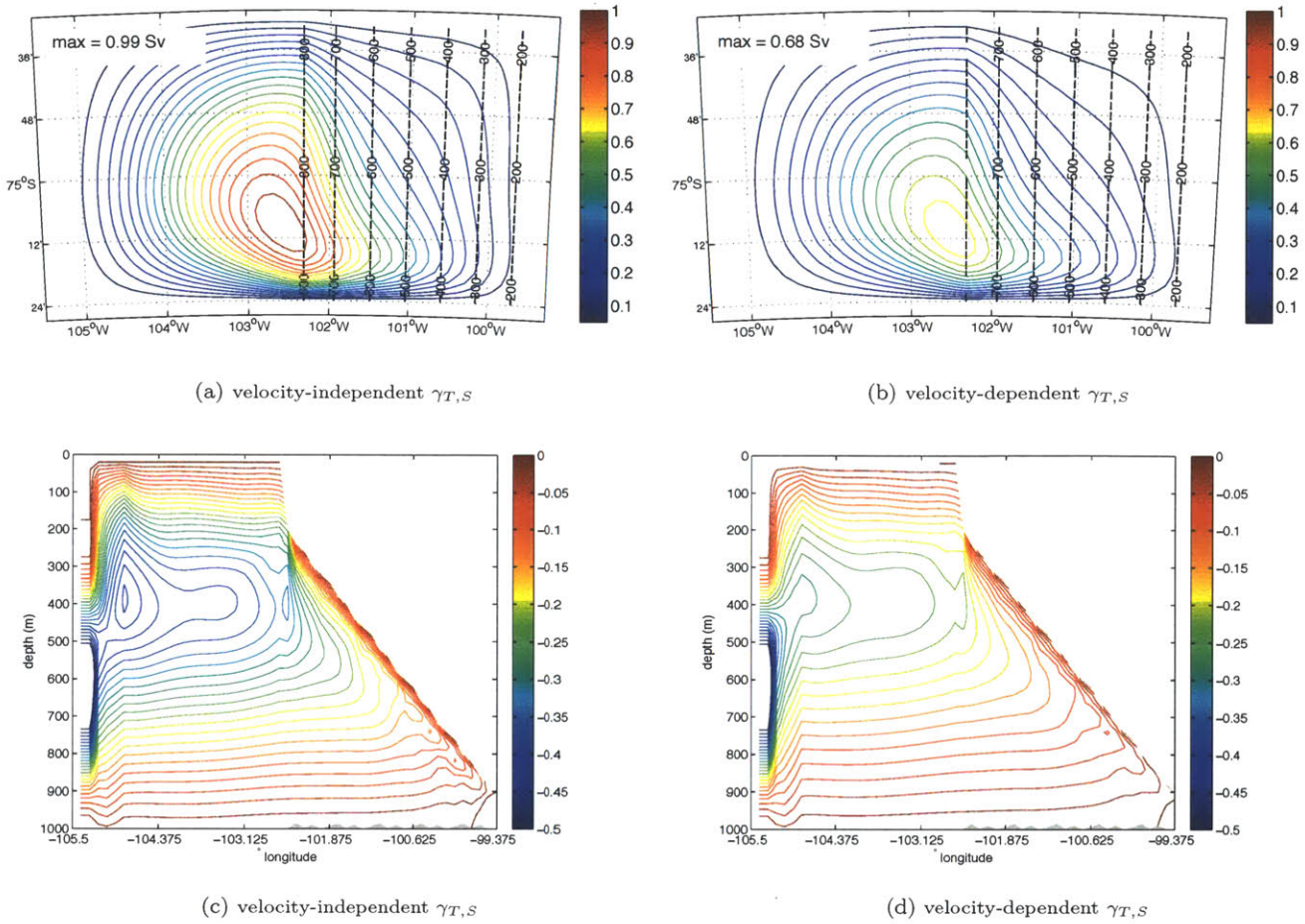

(a) velocity-independent $\gamma_{T,S}$

(b) velocity-dependent $\gamma_{T,S}$

(c) velocity-independent $\gamma_{T,S}$

(d) velocity-dependent $\gamma_{T,S}$

Figure 9: (a, b) Barotropic streamfunction for the depth-integrated horizontal volume transport (Sv) calculated using (a) the velocity-independent and (b) the velocity-dependent parameterization of the turbulent exchange velocities. The maximum value of volume transport is indicated in the top left corner of each figure. Black dotted contours show the water column thickness distribution, h (m). (c, d) Baroclinic streamfunction for the meridionally-integrated zonal overturning circulation (Sv) calculated using (c) the velocity-independent and (d) the velocity-dependent form of the parameterization of the turbulent exchange velocities.

underneath the ice shelf (see figures 10a and 10c), at 75.375°S, that is, across the westward outflowing branch of the barotropic cavity circulation. Theory behind the closed ice pump[11] dynamics predicts that the rising buoyant plume will eventually reach a level at which its temperature matches the in situ freezing temperature. Beyond this point, it is supercooled with respect to the ambient ocean. The plume can therefore refreeze and ice can accumulate at the ice shelf base. Brine rejection upon refreezing will cause densified water from the near surface layers to sink. This downwelling will supply latent heat for melting at the grounding line and thereby close a self-sustaining overturning circulation underneath the ice shelf. This picture is consistent with the circulation underneath large ice shelves in contact with High Salinity Shelf Water at the surface freezing temperature created upon sea ice formation close to the ice shelf edge. On the other hand, if the plume does not reach a level at which its density becomes equal to the in situ ocean density, it escapes the cavity as a fresh

[11] ice pump circulation in a domain forced by nothing but the heat flux at the ice interface associated with the pressure dependence of the freezing point and in which freshwater fluxes resulting from melting and refreezing must therefore be equivalent

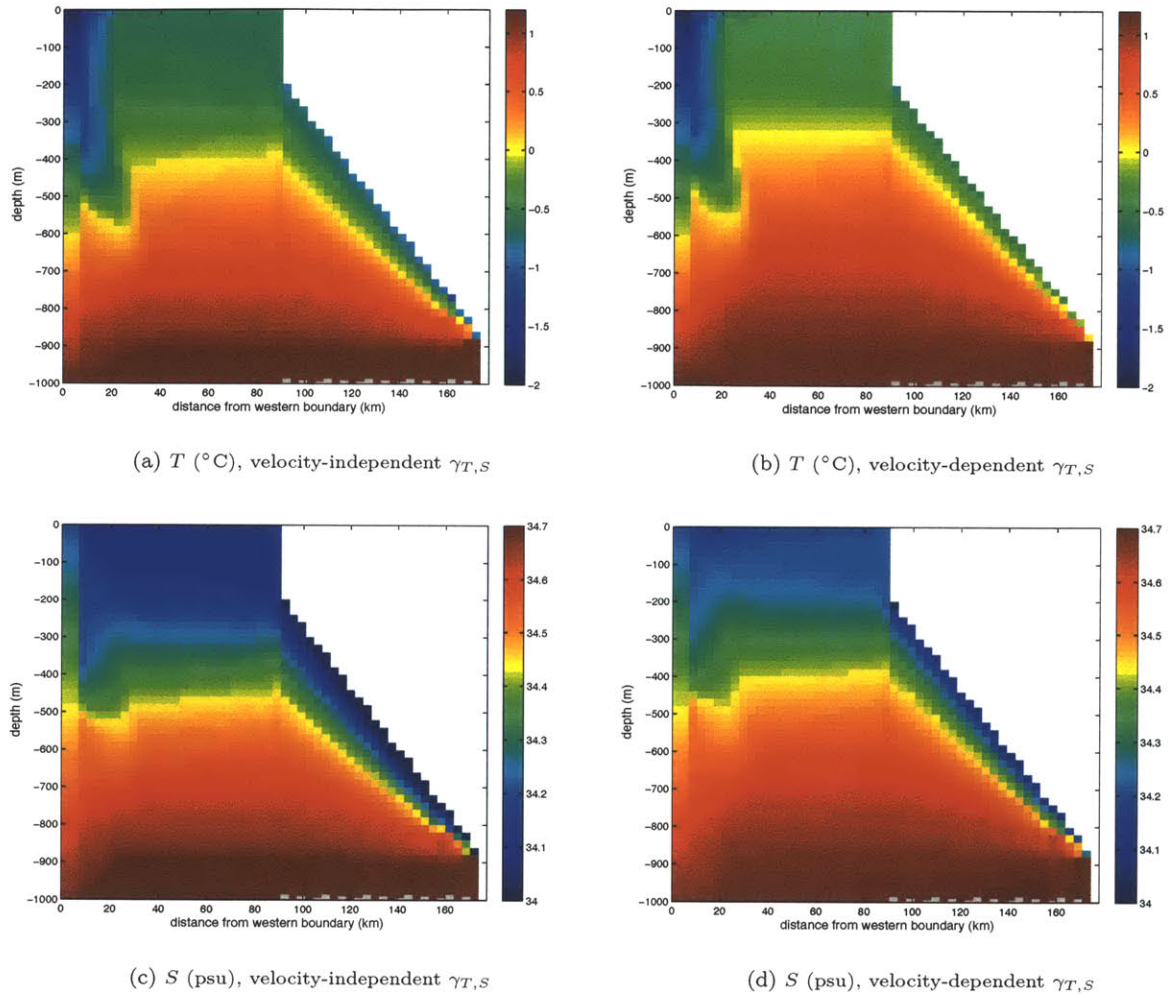

(a) T (°C), velocity-independent $\gamma_{T,S}$

(b) T (°C), velocity-dependent $\gamma_{T,S}$

(c) S (psu), velocity-independent $\gamma_{T,S}$

(d) S (psu), velocity-dependent $\gamma_{T,S}$

Figure 10: Vertical cross-sections of potential temperature (upper panels) and salinity (lower panels) along 75.375°S, simulated using (a, c) the velocity-independent and (b, d) the velocity-dependent parameterization of the turbulent exchange velocities.

and cold water mass and hence interacts with the open ocean. It is the case in the present simulations. Figure 8a indicates that the idealized ice shelf does not support basal refreezing[12] and figure 9c show no sinking branch of the overturning circulation close to the ice shelf front. Holland et al. (2008) pointed out that such conditions are consistent with small and steep ice shelves in contact with Circumpolar Deep Water with temperature of 1°C and over. Observations from Jacobs and Hellmer (1996) also suggest no refreezing under the small ice shelves of the Amundsen Sea and plume outflows under PIIS that reach temperatures up to 2°C above freezing. Here, ocean temperatures prescribed at the open boundary reach the maximum associated with the climatological conditions retrieved for PIIS, that is over 1.0°C indeed (exactly 1.18°C). The structure of the simulated overturning circulation is therefore consistent with the work of Holland et al. (2008) and observations from Jacobs and Hellmer (1996). The absence of downwelling in front of the ice shelf could also be explained by the dominance of the zonal circulation prescribed at the western boundary. However, experiments in which no ocean currents were prescribed did not support refreezing and downwelling at the ice shelf edge either (results not shown).

[12]As mentioned in section 3, the model does not parameterize sea ice or frazil ice formation.

The structure of the horizontal circulation simulated with the velocity-independent model is also very similar to that obtained in earlier modeling studies (eg., Determann and Gerdes, 1994; Grosfeld and Gerdes, 1997; Holland and Jenkins, 2001; Holland and Feltham, 2006; Holland et al., 2008; Losch, 2008) and in agreement with the cavity dynamics described in section 2. The streamfunction for the vertically-integrated volume transport (figure 9a) shows a cyclonic gyre covering the whole domain. In the eastward branch of the gyre, warm water from the open ocean entering the cavity is diverted along the northern boundary, consistent with a buoyancy-induced cyclonic circulation set up by melting at the ice shelf base. From the northeastern corner of the cavity, where maximum melt rates occur, the water mass formed through mixing of meltwater and ambient water flows southward along the ice shelf base. Melt rates decrease southward as the plume becomes more diluted with meltwater and exhausts its heat potential. The barotropic transport streamfunction indicates an intensification of the westward flowing branch along the southern boundary, which is consistent with the intensification an ageostropic flow against the background potential vorticity gradient. In particular, the near-meridional orientation of contours of f/h (see figure 9a) is consistent with the idea of Little et al. (2008) that water column thickness dominates over planetary rotation in setting the background potential vorticity gradient underneath ice shelf cavities. The control of water depth distribution on the cavity circulation is even more obvious in the present atypically-oriented domain since topographically-induced and rotation-induced potential vorticity gradients are perpendicular to each other.

The main difference between our velocity-independent model results and that of previous studies is that the cyclonic gyre is not restricted to the cavity but extends over the whole domain. This is consistent with the absence of freezing-induced downwelling at the ice shelf edge and with the 'overshooting" of the meltwater plume out of the cavity. It likely increases barotropic exchanges between the open ocean and ice shelf cavity relative to the typical 'cold' ice shelf circulation (Grosfeld and Gerdes, 1997; Losch, 2008). The shift in the orientation of transport streamlines across the ice shelf edge however suggests that the ice front acts to some extent as a topographic barrier for the cavity circulation. Plotting the velocity in the uppermost ocean layer (the mixed layer underneath the ice shelf and surface layer over the open ocean) actually shows a separation of the flow inside and outside the cavity into two surface circulations. A cyclonic circulation characterizes the ice-shelf covered part and an anticyclonic gyre is set over the open ocean part of the domain (see figures 11c and 11d). The absence of signature of the surface circulation in the depth-integrated volume transport streamfunction indicates that the circulation in mid and deep layers dominates over that of the upper layers in setting structure of transport over the domain and is thus in agreement with the results of Little et al. (2008) described earlier.

The idealized model using the velocity-dependent parameterization of the turbulent exchange velocities (and the default drag coefficient value of $1.5 \cdot 10^{-3}$) simulates a depth-integrated volume transport and a meridionally averaged overturning circulation with structure very similar to that of the velocity-independent experiment (see figures 9b and 9d). However, the spatial distribution of melt rates differs largely between the two simulations. In the velocity-dependent case, the maximum melt rates are found along the exiting path of the meltwater plume, that is, over the intensified westward branch of the cyclonic circulation along the southern edge of the cavity, and over an area extending westward from the southern part of the grounding line. No local melt rate maximum is seen over the northeastern corner of the cavity. The correspondence between the overturning and horizontal circulations simulated in the two experiments implies that hydrographic properties inside the cavity must be similarly distributed in both cases. The disparities in melting patterns therefore suggests that the melt rate is not as sensitive to ocean temperature in the velocity-dependent than in the velocity-independent simulations, i.e., that the effect of mixed layer currents dominate over the effect of thermal forcing in setting the diffusive heat flux through the ice-ocean boundary layer in the velocity-dependent case.

To verify this assumption, we compare the velocity-independent and velocity-dependent melt rate patterns to the distributions of the two main drivers of the diffusive heat flux (Q_T^M), which according to equations (6) and (9) are the difference in temperature across the boundary layer, $T_M - T_B$, and, through the formulation of the friction velocity, the magnitude of mixed layer current velocities, U_M (figure 11). As expected from the similitude between the barotropic and overturning circulations, and magnitudes aside, the spatial patterns of both the thermal forcing and mixed layer velocity are very similar in the velocity-independent and velocity-dependent simulations. In both cases, the highest gradients of temperature across the ice-ocean boundary layer are found over the northeastern corner of the cavity, where warm water first reach the ice shelf base. Highest mixed layer current speeds are concentrated along the southern cavity wall over the region of plume outflow, and increase southward over the interior part of the cavity. The spatial correlation between the melt rates and either forcing is however very different between the two simulations: while in the velocity-independent case, maxima in melt rates are collocated with maxima in thermal forcing and are seemingly insensitive to details in mixed layer velocity pattern, in the velocity-dependent case, melt rates are not spatially correlated with thermal forcing but seem constrained by the distribution of U_M.

This migration of the maximum melt rates from the areas of high ocean heat to regions of strong currents is consistent with results of Mueller et al. (2012). In a recent modeling study of Larsen C Ice Shelf, they compared a simulation of a three-dimensional ice shelf-ocean model in which they used the velocity-dependent melt rate parameterization of Holland and Jenkins (1999) to another in which they employed the velocity-independent formulation of Hellmer and Olbers (1989). They observed that between the two experiments, maximum melt rates migrated from the regions of strongest time-independent barotropic currents to the the vicinity of the grounding lines, where T_B is lowest and the thermal forcing, highest.

The magnitude of the mixed layer currents, the melt rates and cavity circulations are all smaller in the velocity-dependent than in the velocity-independent simulation. This is explained by the fact that the constant thermal exchange velocity used in the velocity-independent parameterization of Hellmer and Olbers (1989) is an upper bound to typical values of γ_T obtained from the velocity-dependent parameterization of Jenkins (1991) or Holland and Jenkins (1999). Such high value of γ_T corresponds to a spatially uniform mixed layer velocity of 0.2 ms^{-1}. It is therefore higher than most estimates of U_M associated with the thermohaline circulation underneath ice shelves. Instead, it would be more consistent with the presence of strong tidal flow in the cavity (Holland and Jenkins, 1999). Figure 11d indeed indicates that currents as fast as 0.2 ms^{-1} occur only over small portions of the cavity when using the default value of drag coefficient. This is again in agreement with the study of Mueller et al. (2012), who noticed that the strength of ocean currents was overestimated in their velocity-independent simulation.

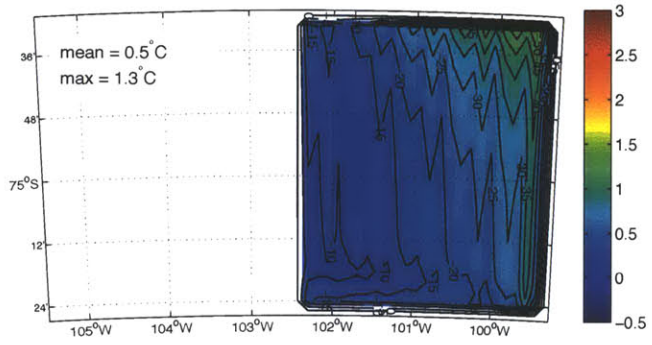

(a) $T_M - T_B$ (°C), velocity-independent $\gamma_{T,S}$

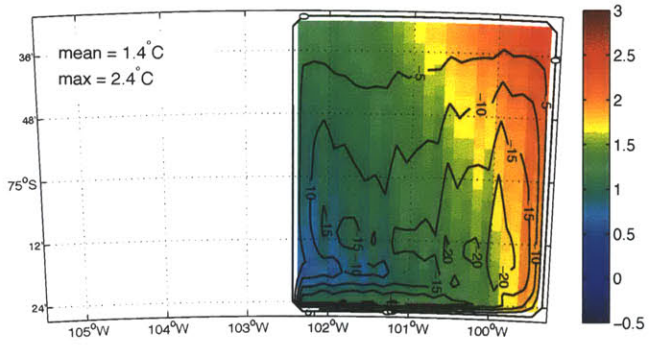

(b) $T_M - T_B$ (°C), velocity-dependent $\gamma_{T,S}$

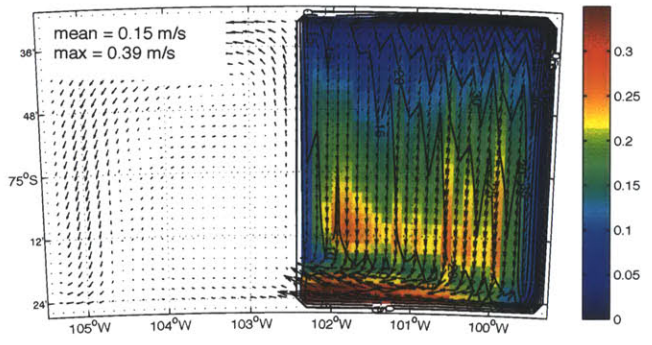

(c) U_M (ms^{-1}), velocity-independent $\gamma_{T,S}$

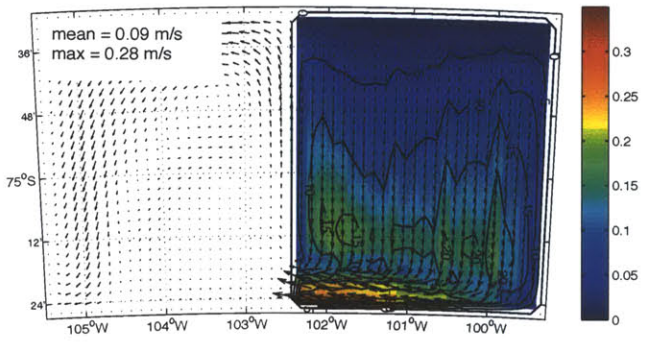

(d) U_M (ms^{-1}), velocity-dependent $\gamma_{T,S}$

Figure 11: (a, b) Thermal forcing (i.e., temperature difference across the ice-ocean boundary layer) simulated using (a) the velocity-independent and (b) the velocity-dependent parameterization of the turbulent exchange velocities in the idealized cavity setup. The values of area-averaged and maximum thermal forcing are indicated in the top left corner of the figures. (c, d) Ocean mixed layer velocity calculated using (c) the velocity-independent and (d) the velocity-dependent parameterization of the turbulent exchange velocities. The values of area-averaged and maximum mixed layer velocity are given in the top left corner of the figures. Vectors indicate the direction and relative magnitude of the mixed layer currents. On all figures, black contours show the spatial distribution of melt rates (m/yr).

4.1.2 Realistic experiments

Melt rates simulated for the realistic PIIS experiments using the velocity-independent and velocity-dependent (with $C_d = 1.5 \cdot 10^{-3}$) parameterizations of $\gamma_{T,S}$ are shown in figures 12a and 12b respectively. Patterns of temperature differences across the boundary layer ($T_M - T_B$) and of mixed layer velocities (U_M) are illustrated in figure 13 for both simulations. As in the idealized experiments, spatial patterns of $T_M - T_B$ and of U_M are very similar but important differences are seen in the melt rate distributions between the two cases.

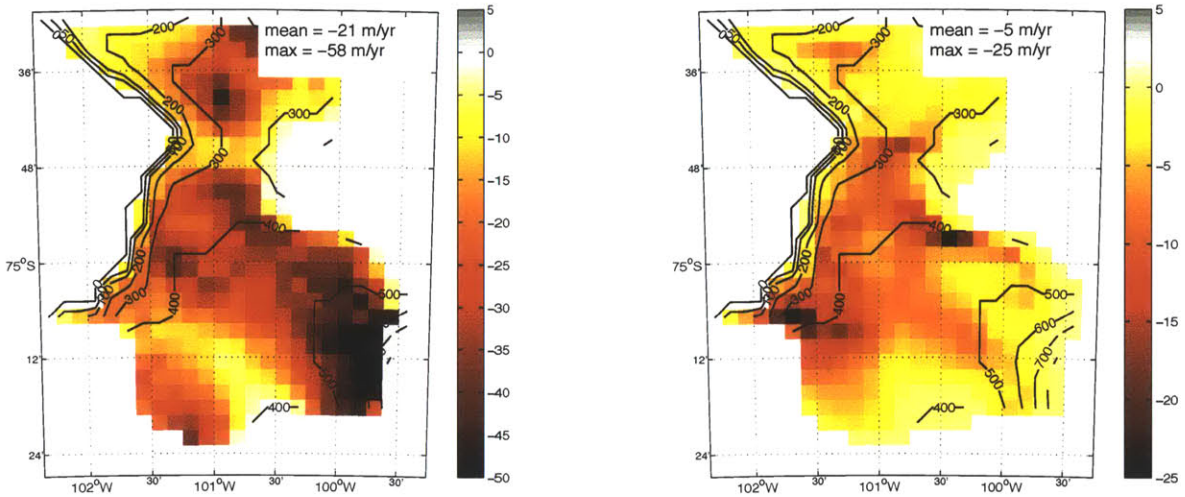

(a) velocity-independent $\gamma_{T,S}$ (b) velocity-dependent $\gamma_{T,S}$

Figure 12: Melt rate simulated using (a) the velocity-independent and (b) the velocity-dependent parameterization of the turbulent exchange velocities in the realistic PIIS setup. Black contours indicate the depth of the ice shelf base (m). The maximum and area-averaged melt rates are indicated in the top left corner of each panel. Different scales are used to bring out clearly the spatial distribution of melt rates in both cases.

As seen on figure 13a, the velocity-independent melt rates are still highly spatially correlated with the distribution of thermal forcing. Comparison with figure 12a showing the melt rate magnitude along with contours of the shelf base depth clearly indicates that the highest melt rates occur in the southeastern portion of the cavity where the ice shelf base is deepest, i.e. where T_B is lowest. Cross sections of temperature and salinity show that the warmest and most salty waters reach the grounding line in this area (see figures 15a and 15c), hence explaining the occurrence of the maxima in thermal forcing there. Comparison of the thermal forcing, melt rate pattern and background potential vorticity contours suggests that the presence of a southwest-northeast oriented sill halfway between the ice front and the deepest grounding line of PIIS proper constrains to some extent the spatial distribution of water properties, hence of ablation rates. Figure 14a shows the streamfunction for the vertically-integrated volume transport along with the distribution of f/h. As in the idealized experiments, the structure of the circulation suggests that the barotropic transport inside the cavity is strongly controlled by the distribution of water column thickness (nearly equivalent to the distribution of f/h). The circulation under PIIS proper is characterized by an extensive cyclonic gyre that brings warm water at depth in contact with the southeastern grounding line. Transport over the sill is weak. On each side of the sill, the circulation breaks into two smaller cyclonic gyres, separating regions of high melt rates upstream and downstream by a local minimum in thermal forcing.

On the other hand, comparison of figures 13b and 13d indicates that the melt rate simulated using the velocity-dependent parameterization of $\gamma_{T,S}$ is not spatially correlated with the temperature gradient across the boundary layer. Instead, it mimics the distribution of the mixed layer current magnitude, as in the idealized

experiments. Melt rate maxima in the realistic cavity setup are collocated with mixed layer outflows (see figure 13d). The spatial distribution of velocity-dependent melt rates in the realistic experiment is therefore consistent with that obtained in the idealized cavity setup: the highest melt rates in both simulations are collocated with rapid plume outflows. In the realistic case, the outflow around 75°06′S, 101°30′W is located at the convergence of the northwestward branches of both cyclonic circulations on the upstream and downstream side of the sill. The outflow around 75°00′S, 100°30′W coincides with the convergence of currents against the eastern cavity wall of PIIS. The steep topography there induces strong local potential vorticity gradients and promotes the intensification of the convergent geostrophic currents. A third weaker outflow collects melt water from the less dynamic northern portion of the cavity. Relatively high melt rates are also seen over the inflowing branch of the cyclonic gyre that dominates the circulation under PIIS.

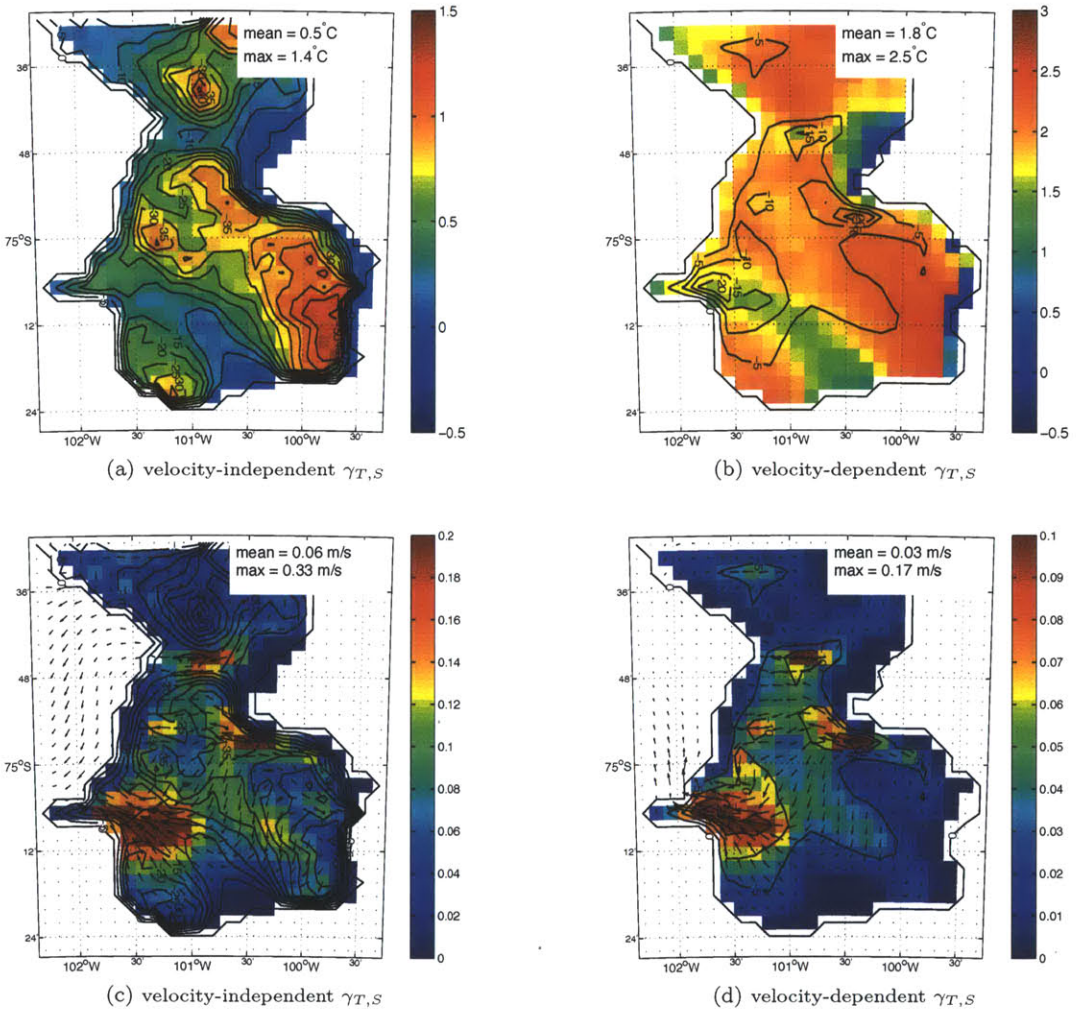

(a) velocity-independent $\gamma_{T,S}$

(b) velocity-dependent $\gamma_{T,S}$

(c) velocity-independent $\gamma_{T,S}$

(d) velocity-dependent $\gamma_{T,S}$

Figure 13: (a, b) Thermal forcing (i.e., temperature difference across the ice-ocean boundary layer) simulated using (a) the velocity-independent and (b) the velocity-dependent parameterization of the turbulent exchange velocities in the realistic PIIS setup. The values of area-averaged and maximum thermal forcing are indicated in the top left corner of the figures. (c, d) Ocean mixed layer velocity calculated using (c) the velocity-independent and (d) the velocity-dependent parameterization of the turbulent exchange velocities. The values of area-averaged and maximum mixed layer velocity are given in the top left corner of the figures. Vectors indicate the direction and relative magnitude of the mixed layer currents. In all panels, black contours show the spatial distribution of melt rates (m/yr). Different scales are used to bring out the spatial distribution of both forcings in each cases.

As in the idealized experiment, the realistic velocity-dependent simulation uses $1.5 \cdot 10^{-3}$ for the drag coefficient and produces smaller melt rates than the corresponding velocity-independent simulation. Consequently, the maximum velocity-dependent integrated volume transport is reduced by 1/2 compared to the velocity-independent transport (note the use of different scales in figures 14a and 14b). The overall structure of the depth-integrated volume transport is similar in both cases. However, in the velocity-dependent experiment, no separation of the circulation in two distinct cyclonic gyres upstream and downstream of the sill occurs. This result is consistent with the difference in melting patterns between the two experiments. According to equation (17) the presence of an absolute maximum in melt rates downstream of the sill in the velocity-independent simulation induces a local cyclonic circulation there. This is not the case in the velocity-dependent simulation, since melt rates are not particularly high at this location. The distribution of hydrographic properties shown by temperature and salinity cross-sections (see figures 15 and 15) are consistent with the differences in circulation between the two experiments. In the velocity-independent case, the warmest and most salty water is isolated on the downstream side of the sill. This is not seen in the velocity-dependent experiment. This difference in the circulation and distribution of hydrographic properties between both simulations supports the idea that buoyancy flux-induced gradients of potential vorticity strongly control the cavity circulation at depth (Little et al., 2008).

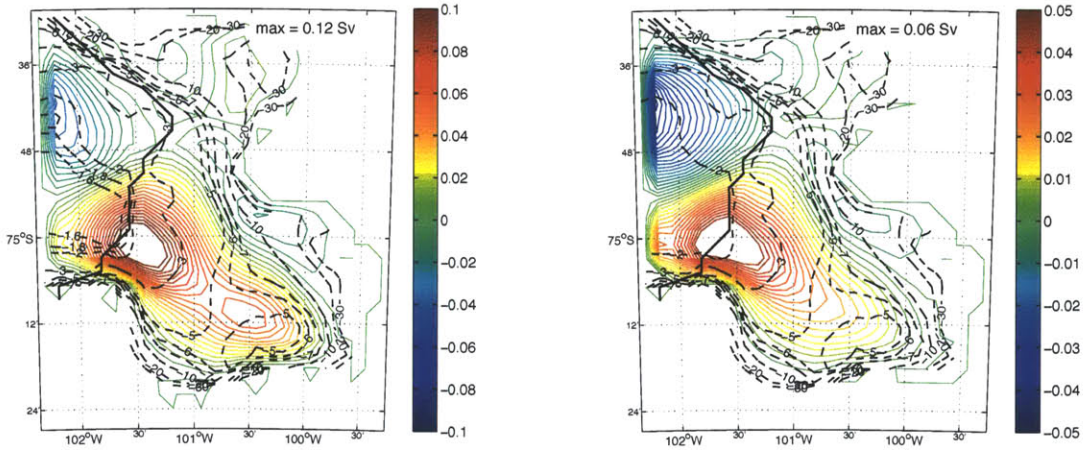

(a) velocity-independent $\gamma_{T,S}$ (b) velocity-dependent $\gamma_{T,S}$

Figure 14: Barotropic streamfunction for the depth-integrated horizontal volume transport (in Sv) calculated using (a) the velocity-independent and (b) the velocity-dependent parameterization of the turbulent exchange velocities. Dashed contours show the distribution of background potential vorticity, f/h (10^{-7} m^{-1}s^{-1}), with h the water column thickness. The thick black line indicates the position of the ice shelf front. Different scales are used to capture the details of the circulation in both cases.

Our simulated spatial pattern of velocity-dependent melt rates is in good agreement with the (velocity-dependent) plume model simulations of Payne et al. (2007), who obtain second melt rates maxima of about 25 m/yr over the path of two fast outflow plumes following inverted channels in the underside of the ice shelf base and a third but weaker plume outflow collecting meltwater under the norther potion of the ice shelf. Interestingly, their results are consistent with melt rates estimates from an ice flux divergence calculation based on ice velocity and thickness data. Payne et al. (2007) also point out that Advanced Spaceborne Thermal Emission and Reflection Radiometer (ASTER) images indicate a retreat of sea ice in front of the ice shelf over three isolated areas collocated with the outflows, suggesting the presence of warm upwelling plume water there.

In the simulations of Payne et al. (2007) however, the largest melting (over 100 m/yr) occurs over an area extending about 40 km away from the deepest part of the grounding line of PIIS proper. The present velocity-dependent simulation does not place an absolute melt rate maximum there, but the paths of the three outflow plumes are in good agreement with the experiments of Payne et al. (2007) and hence with the ASTER data. The differences between our results and those of Payne et al. (2007) are likely attributable to the very different modeling approaches. Payne et al. (2007) uses a reduced gravity (plume) model, which has the disadvantage of not assessing the impacts of any depth-independent flow within the cavity of PIIS. Hence the location of melting in their simulations is controlled only by hydrographic conditions, by the topography of the ice shelf base and by the velocity of meltwater plumes. Our three-dimensional model on the other hand suggests that depth-independent currents are important in controlling the distribution of melting underneath PIIS. Barotropic currents are consistent with the distribution of hydrographic properties and convergence of meltwater into the plume outflows and are particularly weak along the deepest grounding line of PIIS, inducing only slow melting there. Recently, Mueller et al. (2012) ran realistic simulations of Larsen C Ice Shelf using a three-dimensional model and the velocity-dependent melt rate parameterization of Holland and Jenkins (1999). In order to mimic the behavior of a plume model, they performed an experiment in which they prescribed a low initial value of friction velocity u_* at the base of the ice shelf and let u_* increase as the thermohaline circulation evolved. They indeed observed a migration of melt rates towards the high thermal forcing grounding lines in this particular simulation relative to their standard simulations. Furthermore, Payne et al. (2007) used a very different ice shelf bathymetry data sets for PIIS that includes many more small scale features of the ice shelf base than the present data set. For instance, the inverted channels key to the path of their outflow plumes are not represented in the present model. This could also explain some difference between their and our results. Nevertheless, the combination of their ice shelf base and bedrock bathymetry data results in a distribution of water column thickness comparable to that used in the present model at the location of plume outflows. Therefore, in both models, the outflows follow contours of f/h and hence are likely geostrophic[13].

[13]In a plume model such as that of Payne et al. (2007) only the geometry of the ice shelf base needs to be specified, not the bathymetry of the seafloor. It seems that the topography of the ice shelf base derived by Payne et al. (2007) compensates for the contribution of bedrock bathymetry in setting the overall water column thickness distribution, such that the pattern of f/h in their model is overall similar to ours.

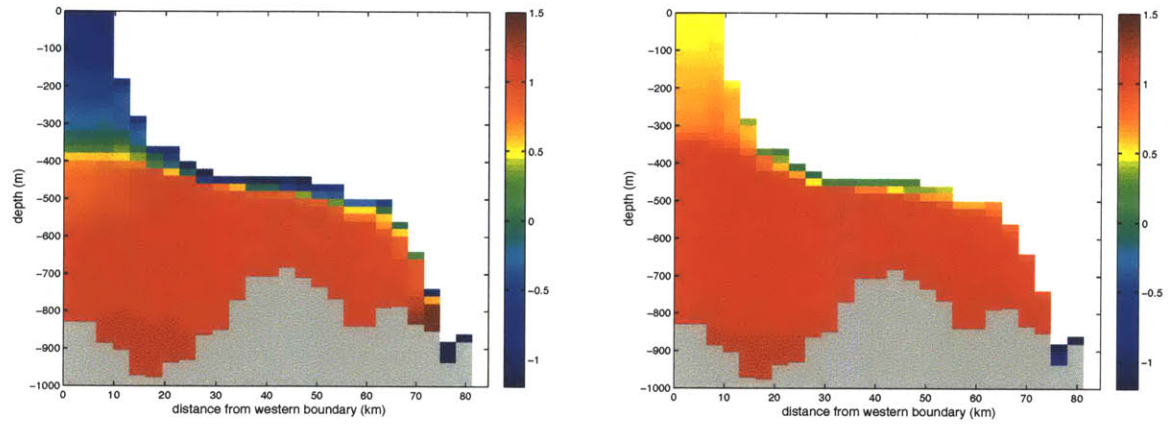

(a) T (°C), velocity-independent $\gamma_{T,S}$

(b) T (°C), velocity-dependent $\gamma_{T,S}$

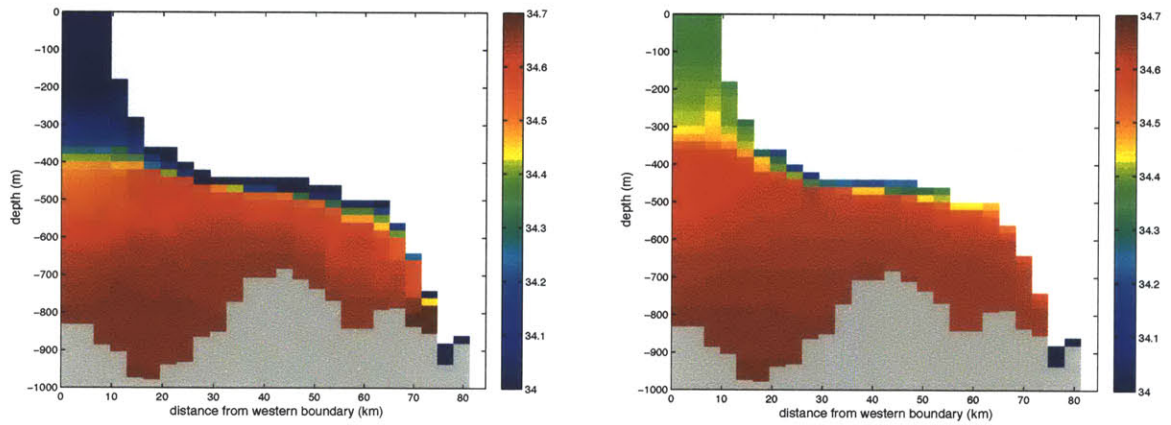

(c) S (psu) velocity-independent $\gamma_{T,S}$

(d) S (psu), velocity-dependent $\gamma_{T,S}$

Figure 15: Vertical cross-sections of potential temperature (upper panels) and salinity (lower panels) along the strait path shown in figure 5a, simulated using (a, c) the velocity-independent and (b, d) the velocity-dependent parameterization of the turbulent exchange velocities.

4.2 Dependence of the melt rate on the drag coefficient

As described in section 2, energy conservation at the ice-ocean interface requires that the latent heat flux associated with melting and refreezing be equal to the diffusive heat flux through the boundary layer, Q_M^T, minus the fraction of heat lost to the ice shelf by conduction, Q_I^T. In many studies (eg., Holland and Feltham, 2006; Holland and Jenkins, 1999; Determann and Gerdes, 1994) it was pointed out that scaling of (1) against typical ice shelf cavity conditions gives a magnitude of the conductive heat flux that is always about one order of magnitude smaller than the diffusive heat flux term. Hence, considering the ice shelf as a perfect insulator is a reasonable approximation. Doing so, one can equate the latent and diffusive heat fluxes at the ice shelf base and express the melt rate as

$$m = \frac{c_{pM}}{L_f} u_* \Gamma_T (T_M - T_B). \tag{32}$$

In this form, the heat conservation equation indicates that the two dominant external forcings on the melt rates are :

1. the friction velocity, u_*,
2. the temperature difference across the ice-ocean boundary layer, $T_M - T_B$, also referred to as the 'thermal forcing' (Holland and Jenkins, 1999).

Because of the dominance of molecular over turbulent diffusion in the viscous sublayer closest to the ice interface, the heat and salt exchange coefficients $\Gamma_{T,S}$ are very weakly dependent on the friction velocity. Hence equation (32) predicts to first order a linear dependence of the melt rate on u_*. From the equation for u_* (8), one therefore expects the melt rate to be nearly-linearly dependent on $\sqrt{C_d}$.

Many second order effects and feedbacks are however likely to alter this first order approximation. First, increasing the drag coefficient enhances friction at the ice shelf base. It is therefore expected to slow down the flow of the buoyant plume along the ice shelf base, hence to reduce the mixed layer velocity U_M. As the melt rate is made (nearly) linearly proportional to U_M through the parameterization of u_*, this counteracting effect should result in a sub-linear dependence of the melt rate on $\sqrt{C_d}$. It might also cause the melt rate to decrease with increasing drag coefficient beyond some critical value of C_d. On the other hand, the increase of the melt rate with C_d will directly intensify buoyancy fluxes underneath the ice shelf and with it, the melt-induced density gradients. As discussed by Little et al. (2008), mixed layer currents should increase in response to the strengthening of density gradients underneath the ice shelf. This will initiate a positive feedback on the melting that could lead to an over-linear dependence of melt rates on u_*. Varying the drag coefficient also directly impacts the diffusivity of salt across the boundary layer trough the formulation of the salt exchange velocity. As γ_S is nearly linearly dependent on $\sqrt{C_d}$ (equation 10), increasing the drag coefficient should accelerate the relaxation of salinity at the ice shelf base towards the mixed layer value and thereby reduce the salinity difference $S_M - S_B$ across the ice-ocean boundary layer. Through the dependence of freezing point on salinity, this should reduce the difference in temperature across the boundary layer, hence the melt rates. In theory, this should promote a sub-linear dependence of the melt rates on C_d. However, because the dependence of seawater temperature on salinity is only weak, this effect is expected to be small. Feedbacks on the melt rates through changes in the cavity circulation induced when varying C_d can also be expected.

To investigate the dependence of the melt rates of C_d and assess the relative importance of various feedbacks associated with variations of the drag coefficient, we compare sets of both idealized and realistic PIIS experiments in which C_d is varied between $\frac{1}{16}$ and 16 times the 'default' value suggested by Holland and Jenkins (1999) ($1.5 \cdot 10^{-3}$). We examine the behavior of the two direct forcings on the melt rates under changes of drag coefficients by comparing area-averaged values of the friction velocity and difference in temperature across the

boundary layer underneath the ice shelf. The area average value of a given variable X is calculated as

$$\frac{1}{A}\int_x\int_y \dot{X}\ dx\ dy$$

where A is the total area of the ice shelf base and $dxdy$ is the area of each individual cell. To account for the slope of the ice shelf base, the area of each grid cell should be calculated as

$$dx \cdot \cos(\alpha) dy.$$

with α, the slope of the ice shelf base, given by the zonal gradient of water column thickness across each grid cell:

$$\alpha = \arctan \frac{dh}{dx},$$

However, in the $\frac{1}{8}^\circ$ resolution model, the gradient of water column thickness can be at most $\frac{1000\ \mathrm{m}}{4000\ \mathrm{m}}$. For this ratio, the correction factor on the grid cell area is of 3%. Hence the ice shelf base slope is neglected and the ice shelf base slope area calculated from the horizontal area of each grid cell. This approach is convenient to calculate spatial averages, particularly in the case of the realistic PIIS cavity experiments. Over the range of drag coefficients investigated here, the heat flux trough the ice shelf Q_I^T varies between 0.1% and 1% of Q_M^T. Hence it is not expected to make a significant contribution to the variability of the melt rate with C_d.

4.2.1 Idealized experiments

Figure 16a shows the area-averaged melt rate and diffusive heat flux calculated for simulations with varying drag coefficient. As predicted by theory, both quantities increase with the drag coefficient in a sub-linear manner. As seen in figure 16b, friction velocity also increases with the drag coefficient. From theory, one would expect a linear relationship between u_* and $\sqrt{C_d}$ (equation 8) such that a power-law fit of the form $u_* = aC_d^b$ would have $b = 0.5$. Fitting the area-averaged friction velocity against the drag coefficient with such a power law (blue curve) actually indicates that the dependence of u_* on $\sqrt{C_d}$ is above-linear (within a 95% interval, $b = [0.675, 0.7534]$). This is because the area-averaged mixed layer velocity (figure 16b, dashed/dotted orange curve) also increases with the drag coefficient, in a sub-linear manner. As mentioned earlier, the increase of mixed layer currents is consistent with a strengthening of buoyancy-flux induced density gradients under the shelf (Little et al., 2008). In turn, stronger mixed layer currents increase the diffusive heat flux across the boundary layer, thereby accelerating the increase of melt rates with C_d. This positive feedback between melt rates, buoyancy fluxes-induced gradients and mixed layer currents is therefore expected to result in an above-linear dependence of the melt rate on $\sqrt{C_d}$. Such a feedback will not be accounted for by a velocity-independent parameterization of the turbulent exchange velocities.

On the other hand, figure 16c shows that the thermal forcing (plain purple curve) underneath the ice shelf decreases with the drag coefficient in a sub-linear manner. Since the ice shelf base temperature varies only with pressure and only weakly with salinity, this points to an overall cooling of the mixed layer and is consistent with the production of a larger volume of cold buoyant meltwater that spreads and forms an insulating film at the ice shelf base (Jacobs et al., 2011). The reduction in thermal forcing is therefore a negative feedback on the increase of melting with C_d. Provided that the cooling is due to a larger production of meltwater, S_B will decrease as the drag coefficient is increased. This will raise the freezing point and reduce the difference of temperature across the boundary layer, thereby further slowing the increase in melt rates with C_d. The increase in salt diffusivity (i.e., γ_S) with C_d is also expected to reduce the salinity gradient at the ice shelf base

and reduce the melt rates. To verify if either or both of these salt feedbacks have a non-negligible effect on the variability of thermal forcing with changing C_d, we calculate the area-averaged thermal driving underneath the ice shelf (red curve), defined as

$$T_* = T_M - T_B - a(S_M - S_B) \tag{33}$$

with a, the (negative) salinity coefficient given in section 2. Thermal driving is equivalent to thermal forcing in a two-equation model, i.e., it is the thermal driving one obtains when neglecting the effects of salt diffusivity on the temperature gradient at the ice shelf base (Holland and Jenkins, 1999). Fitting the area-averaged values of both quantities shows that the thermal forcing and thermal driving behave very similarly with C_d in the model. This suggests that salinity feedbacks on the thermal forcings are not significant, as anticipated.

Fitting the area-averaged melt rate against C_d with a power law of the form $m = aC_d^b$ gives $b \gtrless 0.5$ over

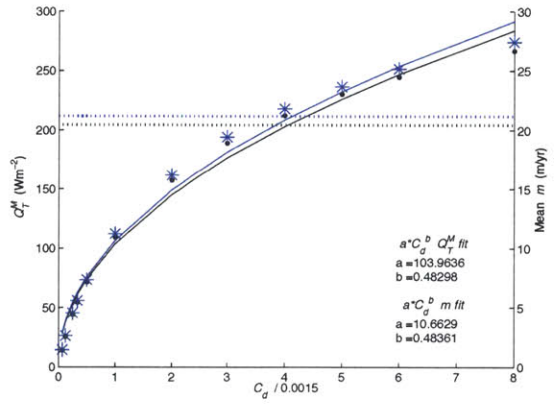

(a) m and Q_T^M

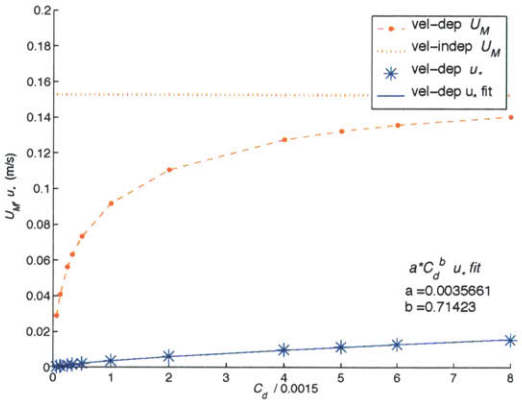

(b) u_* and U_M

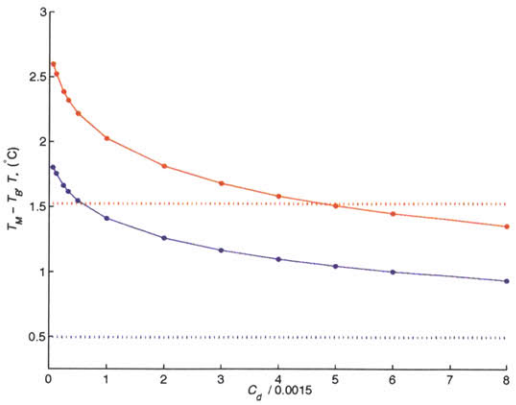

(c) thermal driving and thermal forcing

Figure 16: (a) Area averaged diffusive heat flux Q_M^T (W/m^2, black dots) and melt rate (m/yr, blue asterisks) underneath the idealized ice shelf as a function of the drag coefficient C_d. The black and blue dotted lines show respectively the area-averaged Q_M^T and melt rate obtained using the velocity-independent parameterization of $\gamma_{T,S}$. The solid black and blue curves are power law fits to the area-averaged diffusive heat flux and melt rates. Coefficients of the fits are shown in the lower right corner of the graph. The correspondence between the fits indicates that both quantities vary very similarly under changes in C_d and hence suggests that the variability of Q_I^T to C_d is negligible. (b) Area averaged mixed layer velocity (ms^{-1}, orange dotted/dashed curve) and friction velocity (ms^{-1}, blue asterisks), as a function of the drag coefficient C_d. The orange dotted line shows the area-averaged mixed layer velocity U_M calculated for the velocity-independent experiment. The solid blue curve is the power law fit to the area-averaged friction velocity. (c) Area averaged thermal driving (°C, red curve) and thermal forcing (°C, purple curve) across the boundary layer as a function of the drag coefficient C_d. The red and purple dotted lines show the area-averaged thermal driving and thermal forcing respectively, calculated in the velocity-independent experiment.

a 95% confidence interval. Hence it does not allow determining which of the positive mixed layer velocity feedback ($b > 0.5$) or the negative thermal forcing feedback ($b < 0.5$) on melt rates is dominant. Consideration of the scattering of the calculated melt rate around the fitted curve in figure 16a indicates that a power law of this form might not be appropriate, as the misfit is not random but systematic over different ranges of drag coefficient. This suggests the occurrence of feedbacks and/or non-linearities in the model that are not accounted for in the theory described above.

Nonetheless, the dependence of the melt rate on C_d observed here is in good agreement with the results of Payne et al. (2007), who obtained a sub-linear dependence of the ablation rates on the drag coefficient with the velocity-dependent plume model of Holland and Feltham (2006). One important difference between their results and ours is that they found melt rates decreased beyond a critical value of C_d due to the reduction of plume velocity with increased frictional drag at the ice shelf base. Here, melt rates increase over the whole range of drag coefficient values even if this range is wider than that used by Payne et al. (2007). This might be attributable to the difference in the modeling approach used here and that employed in the work of Payne et al. (2007) and could be an indication of the importance of horizontal circulation in setting the melt rate distribution.

Figure 16b also indicates that the velocity-independent parameterization of Hellmer and Olbers (1989) produces higher mixed layer velocities than the velocity-dependent parameterization of Holland and Jenkins (1999) over the whole range of drag coefficients investigated here. This is due to the increase of friction at the ice shelf base which slows down mixed layer currents. Another set of experiments in which the drag coefficient at the ice shelf base was kept constant in the momentum equation but was varied in the heat (and salt) conservation equation (results not shown) actually showed that the area-averaged mixed layer velocity in the velocity-dependent model matched that in the velocity-independent model for $C_d \approx 4 \times 1.5 \cdot 10^{-3}$. Thermal forcing on the other hand is higher in the velocity-dependent simulations for all values of C_d. It is also interesting to note that thermal driving is higher than thermal forcing by more than half a degree for all drag coefficients. This indicates that neglecting the effects of salt diffusivity would significantly overestimate the melt rates. Figure 16a suggests that a drag coefficient four times the default value gives the best agreement in melt rates between the velocity-independent and velocity-dependent experiments.

However, matching the velocity-dependent results to that of the velocity-independent experiments does not physically justify the use of this increased valued of C_d. Comparison of both the velocity-dependent and independent results against observations under PIIS is the only valuable validation of the drag coefficient in the absence of direct measurements of C_d, and it is not done here. Furthermore, as mentioned in the previous section, the constant heat transfer velocity adopted by Hellmer and Olbers (1989) implies a uniform mixed layer velocity that is overestimating the actual conditions under PIIS. Hence, decreasing the value of γ_T in the velocity-independent experiments would perhaps be a more appropriate approach than increasing C_d to match the velocity-dependent and velocity-independent melt rates. Therefore, in the absence of physical evidence for the use of another value of C_d, we keep $1.5 \cdot 10^{-3}$ in the following as our 'default' value of drag coefficient. Nevertheless, since the distribution of melt rates and the structure of the cavity circulation are not altered by the specific value of the drag coefficient in our experiments (as discussed below), we will sometimes adopt the value $6.0 \cdot 10^{-3}$ for the drag coefficient in the idealized simulations in order to allow some comparison of the variability of the velocity-dependent and velocity-independent melt rate parameterizations under different forcings. Unless stated otherwise, the drag coefficient is kept to the default value in all other cases.

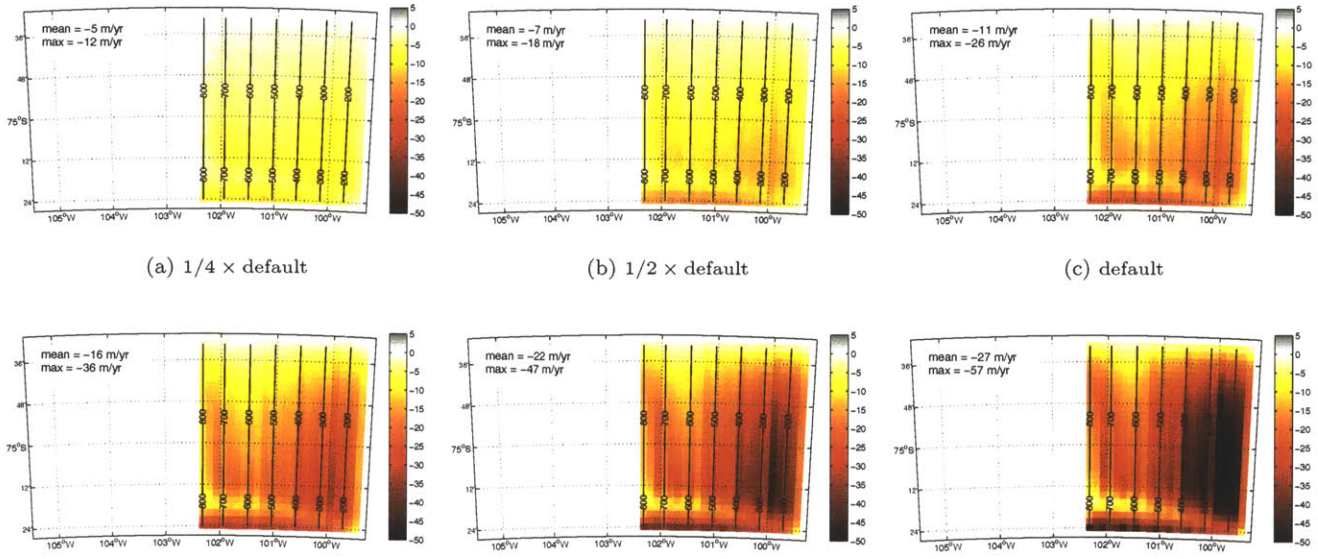

(a) 1/4 × default (b) 1/2 × default (c) default

(d) 2 × default (e) 4 × default (f) 8 × default

Figure 17: Velocity-dependent melt rate underneath the ice shelf (m/yr) calculated for the idealized experiments using (a) $\frac{1}{4}$ × default C_d, (b) $\frac{1}{2}$ × default C_d, (c) default C_d, (d) 2 × default C_d, (e) 4 × default C_d, (f) 8 × default C_d. The maximum and area-averaged melt rates are indicated in the top left corner of each figure.

Increasing the drag coefficient in the velocity-dependent experiments does not alter the spatial distribution of the melt rates. Figure 17 shows the melt rate distribution obtained with a drag coefficient 1/4, 1/2, 1, 2, 4 and 8 times the default value of $1.5 \cdot 10^{-3}$. In all cases, the pattern described in the previous section for the velocity-dependent $\gamma_{T,S}$ simulation is recognizable: the maximum melting occur along the southern portion of the grounding line and decreases westward towards the ice front. A second maximum is collocated with the outflow of the meltwater plume along the southern boundary. As the drag coefficient is increased, both the melting and mixed layer currents increase over these regions, as expected from the strengthening of buoyancy-induced zonal density gradients (see figure 18). Melt rates therefore remain strongly spatially correlated to the mixed layer velocity when varying the drag coefficient. On the other hand, the temperature difference across the boundary layer diminishes over the region of fastest melt when C_d is increased (see figure 19). For an increase of C_d up to 16-folds, T_M and S_M locally decrease beyond the lowest surface temperature and salinity prescribed as initial and boundary conditions, by more than half a degree and 0.7 psu respectively. This confirms that the cooling of the mixed layer is due to increased production or melt water rather than redistribution of hydrographic properties in the cavity. Consistently with this picture, zonal cross-sections of temperature and salinity across the westward outflow (along the 75.375°S parallel, see figures 22 and 23) indicate a cooling, freshening and thickening of the plume as the drag coefficient is increased. Both the depth integrated volume transport and meridionally-integrated overturning circulation also strengthen with the drag coefficient (see figures 20 and 21). The increase in the barotropic circulation is consistent with the accelerated melting and enhanced buoyancy-induced density gradients (Little et al., 2008). The strengthening of the overturning circulation agrees with the production of larger volumes of melt water and resulting increase of vertical density gradients, which enhances the buoyancy of the plume (Holland et al., 2008). Finally, as the melt rate pattern is preserved under variations of drag coefficients, the spatial structure of the circulation is too.

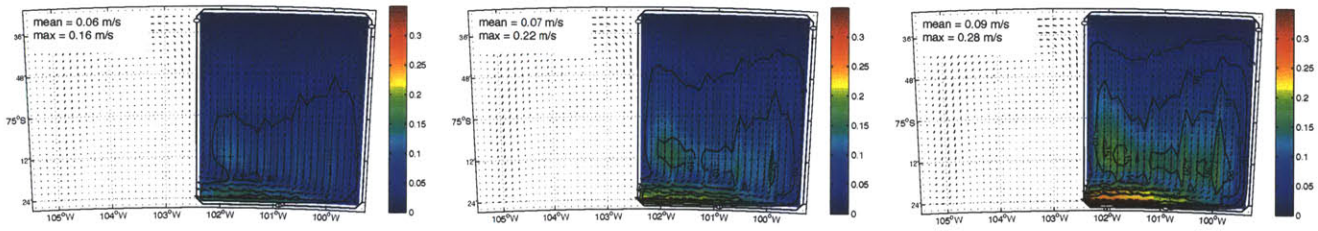

(a) 1/4 × default (b) 1/2 × default (c) default

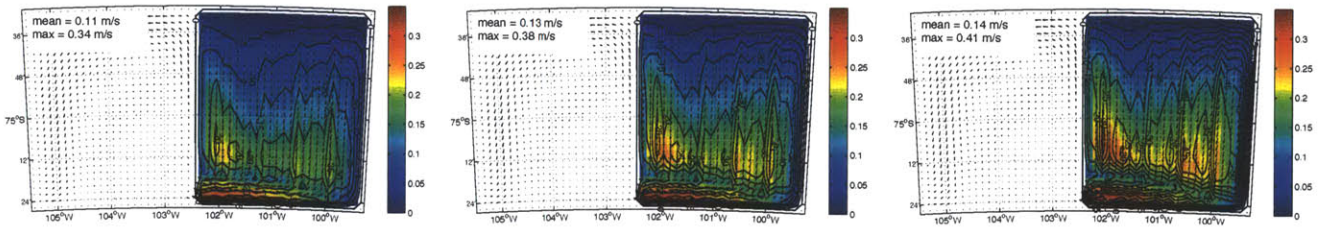

(d) 2 × default (e) 4 × default (f) 8 × default

Figure 18: Mixed layer velocity (ms^{-1}) simulated with the velocity-dependent idealized model using (a) $\frac{1}{4}$ × default C_d, (b) $\frac{1}{2}$ × default C_d, (c) default C_d, (d) 2 × default C_d, (e) 4 × default C_d, (f) 8 × default C_d. Vectors indicate the direction and relative magnitude of the mixed layer currents. The maximum and area-averaged mixed layer velocities are indicated on each figure. Black contours show the distribution of melt rates (m/yr).

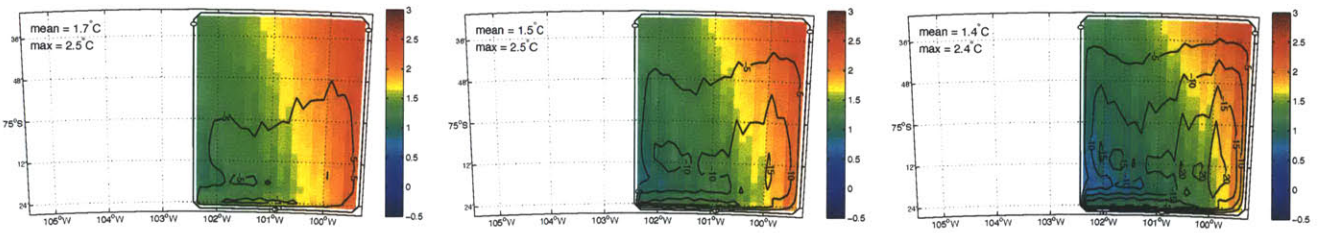

(a) 1/4 × default (b) 1/2 × default (c) default

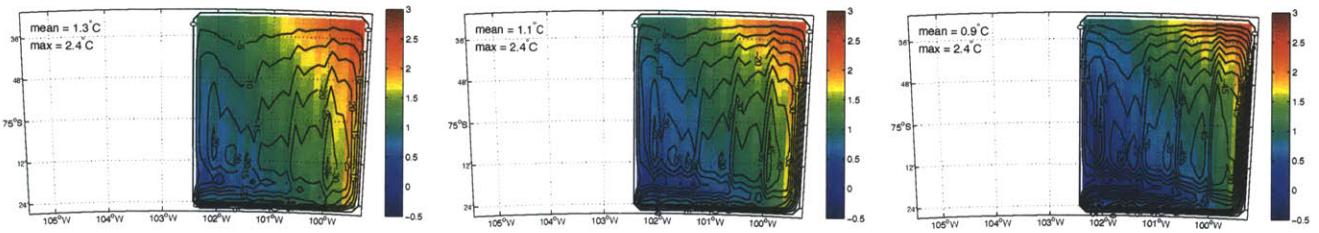

(d) 2 × default (e) 4 × default (f) 8 × default

Figure 19: Thermal forcing underneath the ice shelf ($T_M - T_B$,°C) simulated with the velocity-dependent idealized model using (a) $\frac{1}{4}$ × default C_d, (b) $\frac{1}{2}$ × default C_d, (c) default C_d, (d) 2 × default C_d, (e) 4 × default C_d, (f) 8 × default C_d. The maximum and area-averaged thermal forcings are indicated on each figure. Black contours show the distribution of melt rates (m/yr).

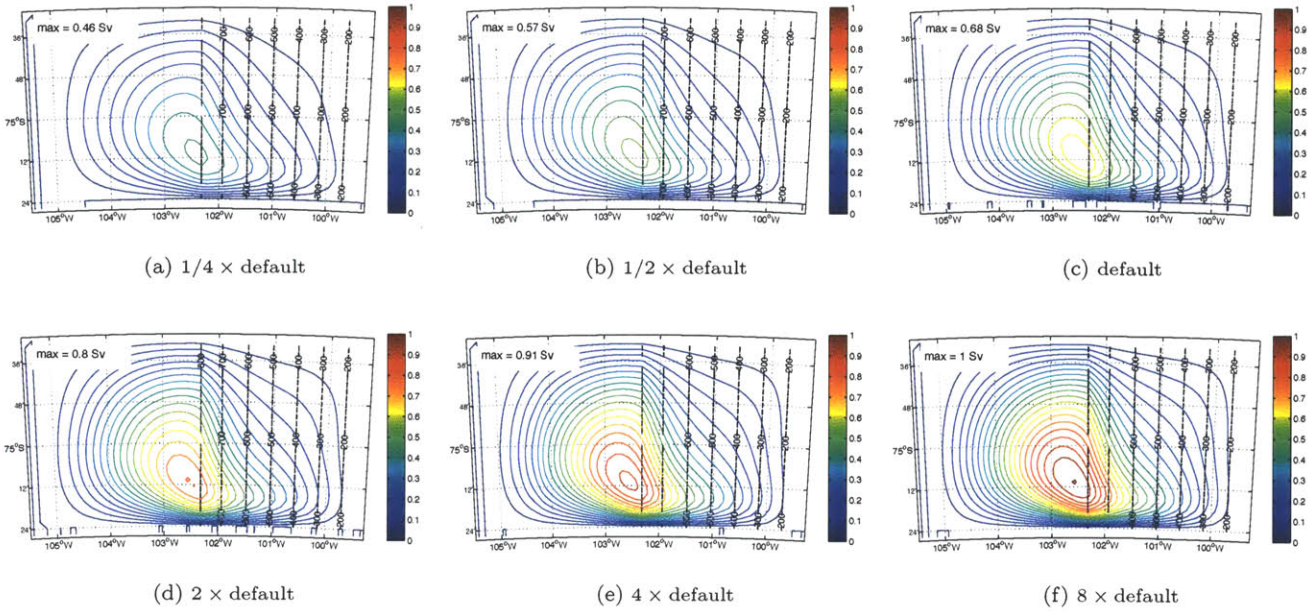

(a) 1/4 × default (b) 1/2 × default (c) default

(d) 2 × default (e) 4 × default (f) 8 × default

Figure 20: Barotropic streamfunction of the vertically integrated volume transport (Sv) for idealized velocity-dependent simulations using (a) $\frac{1}{4}$ × default C_d, (b) $\frac{1}{2}$ × default C_d, (c) default C_d, (d) 2 × default C_d, (e) 4 × default C_d, (f) 8 × default C_d. Dashed contours show the distribution of water column thickness (m) underneath the ice shelf. The maximum value of barotropic transport is indicated in the top left corner of each figure.

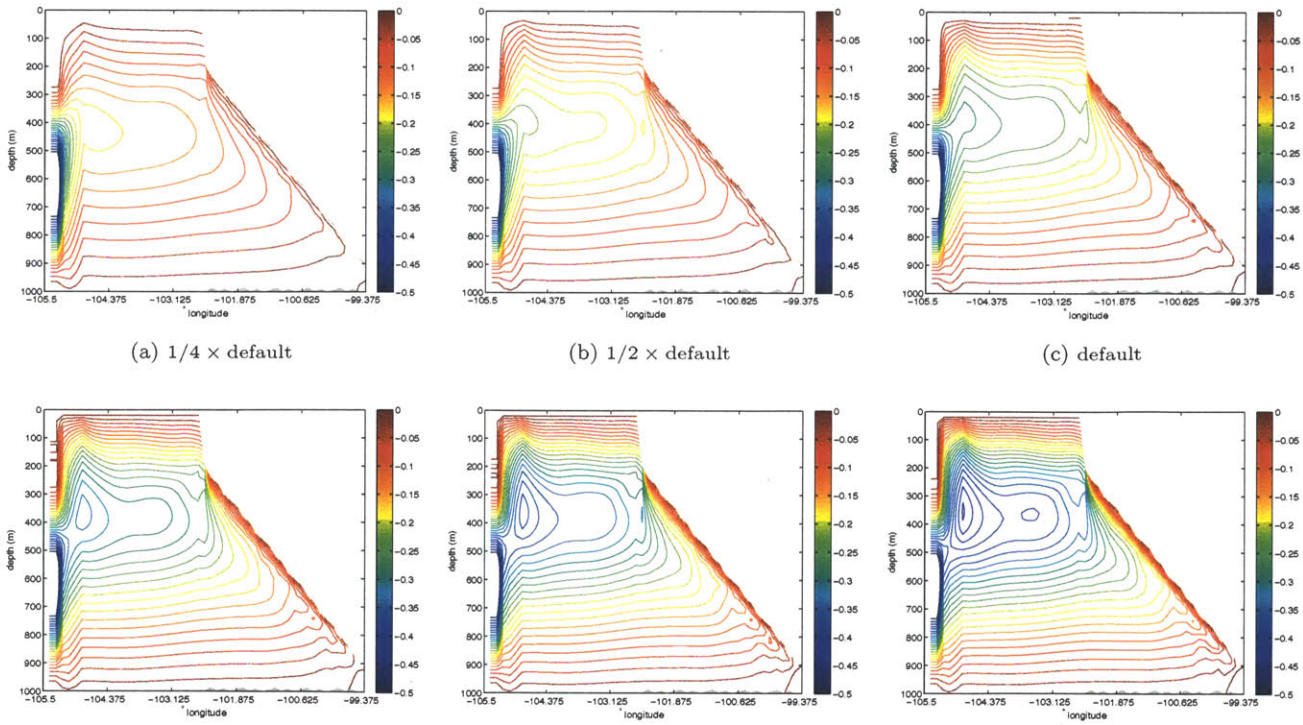

(a) 1/4 × default (b) 1/2 × default (c) default

(d) 2 × default (e) 4 × default (f) 8 × default

Figure 21: Overturning streamfunction of the meridionally integrated volume transport (Sv) for idealized velocity-dependent simulations using (a) $\frac{1}{4}$ × default C_d, (b) $\frac{1}{2}$ × default C_d, (c) default C_d, (d) 2 × default C_d, (e) 4 × default C_d, (f) 8 × default C_d.

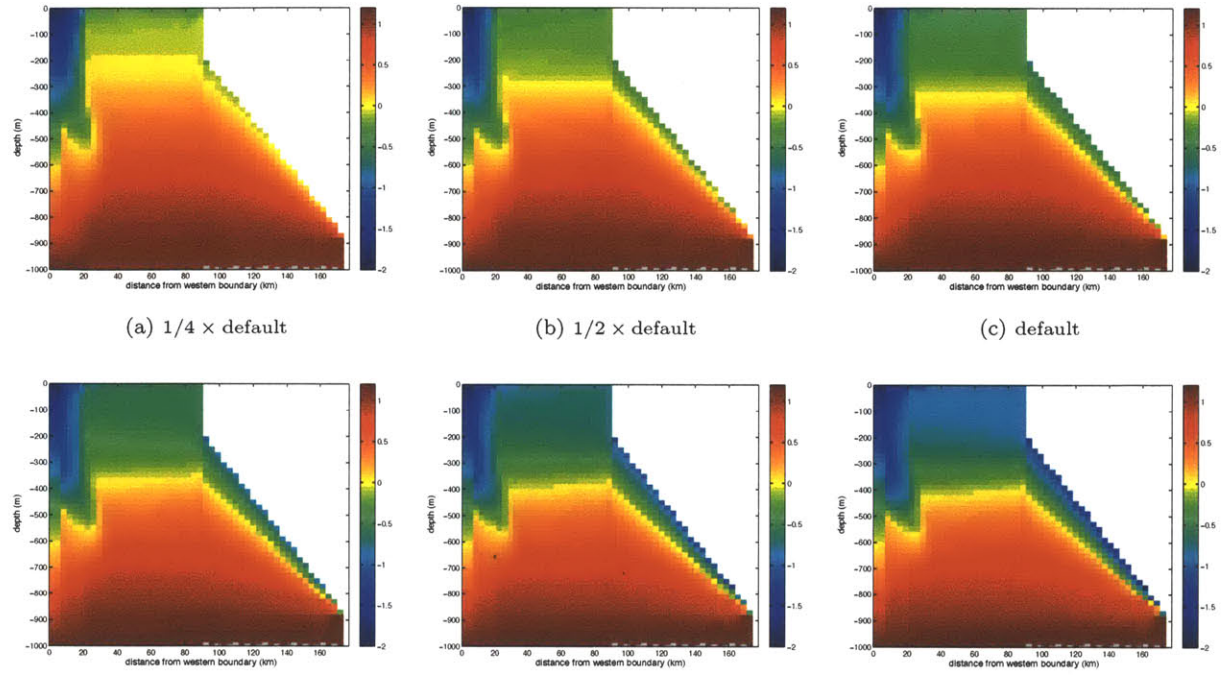

(a) 1/4 × default (b) 1/2 × default (c) default

(d) 2 × default (e) 4 × default (f) 8 × default

Figure 22: Vertical cross-sections of potential temperature (°C) along 75.375°S for the idealized velocity-dependent simulations using (a) $\frac{1}{4}$ × default C_d, (b) $\frac{1}{2}$ × default C_d, (c) default C_d, (d) 2 × default C_d, (e) 4 × default C_d, (f) 8 × default C_d.

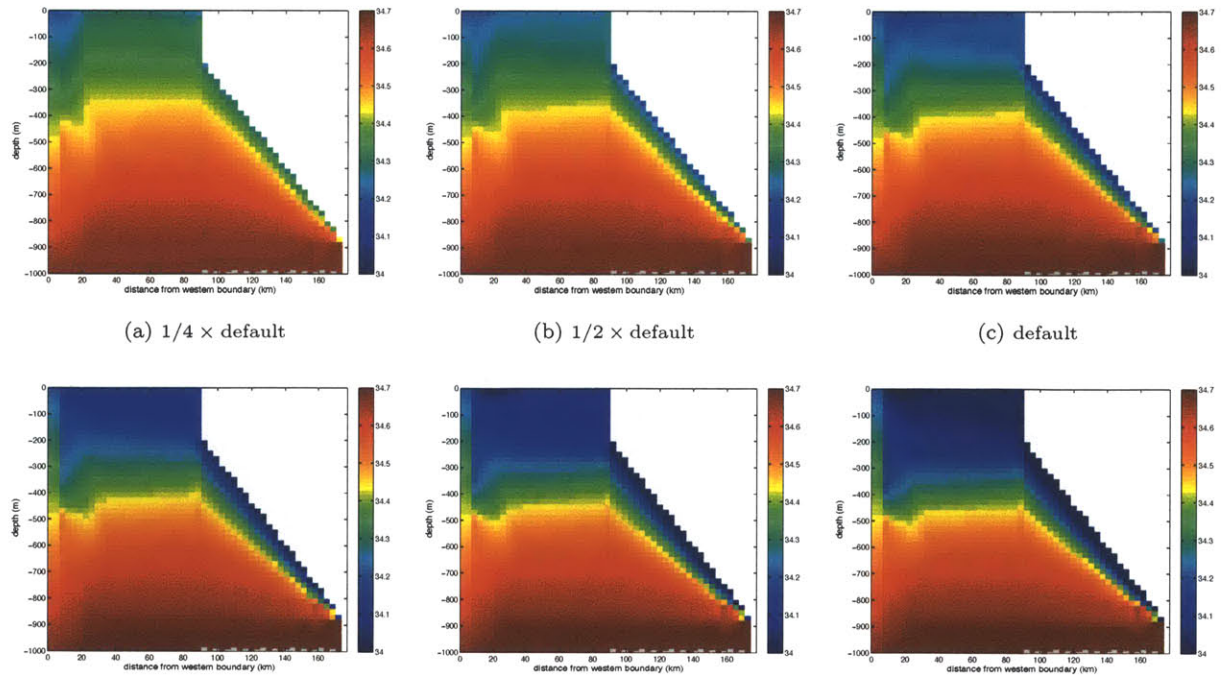

(a) 1/4 × default (b) 1/2 × default (c) default

(d) 2 × default (e) 4 × default (f) 8 × default

Figure 23: Vertical cross-sections of salinity (psu) along 75.375°S for the idealized velocity-dependent simulations using (a) $\frac{1}{4}$ × default C_d, (b) $\frac{1}{2}$ × default C_d, (c) default C_d, (d) 2 × default C_d, (e) 4 × default C_d, (f) 8 × default C_d.

4.2.2 Realistic experiments

Thermodynamic forcings and melt rates in the realistic experiments behave in a similar manner as in the idealized experiments when varying the drag coefficient. As shown in figure 24a, the melt rate varies as a sub-linear function of C_d. The mixed layer velocity also increases in a sub-linear fashion with C_d, resulting in an above-linear increase in friction velocity with $\sqrt{C_d}$ (see figure 24b). This suggests that a positive feedback between enhanced melting, strengthened buoyancy-induced density gradients and mixed layer currents similar to that observed in the idealized experiments accelerates the increase in melt rates with C_d underneath PIIS. Thermal forcing decreases in a sub-linear manner with $\sqrt{C_d}$, in agreement with the idealized cases (see figure 24c, purple curve), and indicates an increased production of meltwater that insulates the ice interface from the warmer waters below. As in the idealized experiments, almost identical power fits for the evolution of thermal forcing and thermal driving against C_d suggest that the mixed layer and the accelerated diffusivity of salt accompanying the increase in C_d do not feedback significantly on the thermal forcing (see figure 24c).

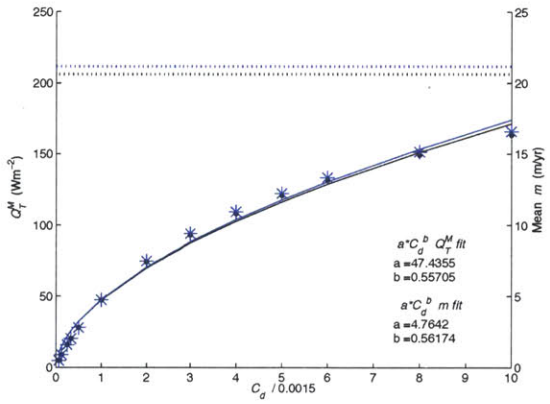

(a) m and Q_T^M

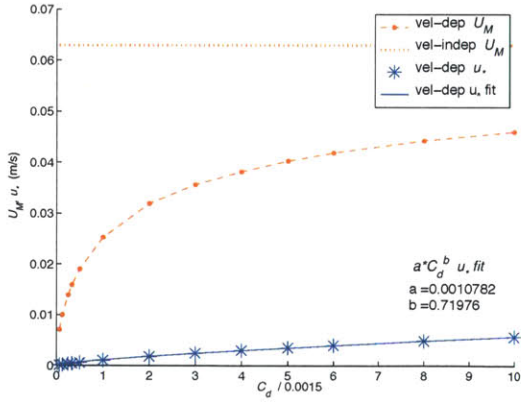

(b) U_M

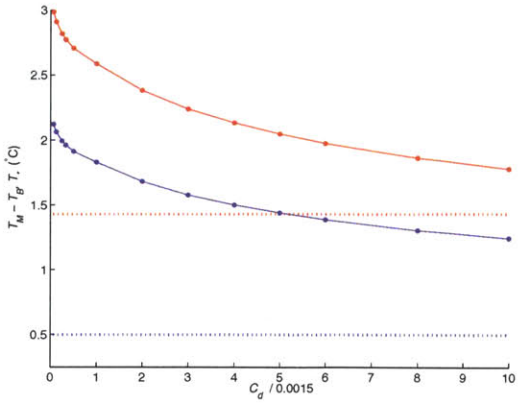

(c) thermal driving and thermal forcing

Figure 24: (a) Area averaged diffusive heat flux (W/m^2, black dots) and melt rate (m/yr, blue asterisks) underneath the idealized ice shelf as a function of the drag coefficient. The solid black and blue curves are power law fits to both variables. The black and blue dotted lines show respectively the area-averaged Q_M^T and melt rate obtained using the velocity-independent parameterization of $\gamma_{T,S}$. (b) Area averaged mixed layer velocity (ms^{-1}, orange dotted/dashed curve) and friction velocity (ms^{-1}, blue asterisks), as a function of the drag coefficient C_d. The orange dotted line shows the area-averaged mixed layer velocity U_M calculated for the velocity-independent experiment. The solid blue curve is the power law fit to the area-averaged friction velocity. (c) Area averaged thermal driving (°C, red curve) and thermal forcing (°C, purple curve) across the boundary layer, as a function of the drag coefficient C_d. The red and purple dotted lines show the same area-averaged forcings calculated in the velocity-independent experiment.

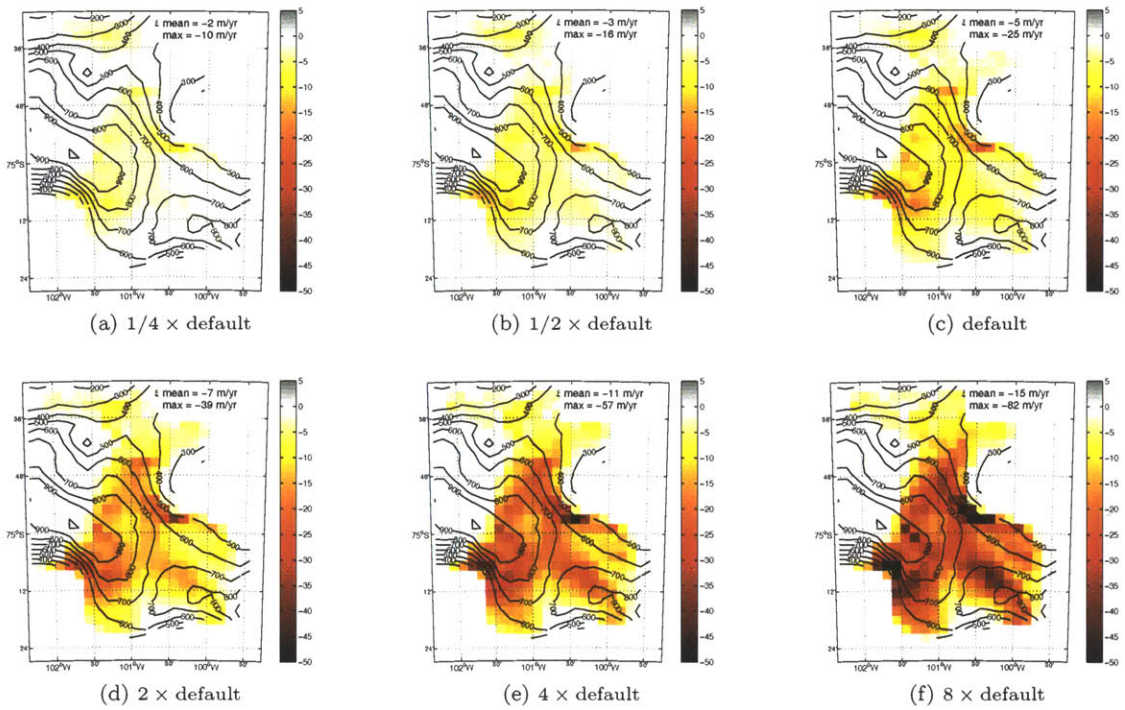

(a) 1/4 × default (b) 1/2 × default (c) default

(d) 2 × default (e) 4 × default (f) 8 × default

Figure 25: Melt rate underneath the ice shelf (m/yr) simulated with the velocity-dependent realistic PIIS model using (a) $\frac{1}{4}$ × default C_d, (b) $\frac{1}{2}$ × default C_d, (c) default C_d, (d) 2 × default C_d, (e) 4 × default C_d, (f) 8 × default C_d. The maximum and area-averaged melt rates for each simulation are given at the top right corner of the figures. Black contours show the depth of the seabed (m).

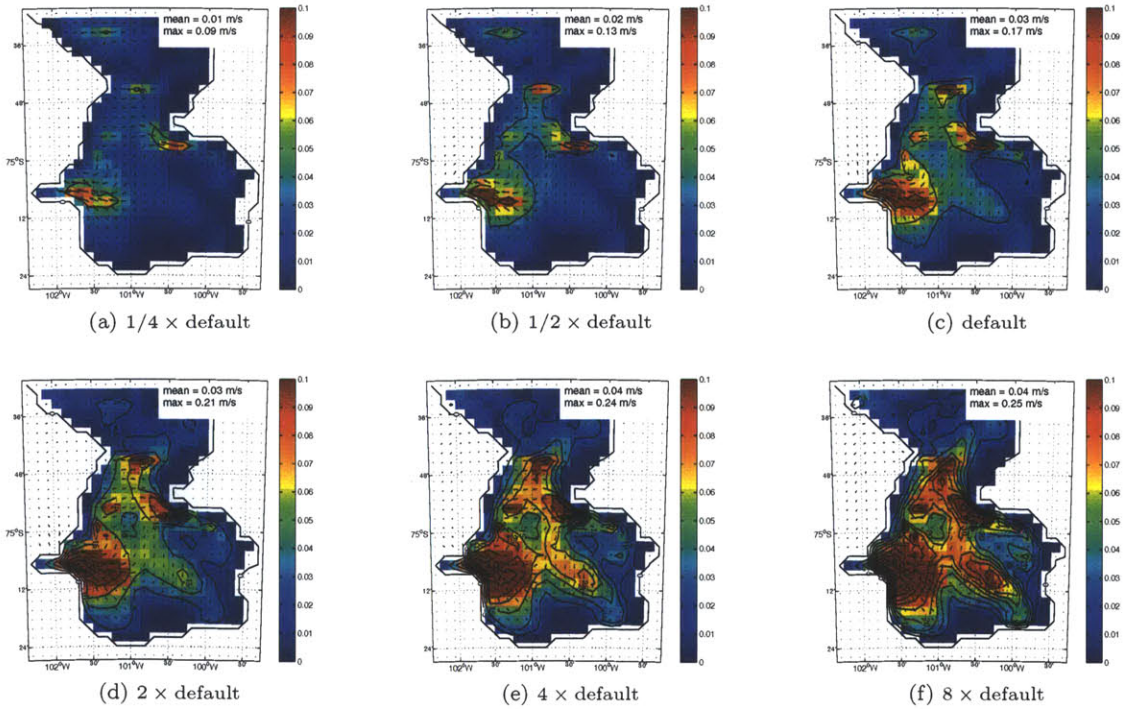

(a) 1/4 × default (b) 1/2 × default (c) default

(d) 2 × default (e) 4 × default (f) 8 × default

Figure 26: Mixed layer velocity (ms^{-1}) simulated with the velocity-dependent realistic PIIS model using (a) $\frac{1}{4}$ × default C_d, (b) $\frac{1}{2}$ × default C_d, (c) default C_d, (d) 2 × default C_d, (e) 4 × default C_d, (f) 8 × default C_d. Vectors indicate the direction and relative magnitude of the mixed layer currents. Black contours show the distribution of melting (m/yr)

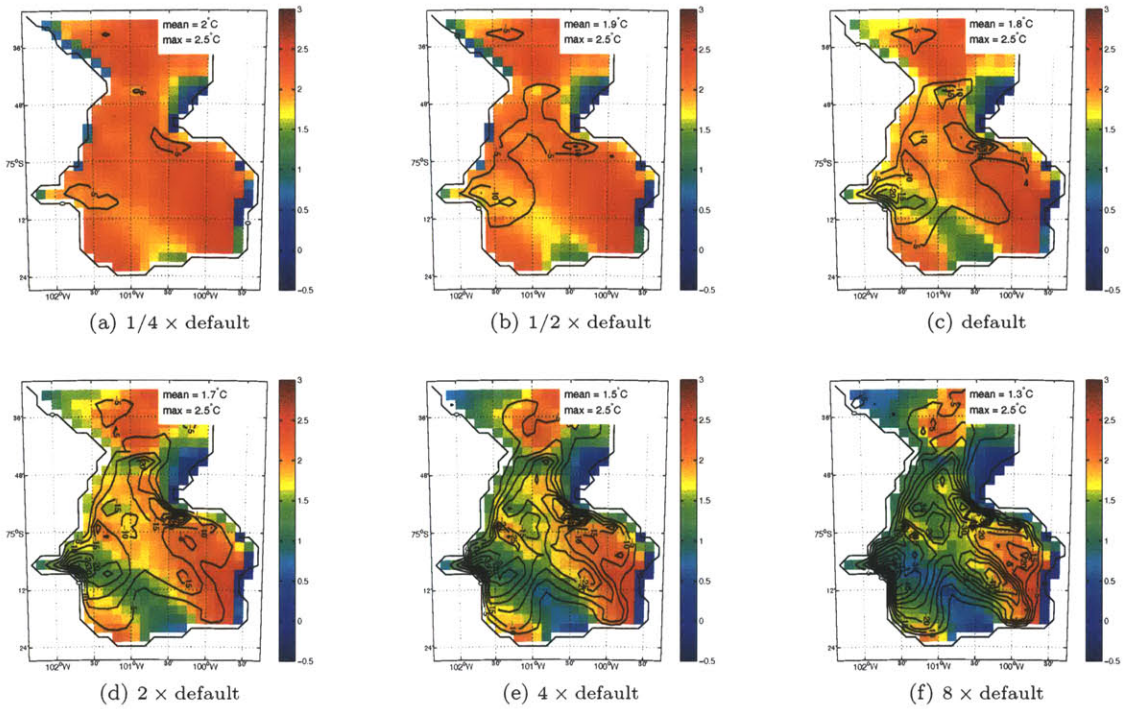

(a) 1/4 × default (b) 1/2 × default (c) default

(d) 2 × default (e) 4 × default (f) 8 × default

Figure 27: Thermal forcing underneath the ice shelf ($T_M - T_B$,°C) simulated with the velocity-dependent realistic PIIS model using (a) $\frac{1}{4}$ × default C_d, (b) $\frac{1}{2}$ × default C_d, (c) default C_d, (d) 2 × default C_d, (e) 4 × default C_d, (f) 8 × default C_d. The maximum and area-averaged thermal forcings are indicated on each figure. Black contours show the distribution of melt rates (m/yr).

As in the idealized experiments, the velocity-independent formulation produces higher melt rates than the velocity-dependent formulation of $\gamma_{T,S}$. The area-averaged mixed layer velocity is lower in the velocity-dependent than in the velocity-independent experiment over the entire range of values of drag coefficient investigated (including 16 × default C_d, not shown). This was also the case in the idealized experiments. However, in the realistic simulations, the slower mixed layer velocities cannot be entirely explained by the increased friction at the ice shelf base. Even when keeping the drag coefficient constant in the momentum equation and varying C_d only in the heat and salt conservation equations, currents underneath the ice shelf remain slower than in the velocity-independent model. On the other hand, figure 24c shows that the thermal forcing is higher in the velocity-dependent than in the velocity-independent experiments for all values of C_d.

Varying the drag coefficient in the realistic PIIS simulations changes the magnitude of the rates of melting, thermal forcing and mixed layer velocities, but conserves the spatial pattern of melt rates. It therefore remains strongly spatially correlated to U_M and seemingly not affected by the distribution of thermal forcing. As the drag coefficient is decreased, some refreezing occurs. It is however slow and restricted to small portions of the grounding line, such that it accounts for a total (area-integrated) accumulation rate between about 0.1 and 0.65 meters per year.

As in the idealized simulations, the depth-integrated volume transport increases with C_d in response to the acceleration in melting and the strengthening in horizontal density gradients. The structure of the barotropic circulation remains overall unaltered by the choice of C_d (see figure 28). Vertical cross-sections of temperature and salinity across the deep southeastern corner of PIIS indicate a cooling and freshening of the uppermost ocean layers underneath the shelf when C_d is increased, in agreement with the calculated decrease in area-averaged thermal forcing (see figures 29 and 30). This is expected from the strengthening of the vertical density

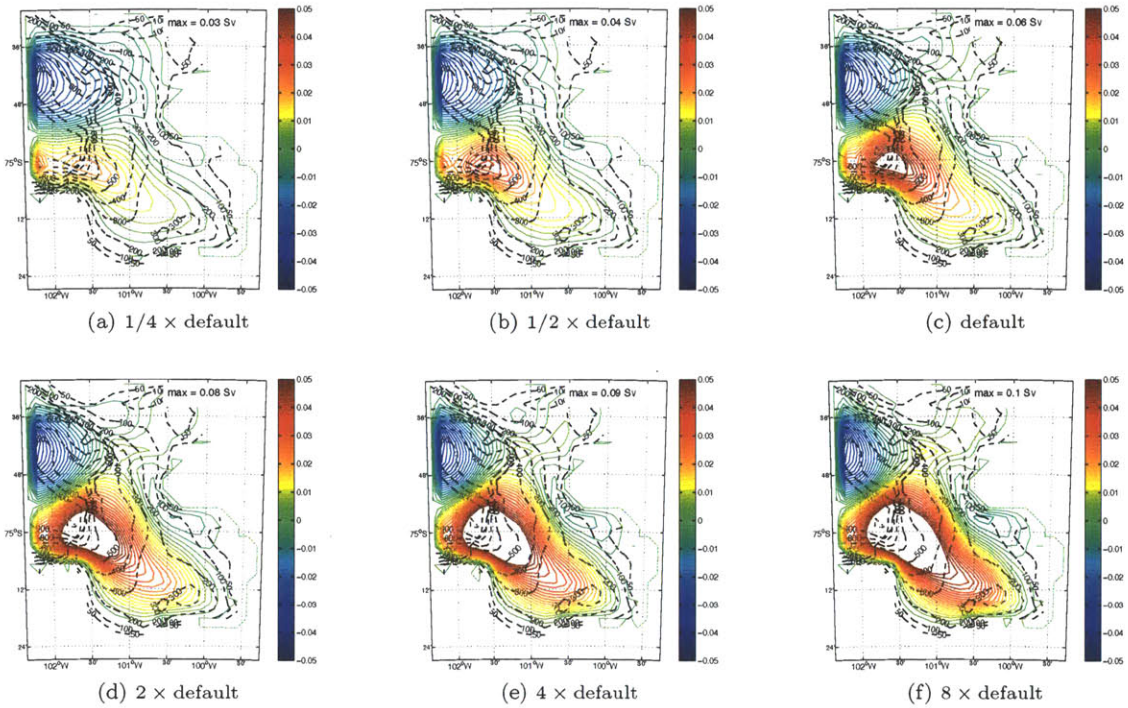

(a) 1/4 × default (b) 1/2 × default (c) default

(d) 2 × default (e) 4 × default (f) 8 × default

Figure 28: Barotropic streamfunction of the vertically integrated volume transport (Sv) for velocity-dependent realistic PIIS simulations using (a) $\frac{1}{4}$ × default C_d, (b) $\frac{1}{2}$ × default C_d, (c) default C_d, (d) 2 × default C_d, (e) 4 × default C_d, (f) 8 × default C_d. Dashed contours show the distribution of water column thickness (m) underneath the ice shelf. The maximum value of barotropic transport is indicated on each figure.

gradient and is in agreement with the observed acceleration of the mixed layer currents over the areas of plume outflow. In brief, the behavior of the idealized and realistic cavity models under variations of drag coefficient are consistent and in good agreement with the cavity dynamics theory presented in section 2.

These drag sensitivity experiments demonstrate that an important positive feedback between mixed layer velocities and melt rates and a negative feedback between mixed layer temperatures and melt rates occur when varying the magnitude of the drag at the ice shelf base. Only the second feedback can be accounted for in a velocity-independent model of the ice shelf-ocean interactions. In particular, the fact that the spatial distribution of melt rates in the velocity-dependent experiments is robust and does not seem to depend on the specific value of the drag coefficient is a valuable result, since in practice, the specific value of C_d underneath ice shelves is still unknown.

Our results also suggest that the inclusion of the velocity-dependent parameterization of $\gamma_{T,S}$ changes the dynamics underneath the ice shelf from a regime with fast mixed layer currents and low thermal forcing to a regime with slower currents and high thermal forcing. Although the large scale circulation in the cavity has a very similar structure in both cases, feedbacks between the smaller scale circulations, the distribution of hydrographic properties and the melt rates could induce two different thermodynamic regimes that are not straightforwardly comparable. Observations of hydrographic conditions and ocean currents under PIIS, or perhaps under another typical 'warm' ice shelf, would be necessary to determine which of the two regimes is more realistic. The significantly lower melt rates obtained in the realistic velocity-dependent simulations is another surprising result. According to the sensitivity experiments in the realistic PIIS setup, a value of drag coefficient more than 16 times that suggested by Holland and Feltham (2006) and Holland and Jenkins (1999)

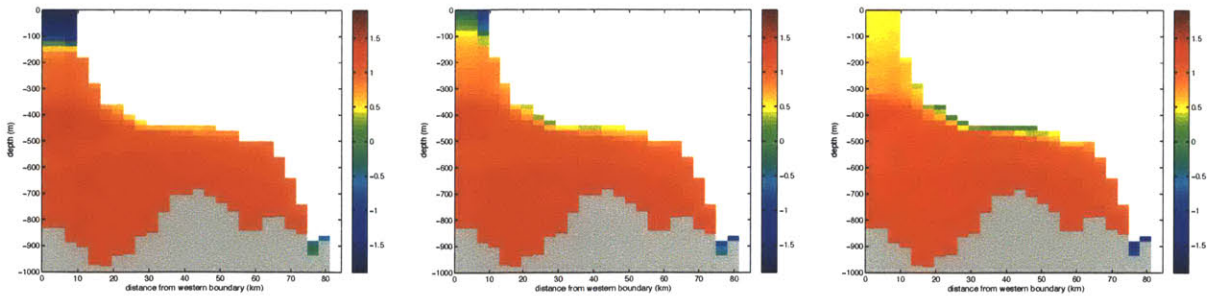

(a) 1/4 × default (b) 1/2 × default (c) default

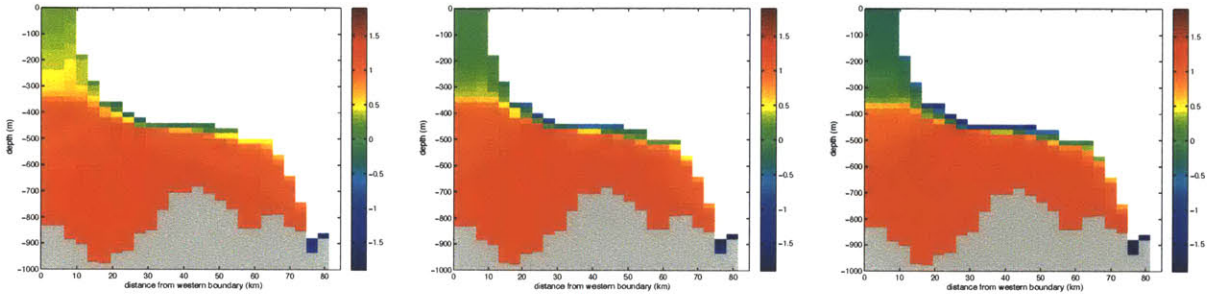

(d) 2 × default (e) 4 × default (f) 8 × default

Figure 29: Vertical cross-sections of potential temperature (°C) along the path identified in figure 5a for the velocity-dependent realistic PIIS simulations using (a) $\frac{1}{4}$ × default C_d, (b) $\frac{1}{2}$ × default C_d, (c) default C_d, (d) 2 × default C_d, (e) 4 × default C_d, (f) 8 × default C_d.

would be needed to match velocity-independent and velocity-dependent melt rates. This is a much higher value of C_d than typically used in ice shelf models. Payne et al. (2007) also simulated melt rates underneath PIIS using a velocity-dependent plume model with realistic bathymetry, ice shelf topography and hydrographic conditions. Their results were in best agreement with an ice flux divergence calculation based on surface mass balance, ice thickness and ice flow data for $C_d = 3.0 \cdot 10^{-3}$. Their ice flux calculation indicated melt rates in excess of 100 m/yr over some localized areas, a PIIS proper average of 26 m/yr and a cavity average of about 18 m/yr. Such melt rates are consistent in magnitude with the present PIIS velocity-independent experiment, but require the use of a drag coefficient about 10 × as high as our default value. This suggests that the default value of C_d has been chosen to fit average sub-ice shelf velocities that are much larger than those under PIIS and closer to the 0.2 m/s average ocean current velocity implied in the velocity-independent formulation of $\gamma_{T,S}$, for instance, those under Ross Ice Shelf (MacAyeal, 1984a,b,c).

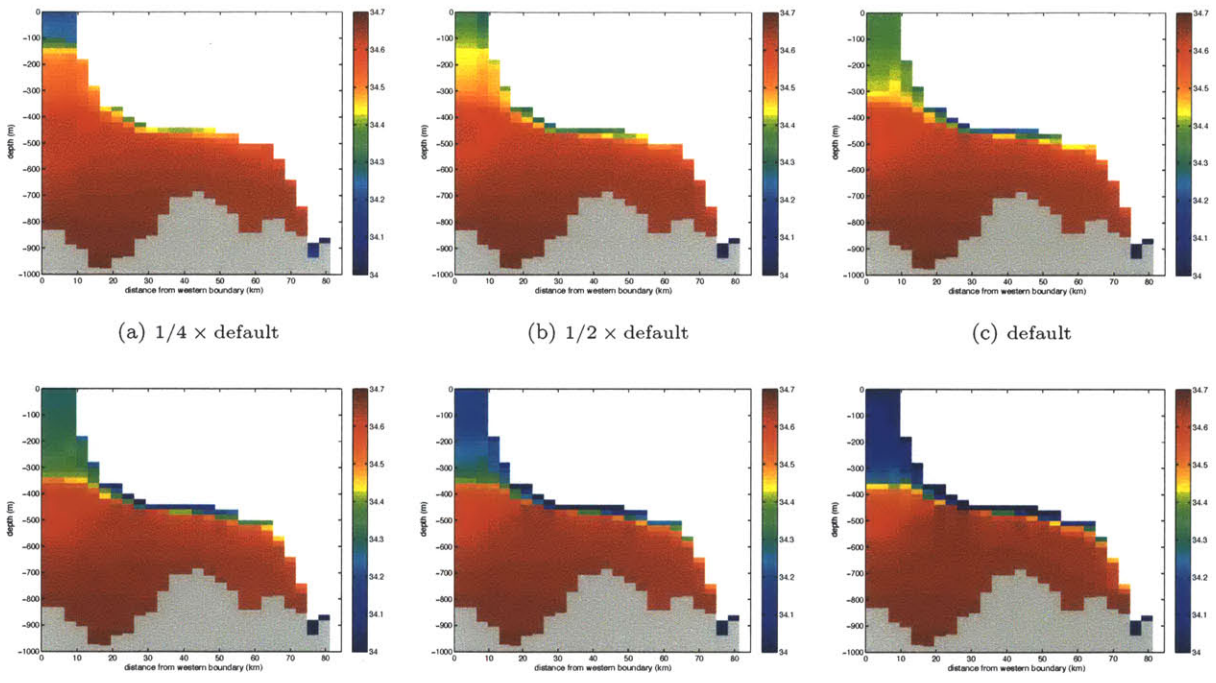

(a) 1/4 × default (b) 1/2 × default (c) default

(d) 2 × default (e) 4 × default (f) 8 × default

Figure 30: Vertical cross-sections of salinity (psu) along the path identified in figure 5a for the velocity-dependent realistic PIIS simulations using (a) $\frac{1}{4}$ × default C_d, (b) $\frac{1}{2}$ × default C_d, (c) default C_d, (d) 2 × default C_d, (e) 4 × default C_d, (f) 8 × default C_d.

4.3 Effect of the cavity geometry on the melt rate and circulation patterns

In this section, we discuss the effect of varying the ice shelf base steepness and the slope of the bedrock on the circulation and melt rates underneath the ice shelf. Six experiments are performed using an idealized cavity geometry. In a first step, the ice shelf base slope is varied and the bedrock is maintained flat (at 1000 meters depth). The 'default' ice shelf base slope case described in sections 4.1 and 4.2 is compared to a 'steep' and a 'gentle' ice shelf base slope simulations. In another set of experiments, the ice shelf base slope is kept to the 'default' angle and the bedrock topography is varied between a 'flat', an 'upslope' and a 'downslope' case (as illustrated in figure 2). The experiments performed here are very similar in many regards to the simulations of Little et al. (2008). An important difference however is the introduction of the velocity-dependent parameterization of the turbulent exchange velocities. Here, results of simulations using the velocity-independent and velocity-dependent formulations of $\gamma_{T,S}$ are contrasted to highlight differences in the model's response to changes in cavity geometry and indicate possible feedbacks between the melt rates, the topographically and melt-induced potential vorticity gradients and the strength of the cavity circulation. In the velocity-dependent simulations, a drag coefficient of 0.006 is used ($4 \times$ default) so that to obtain melt rates, mixed layer velocities and thermal forcings of magnitude similar to that of the velocity-independent simulations and hence allow some comparisons between the two types of experiments.

4.3.1 Varying the ice shelf base slope

Spatial distribution and magnitude of the melt rates

Comparison of the melt rates patterns shown in figure 31 indicates that both the area-averaged and maximum melt rates underneath the ice shelf increase with the slope of the ice shelf base. This result is in agreement with previous investigations of the melt rate sensitivity to the ice shelf base profile described in section 2.2.1 (Determann and Gerdes, 1994; Grosfeld and Gerdes, 1997; Holland et al., 2008; Little et al., 2008) which suggest that the potential for melting and refreezing is determined by the gradient of temperature along the ice shelf base. Here, the increase is seen when using either the velocity-independent or the velocity-dependent parameterization of $\gamma_{T,S}$. In both cases, the overall structure of the melt rate pattern is conserved under the changes of ice shelf base steepness. That is, the maximum melt rates in the velocity-independent simulations remains concentrated over the northeastern corner of the cavity where thermal forcing is highest (see figures 33d, 33e, 33f) and high melt rates in the velocity-dependent simulations still occur over the fast outflow path of the plume, along the grounding line and over the southeastern interior portion of the cavity where mixed layer velocities are high (see figures 32a, 32b, 32c).

In both the velocity-dependent and independent experiments, the area-averaged mixed layer velocity does not vary significantly when changing the slope of the ice shelf base (see figure 32). On the other hand, the maximum U_M is highest for the gentle shelf base slope cases, although the differences between the gentle and default cases are small in the velocity-dependent simulations. Over the interior part of the domain, where mixed layer currents mostly follow contours of potential vorticity, U_M increases with the steepness of the basal slope. This is consistent with an increase in the gradient of temperature at the ice shelf base maintaining stronger geostrophic currents, in thermal wind balance. Another way of explaining the increase in U_M is to consider that the zonal density gradient between the region of melting along the grounding line and the open ocean where no phase changes occur is highest for the steepest ice shelf since it both supports the fastest melting and has the smaller zonal extent. On the other hand, the mixed layer velocity over the plume region increases when decreasing the basal slope, which compensates for the decrease over the interior part of the

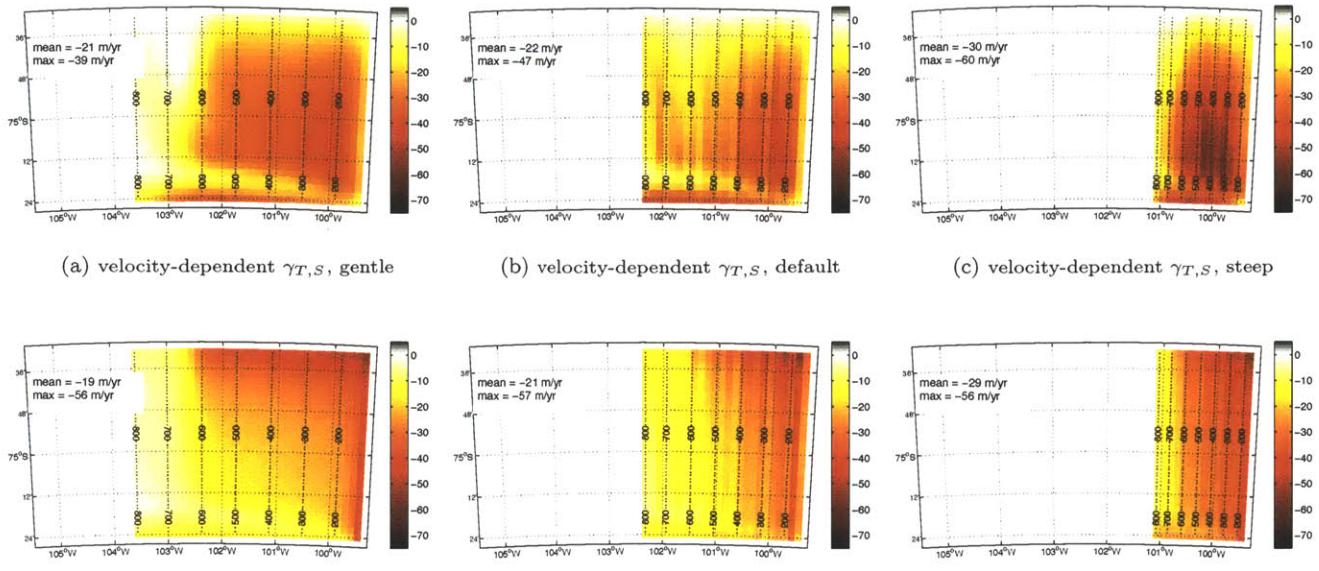

(a) velocity-dependent $\gamma_{T,S}$, gentle (b) velocity-dependent $\gamma_{T,S}$, default (c) velocity-dependent $\gamma_{T,S}$, steep

(d) velocity-independent $\gamma_{T,S}$, gentle (e) velocity-independent $\gamma_{T,S}$, default (f) velocity-independent $\gamma_{T,S}$, steep

Figure 31: Melt rate (m/yr) underneath an idealized ice shelf of constant basal slope with (a,d) gentle (b,e) default (c,f) steep inclinaison. Upper panels show results from the velocity-dependent simulations and lower panels, the results of velocity-independent simulations. Dotted black contours show the distribution of water column thickness (m) underneath the ice shelf.

cavity and explains why the area-averaged mixed layer velocity is the same between all three simulations, in both the velocity-dependent and velocity-independent experiments. The occurrence of faster plume outflow in the gentler ice shelf base slope cases suggests that stratification limits the velocity of the plume. This is in agreement with the work of Little et al. (2008), who mentioned that stronger dissipation of buoyancy is to be expected along steeper ice shelf base slopes. The area-averaged thermal driving also increases with the slope of the ice shelf base (see figure 33), but not the maximum thermal driving[14]. Comparison of the three different ice shelf profiles suggests that the increase in area-averaged thermal driving is due to the reduction of the area over which the cold meltwater plume spreads underneath the ice shelf and is also consistent with a more efficient dissipation of buoyancy flows along steeper slopes.

The variability of the mixed layer velocity as well as the area-averaged thermal driving under the change of basal slope is similar for the velocity-independent and velocity-dependent cases. If the sensitivity to the ice shelf profile was largely different between the two types of experiments, or if the drag coefficient was properly tuned, we could stipulate that part of the difference in sensitivity is due to positive feedbacks captured only by velocity-dependent formulation. For instance, a reinforcement between accelerated melt rates and increased mixed layer velocities over the interior part of the cavity could be expected in the velocity-dependent experiments. However, differences between the two cases occurring here are much too small to be clearly attributable to the specific formulation of $\gamma_{T,S}$.

[14]This is less clearly seen in the velocity-independent cases, since thermal driving is significantly lower in these simulations than in the velocity-dependent simulations when using $C_d = 0.006$ (and all other values of C_d investigated in section 4.2).

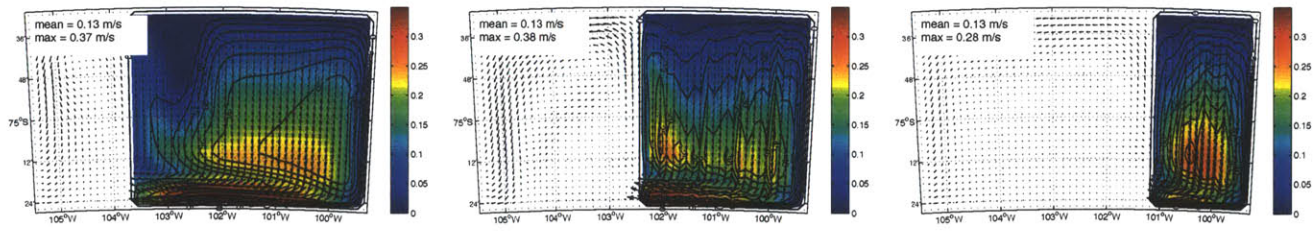

(a) velocity-dependent $\gamma_{T,S}$, gentle (b) velocity-dependent $\gamma_{T,S}$, default (c) velocity-dependent $\gamma_{T,S}$, steep

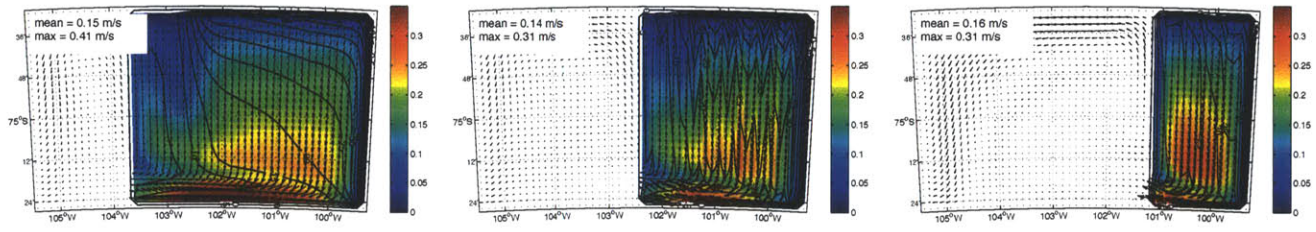

(d) velocity-independent $\gamma_{T,S}$, gentle (e) velocity-independent $\gamma_{T,S}$, default (f) velocity-independent $\gamma_{T,S}$, steep

Figure 32: Ocean mixed layer velocity, U_M (m/s), calculated for an ice shelf base of constant slope with (a,d) gentle (b,e) default (d,f) steep inclinaison. Upper panels show results from the velocity-dependent and lower panels, the results of velocity-independent simulations. Vectors indicate the direction and relative magnitude of the mixed layer currents. Black contours show the melt rate distribution (m/yr).

Overturning and barotropic circulation

As seen on figure 34, the depth-integrated volume transport increases with the slope of the ice shelf base. The increase between the gentle and steep slope cases is of almost 25% in both the velocity-dependent and velocity-independent simulations. However, it must be kept in mind that this particular calculation is influenced by both the actual change in shelf base topography and the resulting change in total water volume in the cavity, which increases significantly for steeper ice shelves. Looking at cross sections of zonal currents along the northern boundary of the cavity (see figure 35, bottom panels), we can nonetheless attribute part of the increase in transport to an intensification of the eastward boundary current for steeper ice shelf bases. This intensification is induced by the increase in melt rates. The resulting strengthening of the buoyancy flux accelerates the cyclonic circulation at depth (Little et al., 2008). As mentioned earlier, we observe that the westward intensified boundary current along the southern cavity wall is strongest in the gentle slope cases (see figure 35, top panels). This is somewhat counter-intuitive as one would expect a higher water column thickness gradient to drive a stronger ageostrophic current in the steep shelf base experiments. On the other hand, it agrees with the idea that diffusion of buoyancy fluxes is more efficient under stronger stratification, i.e., along steeper slopes.

The shape and magnitude of the meridional-averaged overturning circulation does not change significantly under the variation of basal shelf slope (not shown). This is somewhat unexpected since buoyancy forcing (melting) is increasing with the ice shelf base slope. However, identification of the effects of basal slope on the overturning circulation is complicated here because a modification in ice shelf base slope also changes the distance of the ice front from the western boundary at which zonal ocean currents are prescribed. In some

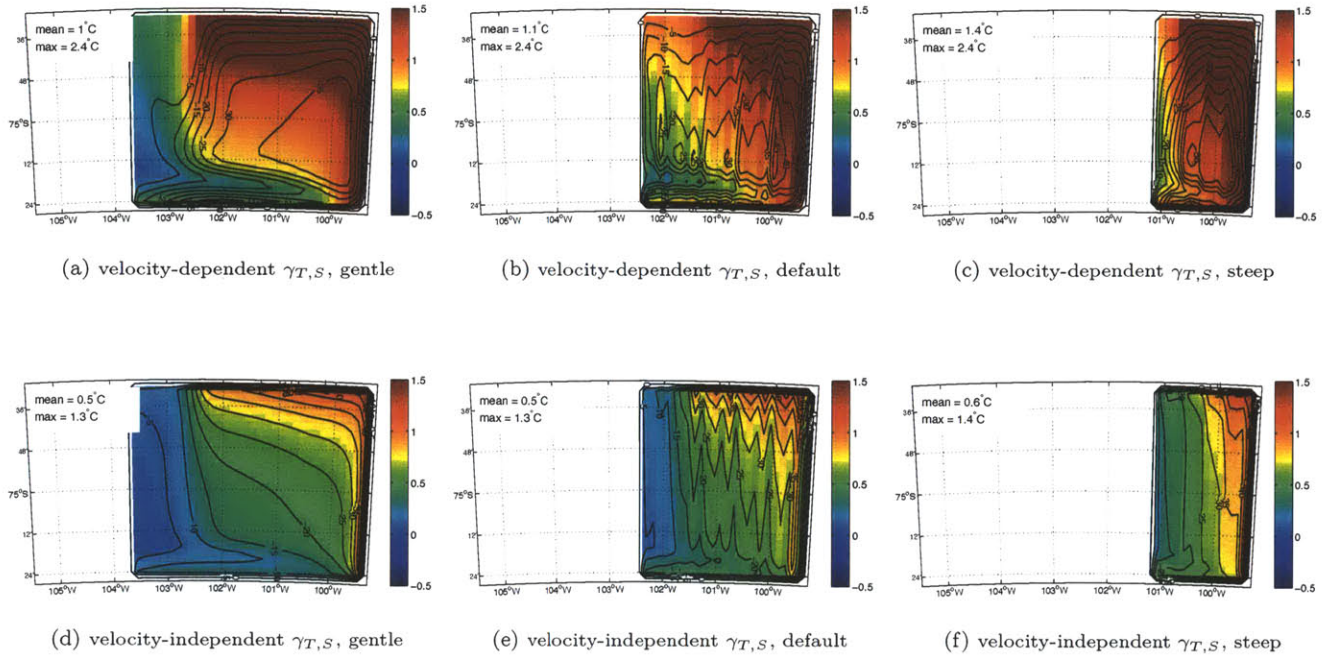

(a) velocity-dependent $\gamma_{T,S}$, gentle (b) velocity-dependent $\gamma_{T,S}$, default (c) velocity-dependent $\gamma_{T,S}$, steep

(d) velocity-independent $\gamma_{T,S}$, gentle (e) velocity-independent $\gamma_{T,S}$, default (f) velocity-independent $\gamma_{T,S}$, steep

Figure 33: Thermal forcing ($T_M - T_B$, °C) calculated for an ice shelf base of constant slope with (a,d) gentle (b,e) default (c,f) steep inclinaison. Upper panels show results from the velocity-dependent simulations and lower panels, the results of velocity-independent simulations. Black contours show the melt rate distribution (m/yr)

cases, this allows for some artificial recirculations to be set in the open ocean in front of the cavity. The present experimental setup therefore does not allow us to draw insightful conclusions from the calculation of the overturning circulation.

The similarity between the vertically-integrated volume transport calculated for the velocity-independent and velocity-dependent simulations is of interest here. According to Little et al. (2008), the cyclonic flow at depth set up by buoyancy fluxes dominates over the topographically-constrained mixed layer geostrophic transport in setting the overall depth-integrated circulation. Since large disparities in the spatial pattern of melting between the velocity-independent and velocity-dependent experiments occur, we would therefore expect the shape of the cyclonic circulation to differ between the two sets of simulations. In particular, because of the concentration of the highest melt rates in the southern portion of the cavity in the velocity-dependent experiments, we would expect a net southward shift of the center of the circulation in these simulations. This is clearly not the case here. However, figure 34 shows that the shape of the depth-integrated circulation is sensitive to the steepness of the prescribed ice shelf base profile, in both the velocity-dependent and velocity-independent experiments. Our results therefore suggest that buoyancy fluxes are not as strong a control on the depth-integrated circulation in the cavity and that the control from ice shelf base topography might be more important than previously thought. This result becomes particularly interesting when considering that the more realistic representation of stratification in the present experiments compared to that of Little et al. (2008) (50 layers compared to 10 layers in the model of Little et al. (2008) and experiments started from a uniform temperature field of -1.9C) would on the contrary be expected to weaken the effect of topographic constraints and strengthen the control of buoyancy fluxes on the interior cavity circulation.

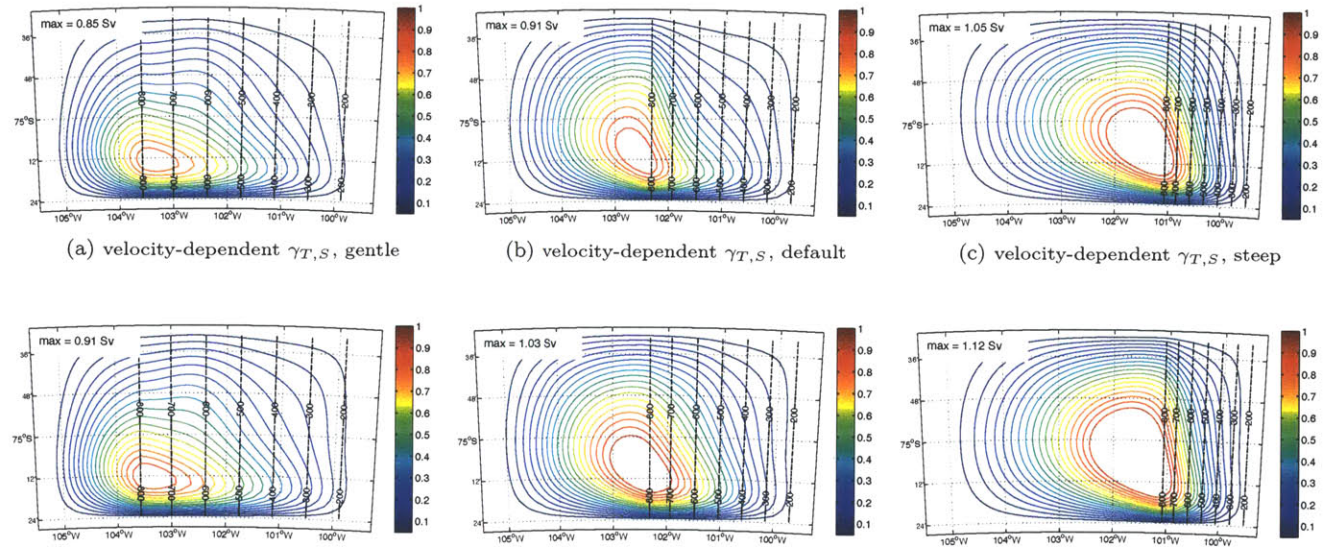

(a) velocity-dependent $\gamma_{T,S}$, gentle (b) velocity-dependent $\gamma_{T,S}$, default (c) velocity-dependent $\gamma_{T,S}$, steep

(d) velocity-independent $\gamma_{T,S}$, gentle (e) velocity-independent $\gamma_{T,S}$, default (f) velocity-independent $\gamma_{T,S}$, steep

Figure 34: Barotropic streamfunction for the depth-integrated horizontal volume transport (in Sv) calculated for an ice shelf base of constant slope with (a,d) gentle (b,e) default (c,f) steep profile. Upper panels show results from the velocity-dependent and lower panels, the results of velocity-independent simulations. Dashed black contours show the distribution of water column thickness (m).

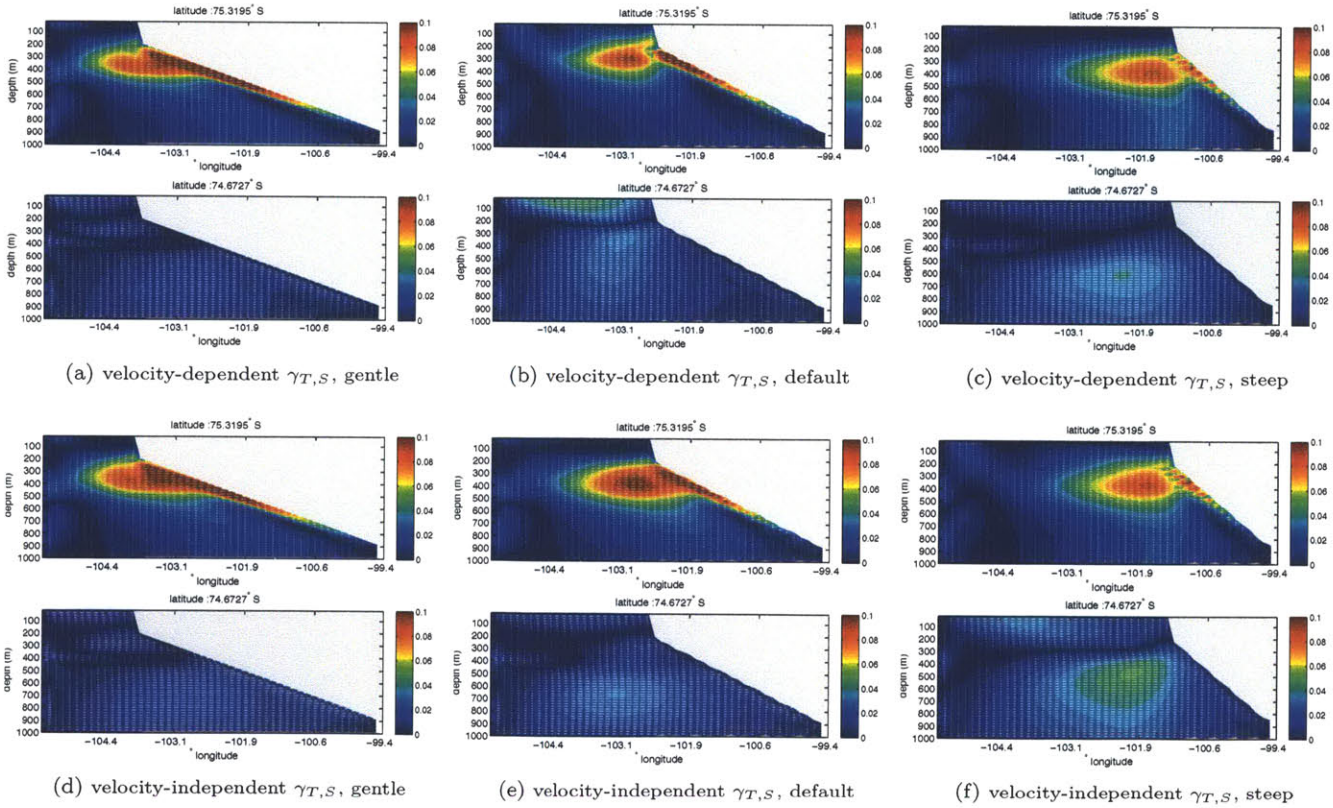

(a) velocity-dependent $\gamma_{T,S}$, gentle (b) velocity-dependent $\gamma_{T,S}$, default (c) velocity-dependent $\gamma_{T,S}$, steep

(d) velocity-independent $\gamma_{T,S}$, gentle (e) velocity-independent $\gamma_{T,S}$, default (f) velocity-independent $\gamma_{T,S}$, steep

Figure 35: Vertical cross-sections of zonal velocity underneath the ice shelf along the southern boundary (top panels) and northern boundary (bottom panels) for idealized ice shelf with constant slope and (a,d) gentle (b,e) default (c,f) steep inclinaison. Upper figures show results from the velocity-dependent simulations and lower figures, the results of velocity-independent simulations. Vectors indicate the direction and relative strength of the zonal currents.

4.3.2 Varying the bedrock slope

Here we compare three simulations in which the slope of the bedrock underneath the ice shelf is changed while the ice shelf base is kept to its 'default' profile. In the 'downslope' case, the bedrock depth increases towards the ice shelf front. In the 'upslope' experiments, it increases towards the grounding line. This last case is perhaps the most realistic of the three, as the sea bottom underneath ice shelf typically deepens inland due to isostatic sinking of the lithosphere and erosion during glacial periods (Holland et al., 2008). The default open boundary conditions in zonal ocean velocity need to be modified in the 'upslope' experiment, as the water column is 100 meters shallower at the western boundary in these simulations. This is not expected to impact the solution significantly, since, as mentioned in section 3, the model is relatively insensitive to the details of the prescribed profile of zonal velocity over a wide range of current magnitude. However, as the boundary and initial conditions in temperature and salinity are unchanged between the three experiments, the modifications in bathymetry results in differences in total volume of water in the cavity and most importantly, in the volume of the warmest waters sitting at depth. This, on the other hand, is likely to cause perceptible differences between the three solutions. Hence here, factors other than changes in bathymetry, such as the total ocean heat content, can cause results to vary between the three simulations. As in the previous section, the changes in melt rates are compared between two sets of experiments using the velocity-dependent and velocity-independent parameterization of $\gamma_{T,S}$ in order to identify possible feedbacks between buoyancy fluxes and ocean circulation induced by the modification in bedrock bathymetry.

Spatial distribution and magnitude of the melt rates

As seen in figure 36, both the spatial distribution and melt rate magnitude vary very little when changing the slope of the bedrock underneath the ice shelf and that, in both the velocity-independent and velocity-dependent experiments. Consistently with this insensitivity, no significant changes in the spatial distribution, mean and maximum of mixed layer velocity and thermal forcing are observed either. The slightly lower melt rates and thermal forcing in both the velocity-dependent and velocity-independent 'upslope' cases is a counter-intuitive result. Because of the westward gradient of potential vorticity set up at depth by the upsloping bathymetry, one would actually expect an intensification the eastward current along the northern boundary at depth, hence an increased flux of ocean heat towards the ice shelf base there and an acceleration of the melting. The opposite results are possibly explained by the reduction of the volume of warmest water at depth, which is greatest in 'upslope' setup and likely to dominate over bathymetric constraints in setting the overall thermal forcing at the ice shelf base.

Overturning and barotropic circulations

Although small, the differences in depth-integrated volume transport between the three cases are perhaps the most interesting result here. Comparison of the streamfunctions for the barotropic volume transport in the 'flat', 'downslope' and 'upslope' simulations (figure 39) show that the magnitude of the barotropic transport is largest for the 'upslope' and lowest for the 'downslope' case. Moreover, the meridional gradient in transport across the northern half of the cavity is also largest for the 'upslope' and lowest for the 'downslope' experiment, and that, in both the velocity-dependent and velocity-independent simulations. This is consistent with an intensification of against-potential vorticity gradient (eastward) inflow at depth along the northern cavity boundary in the 'upslope' bathymetry case that is clearly seen on cross-sections of the zonal current speed (see figure 40, lower panels). In turn, the increased inflow must be accompanied by a stronger return

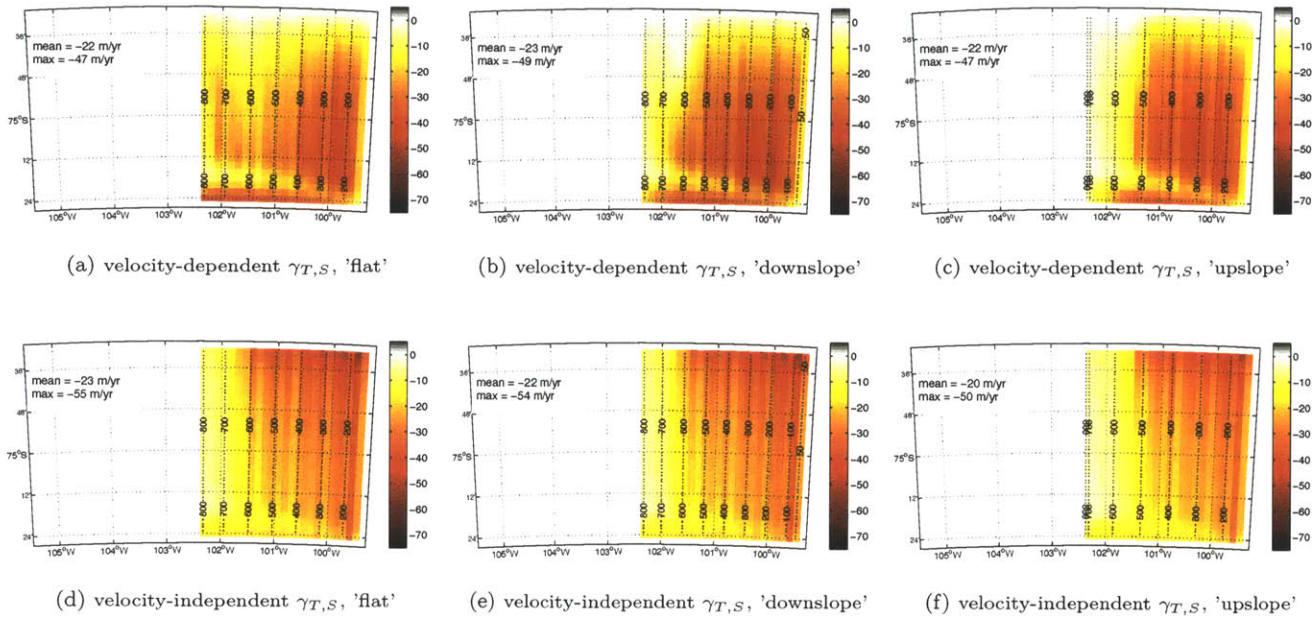

(a) velocity-dependent $\gamma_{T,S}$, 'flat' (b) velocity-dependent $\gamma_{T,S}$, 'downslope' (c) velocity-dependent $\gamma_{T,S}$, 'upslope'

(d) velocity-independent $\gamma_{T,S}$, 'flat' (e) velocity-independent $\gamma_{T,S}$, 'downslope' (f) velocity-independent $\gamma_{T,S}$, 'upslope'

Figure 36: Melt rate underneath the ice shelf (m/yr) calculated for an ice shelf cavity with a (a,d) flat, (b,e) downsloping, (c,f) upsloping bedrock bathymetry. Upper panels show results from the velocity-dependent simulations and lower panels the results of velocity-independent simulations. The maximum and area-averaged melt rates are indicated on each figure. Dotted contours show the water column thickness underneath the ice shelf (m).

(westward) transport over the southern half of the cavity and hence a more intense return current. Figure 40 (upper panels) shows that this indeed happens in the 'upslope' experiments. On the other hand, obtaining the strongest westward return current in the 'upslope' configuration seems counterintuitive because the zonal water column thickness gradient is the weakest in this case. However, it is consistent with findings of Little et al. (2008), who suggested that ice shelf base slope-induced instead of bedrock topography-induced gradient in potential vorticity is the main control on the intensification of return currents set up in the surface layers. Here, the ice shelf base topography is identical in all simulations. Hence the strength of the westward return current along the southern cavity boundary must be controlled by factors other than potential vorticity gradients in the upper layers, such as the strength of the inflow at the northern boundary. As mentioned above, the more intense barotropic transport in the 'upslope' case is not accompanied by higher melt rates, probably because of the lower total ocean heat content in this cavity configuration. There is little to say about the meridionally integrated overturning circulation (not shown) since it looks very similar in both shape and strength for the three prescribed bathymetry profiles. The only interesting point is that the 'downsloping' bathymetry forces the ascent of the warm water at depth towards the grounding line. No significant effect is observed with regards to the melt rates here, but we can hypothesize that in the presence of a steeper bedrock slope, the forced motion would promote faster melting.

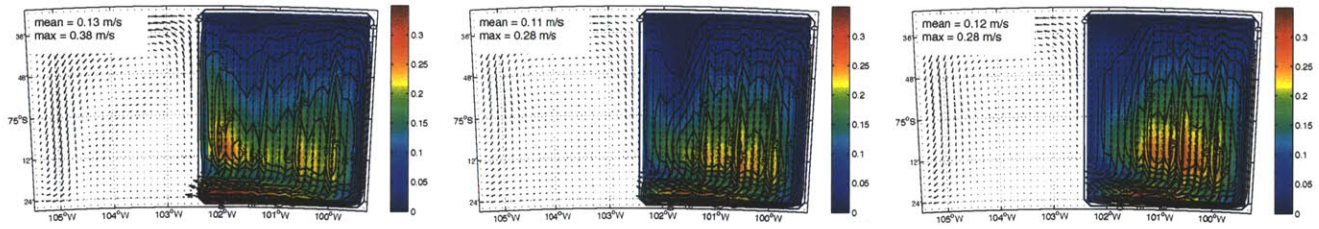

(a) velocity-dependent $\gamma_{T,S}$, 'flat' (b) velocity-dependent $\gamma_{T,S}$, 'downslope' (c) velocity-dependent $\gamma_{T,S}$, 'upslope'

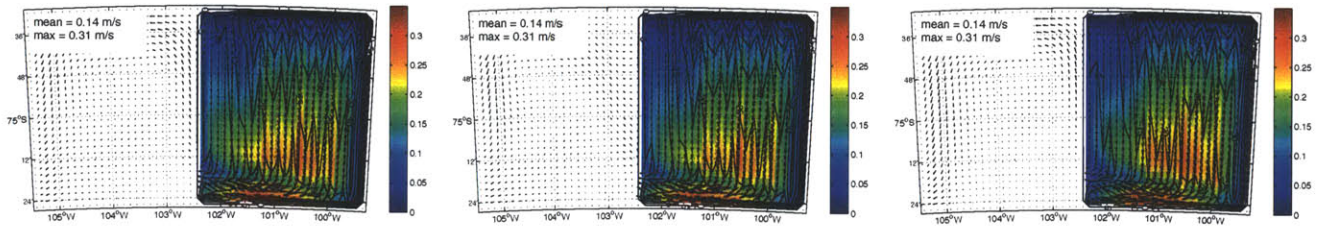

(d) velocity-independent $\gamma_{T,S}$, 'flat' (e) velocity-independent $\gamma_{T,S}$, 'downslope' (f) velocity-independent $\gamma_{T,S}$, 'upslope'

Figure 37: Ocean mixed layer velocity, U_M (m/s), calculated for an ice shelf cavity with a (a,d) flat, (b,e) downsloping, (c,f) upsloping bedrock bathymetry. Upper panels show results from the velocity-dependent simulations and lower panels, the results of velocity-independent simulations. The maximum and area-averaged mixed layer velocities are indicated on each figure. Black contours show the melt rate distribution (m/yr) and vectors indicate the direction and relative strength of the mixed layer currents.

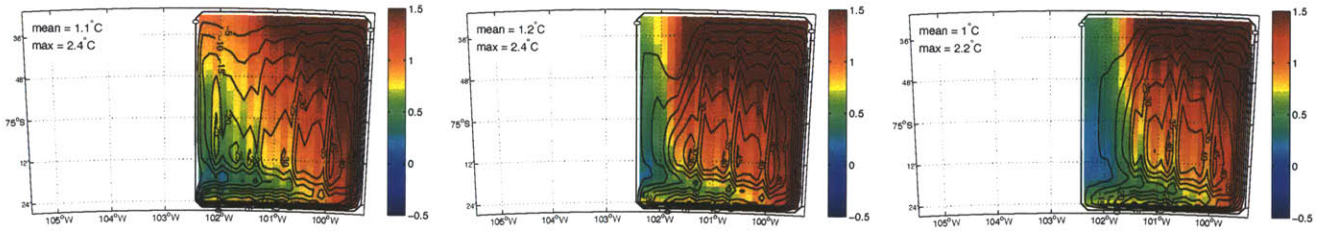

(a) velocity-dependent $\gamma_{T,S}$, 'flat' (b) velocity-dependent $\gamma_{T,S}$, 'downslope' (c) velocity-dependent $\gamma_{T,S}$, 'upslope'

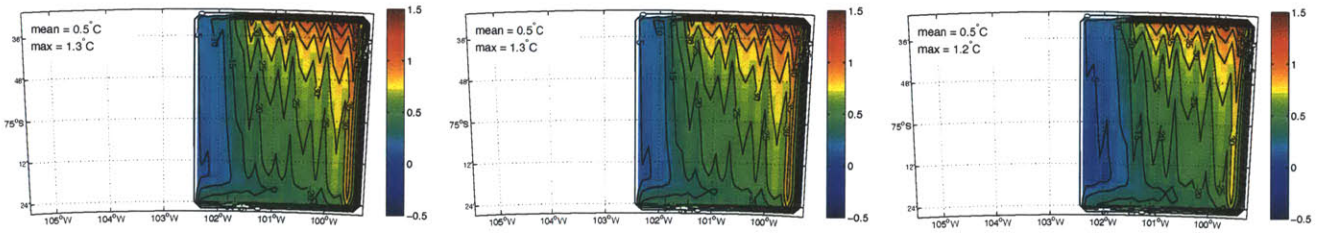

(d) velocity-independent $\gamma_{T,S}$, 'flat' (e) velocity-independent $\gamma_{T,S}$, 'downslope' (f) velocity-independent $\gamma_{T,S}$, 'upslope'

Figure 38: Thermal forcing ($T_M - T_B$, °C) calculated for an ice shelf cavity with a (a,d) flat, (b,e) downsloping, (c,f) upsloping bedrock bathymetry. Upper panels show results from the velocity-dependent simulations and lower panels, the results of velocity-independent simulations. Black contours show the melt rate distribution (m/yr) inside the cavity and the maximum and area-averaged thermal forcings are indicated on each figure.

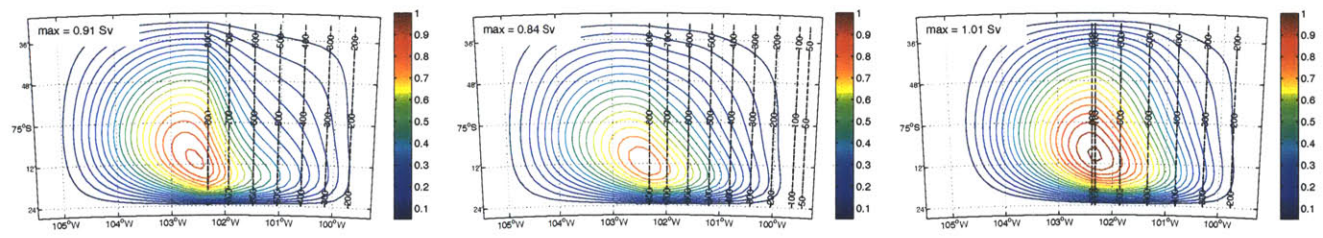

(a) velocity-dependent $\gamma_{T,S}$, 'flat' (b) velocity-dependent $\gamma_{T,S}$, 'downslope' (c) velocity-dependent $\gamma_{T,S}$, 'upslope'

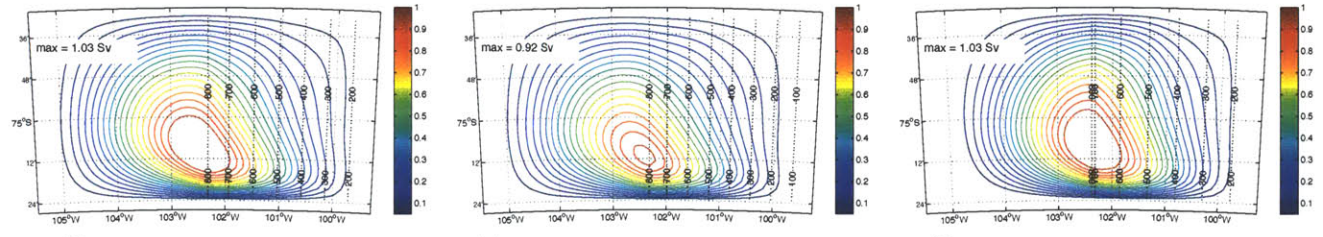

(d) velocity-independent $\gamma_{T,S}$, 'flat' (e) velocity-independent $\gamma_{T,S}$, 'downslope' (f) velocity-independent $\gamma_{T,S}$, 'upslope'

Figure 39: Barotropic streamfunction for the depth-integrated horizontal volume transport (in Sv) calculated for an ice shelf cavity with a (a,d) flat, (b,e) downsloping, (c,f) upsloping bedrock bathymetry. Upper panels show results of the velocity-dependent and lower panels, the results of velocity-independent simulations.

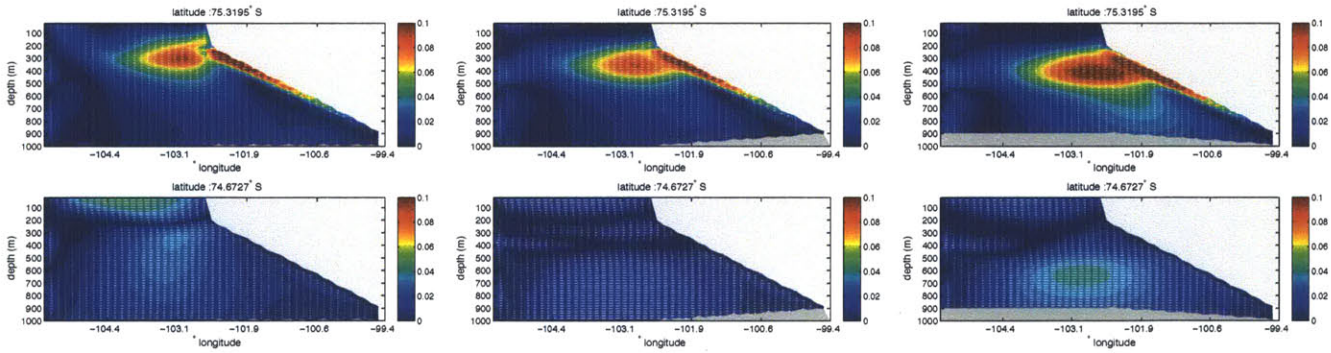

(a) velocity-dependent $\gamma_{T,S}$, 'flat' (b) velocity-dependent $\gamma_{T,S}$, 'downslope' (c) velocity-dependent $\gamma_{T,S}$, 'upslope'

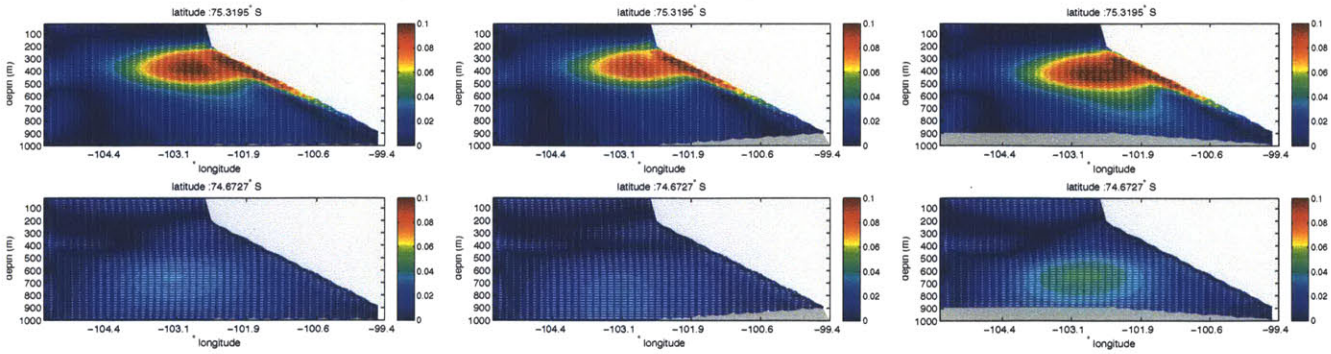

(d) velocity-independent $\gamma_{T,S}$, 'flat' (e) velocity-independent $\gamma_{T,S}$, 'downslope' (f) velocity-independent $\gamma_{T,S}$, 'upslope'

Figure 40: Vertical cross-sections of zonal current speed underneath the ice shelf along the southern boundary (top panels) and northern boundary (bottom panels) for an idealized ice shelf cavity with a (a,d) flat, (b,e) downsloping, (c,f) upsloping bedrock bathymetry. Upper figures show results from the velocity-dependent and lower figures, the results of velocity-independent simulations. Vectors indicate the direction and relative strength of the zonal ocean currents.

The experiments performed in this section show that the ice shelf base topography does influence the melt rates and strength of the circulation through dynamic processes, notably by setting a background potential vorticity gradient across the ice shelf. This is observed in both the velocity-dependent and the velocity-independent simulations. In agreement with the results of earlier studies mentioned previously, steeper ice shelves support faster basal melting here. No appreciable variation in melt rates are obtained when changing the topography of the seabed, consistently with the finding of (Little et al., 2008) that bathymetry is not a strong control on the depth-integrated volume transport in the cavity, especially in the presence of a realistic stratification. More importantly, we observe no significant difference in the model's sensitivity to both the ice shelf base and bedrock topography between the velocity-independent and velocity-dependent parameterizations of the melt rates. That is, the melting patterns differ largely between the two formulations of $\gamma_{T,S}$, as discussed in previous sections, but the impacts of changing the model's cavity geometry are similar for simulations using either parameterization. This is somewhat unexpected. The increase in melting with steepness of the ice shelf base should induce a positive feedback between mixed layer velocities and ablation rates that would be captured only by the velocity-dependent model. Also, from theory, we would expect the strengthening of the warm eastward currents along the northern cavity boundary in the 'upslope' bathymetry case to affect the intensity of melting over the northeastern portion of the cavity. In both the velocity-independent and velocity-dependent cases, a stronger current should result in a faster melting over the northeastern cavity corner. In the velocity-dependent case only, this should induce a positive feedback between enhanced melting and faster mixed layer currents. Perhaps more important variations in the slope of the ice shelf base and bedrock topography would be necessary in order to trigger such feedbacks in our model. In the present setup however, more drastic changes in cavity configuration would result in even more important differences in total volume of water and initial heat content in the cavity and would further complicate the analysis of the simulations. Experiments initiated from rest and uniform conditions of temperature and salinity and in which no profiles of hydrographic properties and/or current velocities are prescribed at open boundaries would probably allow for a more efficient investigation of feedbacks between cavity geometry and velocity-dependent melt rates, but would also be more representative of the dynamics of 'cold' than 'warm' ice shelf cavities.

4.4 Modulation of the melt rate and circulation patterns from tidal forcing

One of the main motivations for the development of a velocity-dependent parameterization of ablation rates underneath ice shelves is to allow thermodynamic processes at the ice interface to be directly coupled to one of the primarily source of turbulent kinetic energy in ice shelf cavities, that is, tides. Previous studies have indicated that tides are an important driver of the thermodynamic processes within 'cold' cavities (MacAyeal, 1984a,b,c; Holland, 2008; Mueller et al., 2012; Makinson et al., 2012), which are characterized by tidal currents that are strong compared to buoyancy-induced flows. That this is the case as well for 'warm' cavities remains uncertain. Authors have recently hypothesized that the tidal contribution to melting underneath warm ice shelves might be limited, as their thermohaline circulation is strong and tidal currents, comparably weak (Holland, 2008; Mueller et al., 2012). However, at least three processes are susceptible to enhance the effect of tides on warm ice shelf cavities. The first is the transfer of energy from the tidal frequency to higher harmonic oscillations (i.e., waves) through non-linear interactions. The second is the generation of time-independent currents over critical ventilation pathways underneath the cavity (Mueller et al., 2012; Payne et al., 2007). The third is tidal mixing at or close to the grounding line (Holland, 2008). In the following, we focus on

- investigating and comparing the the temporal variability of velocity-dependent and velocity-independent melt rates and the associated cavity circulations,
- identifying tidal contribution to the time-independent cavity flow through tidal rectification and its impact on the velocity-dependent and independent melt rates,
- assessing the extent and contribution of tidal mixing to the ablation rates.

We do so in the context of both an idealized 'warm' ice shelf and a realistic PIIS cavity configuration. The generation of topographic waves and baroclinic tides by interactions of the periodic flow with the bedrock and ice shelf base topography (Mueller et al., 2012) is beyond the scope of the present work and is left for further investigations. It is also important to note that we noticed a small bug in the simulations performed in this section. In all model runs here, the drag coefficient at the ice shelf base is set to $2.5 \cdot 10^{-3}$ in the momentum equation, independently of the value of the drag coefficient used in the melt rate parameterization. This mismatch in the value of the drag coefficient is however thought to have little impact on the results presented here. A test simulation in which this bug was fixed indeed indicated only very small differences in the model solution, which consisted in slightly lower maximum and negligibly lower mean melt rates in both the velocity-dependent and velocity-independent experiments.

4.4.1 Melt rate variability

To begin, we analyze the structure and amplitude of the melt rate response to tidal forcing in both the idealized and realistic PIIS cavity. In particular, we compare the modulating effects of tides on the cavity circulation and ablation rates parameterized using both the velocity-dependent and velocity-independent formulations of the turbulent exchange velocities.

Idealized experiments

In a first set of experiments, the model in the idealized ice shelf configuration is forced with meridionally homogeneous, pure diurnal and semi-diurnal tidal current signals. The response of melting and cavity circulation is analyzed. The behavior of the model forced with tidal currents of 0.2 m/s in amplitude is first

described. Such a current amplitude lies in the range of high tidal forcing for Antarctic ice shelves (Holland and Jenkins, 1999; Holland, 2008; Mueller et al., 2012) and was chosen to bring out clearly the characteristics of the cavity's response to tidal forcing. A drag coefficient of $C_d = 6.0 \cdot 10^{-3}$ ($4 \times$ default) was used in the velocity-dependent parameterization of $\gamma_{T,S}$ in order to ease the comparison of the variability of the velocity-dependent and velocity-independent models. As in all experiments previously described, these simulations are forced with the time-independent profile of zonal ocean velocity shown in figure 6a (dashed curve). The total zonal velocity forcing prescribed at the open (western) boundary is thus the sum of a a time-dependent contribution from barotropic tidal currents and of a time-independent profile for the deep inflow and surface outflow currents in front of the cavity.

Figure 41 shows time series of the prescribed profiles of semi-diurnal (left panels) and diurnal (right panels) tidal currents along with the area-averaged thermal forcing, mixed layer velocity and melt rate responses of the velocity-dependent (upper panels) and velocity-independent (lower panels) model. For all four simulations (velocity-dependent and velocity-independent, diurnal and semi-diurnal tides experiments) the response of the model in terms of thermal forcing and mixed layer velocity is similar in structure and has the following characteristics:

- Thermal forcing (second panel, red curve) behaves as an almost pure sine with period equal to that of the prescribed tidal currents. The maximum and minimum in thermal forcing over one tidal cycle both occur at times of reversal in current amplitude, from inflowing to outflowing and from outflowing to inflowing respectively.

- The response in area-averaged mixed-layer velocity (second panel, gray curve) is not a pure mono-periodic sine, but indicates a superposition of at least two signals with periods equal to that of the tidal forcing and half of the tidal forcing. The absolute maximum within one cycle of U_M coincides with the maximum inflow of warm water at depth, while the secondary maximum is timed with the maximum outflow of surface water. Two minima in U_M occur over one cycle and both coincide approximately with the moment at which the direction of the tidal current forcing reverses.

- In the semi-diurnal and diurnal tides experiments, the maximum in thermal forcing lags the fastest inflow of warm water at depth by about two and four hours respectively. Hence there is a shift of approximately $\frac{1}{6}$ of a tidal cycle between the absolute maxima in thermal forcing and that in mixed layer velocity.

The response in melt rates is similar in structure between the diurnal and semi-diurnal tides experiments. However, important differences occur between velocity-dependent and velocity-independent simulations in terms of the temporal variability of ablation rates. The maximum and area-averaged velocity-independent melt rates evolve as pure sine signals and are in phase with the thermal forcing. On the other hand, both the maximum and area-averaged velocity-dependent melt rates mimic the non-linear behavior of the mixed layer velocity. In the diurnal tides experiments, the absolute maxima in melt rates and U_M are however slightly out of phase. This is explained by the increased phase difference between $T_M - T_B$ and U_M with respect to the diurnal experiment, and to the fact that high thermal forcing at this moment in the cycle also contributes significantly to the diffusive heat flux. The absolute maximum in area-averaged melt rate therefore occurs between the maximum in U_M and the maximum in thermal forcing. The second maxima in the area-averaged and maximum melt rates coincide with the second maximum in (outflowing) mixed layer velocity. At that time, thermal forcing is at a near-minimum.

In the following, we describe one diurnal tidal cycle in terms of the location and timing of the maximum velocity-dependent and velocity-independent melt rates and of the thermodynamical forcings underneath the

ice shelf[15]. The amplitude of the tidal currents is of 0.2 m/s. The first two columns of figure 42 show 4-hourly snapshots of the perturbed thermal forcing (or surface layer velocity over the open ocean where $T_B = 0$) and mixed layer velocity (surface velocity over the open ocean). The vectors superimposed on these fields indicate the relative magnitude and direction of the perturbed depth-integrated horizontal volume transport. Perturbed quantities were obtained by subtracting a 1-period average of a given field from its individual snapshots. The third and fourth columns of figure 42 show respectively the instantaneous velocity-dependent and velocity-independent melt rates underneath the ice shelf along with instantaneous (time averaged plus perturbed) depth-integrated barotropic current vectors.

[15]The same description would apply to the very similar semi-diurnal tidal cycle.

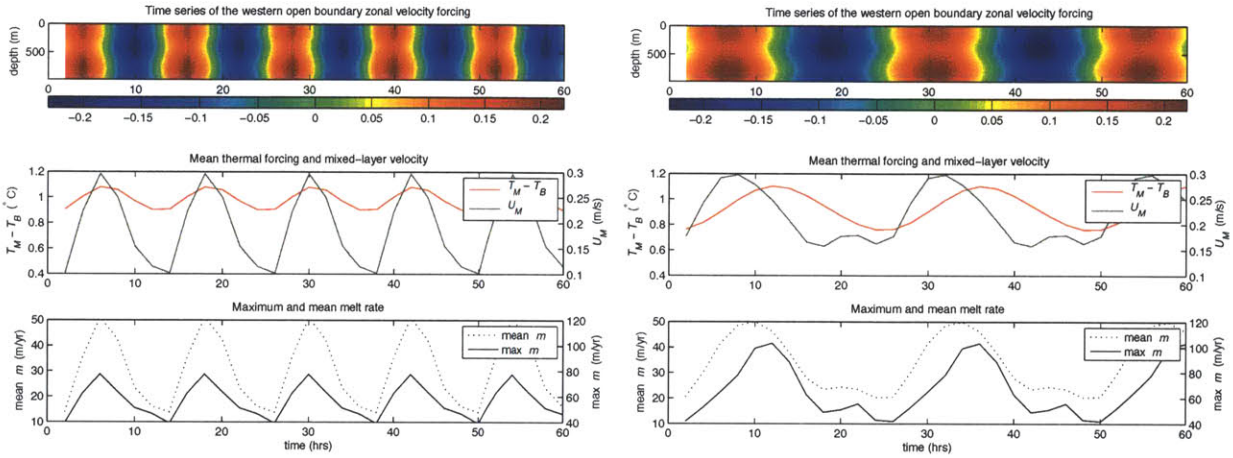

(a) velocity-dependent $\gamma_{T,S}$, 12 hrs tides

(b) velocity-dependent $\gamma_{T,S}$, 24 hrs tides

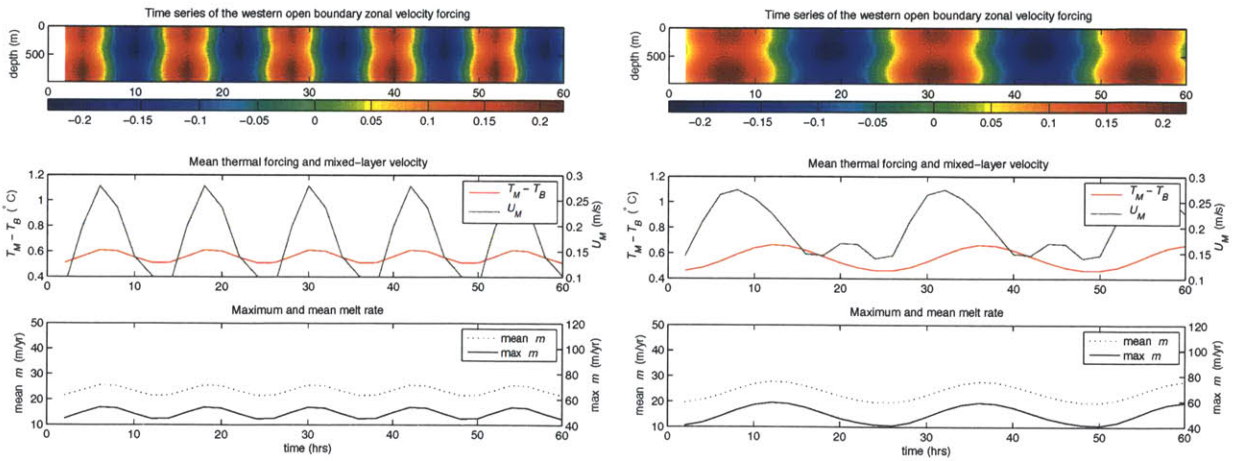

(c) velocity-independent $\gamma_{T,S}$, 12 hrs tides

(d) velocity-independent $\gamma_{T,S}$, 24 hrs tides

Figure 41: Evolution of the zonal current forcing profile (m/s) prescribed at the open boundary (upper subplots), of the area-averaged thermal forcing (red curve) and mixed layer velocity (gray curve, middle subplots) and of the area-averaged (dotted curve) and maximum (solid curve) melt rates (lower subplots) over a period of 2.5 days following the 3-years model spinup. Panels (a) and (b) show the results of the velocity-dependent idealized simulations forced respectively with semi-diurnal and diurnal tides with amplitude $|\hat{\mathbf{U}}_\mathbf{T}| = 0.20$ m/s. Panels (c) and (d) show the results of the velocity-independent idealized simulations forced with semi-diurnal and diurnal tides of the same amplitude.

The tidal cycle analyzed here starts with a half period of inflow tides. During this time, an eastward pressure gradient is induced by the convergence of mass into the cavity. The resulting flow is directed inside the cavity, and deflected to the left by the eastward topographically-induced gradient of potential vorticity, as indicated by the vectors for the depth-integrated volume transport. During this period of strengthening currents (between $t = 4$ hours and $t = 8$ hours), the mixed layer velocity increases, starting from the southwestern portion of the cavity. At this point, mixed layer currents are relatively weak along the grounding line. The velocity-dependent melt rates increase accordingly with the intensification of the mixed layer velocity and reach a maximum at about $t = 8$ hours.

At the beginning of the cycle, thermal forcing is anomalously low, hence velocity-independent melt rates are too. Thermal forcing increases during the entire period of inflow, starting along the grounding line, and reaches a maximum when tidal forcing reverses direction ($t \approx 12$ hours). By that time, the mixed layer velocity has decreased over most of the cavity with the slowing of the inflow tidal currents. However, strong currents remain along the grounding line, which is consistent with the increase in melt rates there and hence with a strengthening of the buoyancy-induced density gradient across the ice shelf. Consequently, the depth-integrated tidal currents at this point are strong (southward) along the grounding line and intensify in the return (westward) flow along the southern wall of the cavity. Hence, as mixed layer velocities decrease over the interior part of the domain with decreasing inflow and then with the intensifying outflow tides, U_M remains high along the grounding line and actually increases along the plume outflow. The depth-integrated tidal currents over most of domain also become more westward as the outflowing tidal forcing intensifies. This further accelerates the plume outflow. Between $t = 20$ and $t = 24$ hours, the plume is the fastest. A second maxima in velocity-dependent melt rates occurs because of the rapid melting collocated with the plume and the strong currents along the grounding line.

During the period of outflow (between $t = 16$ hours and $t = 24$ hours), thermal forcing decreases over most of the domain. The pressure gradient set up by the divergence of mass in the cavity drives outflowing currents which are slightly deflected to the left, accordingly to the topographically-induced potential vorticity gradient. The divergence of mass underneath the ice shelf is consistent with the spreading of the meltwater produced during the previous maxima in melting. As the cold buoyant water insulates the base the ice shelf, velocity-independent melt rates decrease everywhere. At the end of the outflow half-period, around $t = 24$ hours, the temperature forcing reaches a minimum. So does the mixed layer velocity, with the decrease of the tidal currents, and the velocity-dependent melt rates.

This decomposition of a tidal cycle brings up an important difference between the evolution of the thermal and mixed layer velocity forcings, and consequently, of the velocity-independent and velocity-dependent melt rates. Under the effect of tides, the spatial pattern of thermal forcing is unaltered. The temperature difference across the boundary layer increases and decreases everywhere with all spatial proportions kept, and so does the velocity-independent melt rates. On the other hand, the mixed layer velocities vary greatly in space during one tidal cycle, such that velocity-dependent melt rates underneath the ice shelf change in both location and intensity.

The occurrence of multiple maxima in U_M and velocity-dependent melt rates can also be explained in terms of the generation of higher frequency perturbations by non-linear interactions. In shallow water environments, such as the innermost areas of ice shelf cavities, contributions to the momentum balance and mass-conservation from processes such as advection and frictional drag can become significant. In the presence of a periodic forcing in sea surface elevation and/or currents, these non-linear terms can act as source terms at sums, differences, and multiples of the frequencies of the forcing signals. Walters (1986; 1987) described extensively the generation

of higher frequency dynamical forcings by tides. In the following, his treatment of the simple 2-dimensional shallow water system is summarized.

The momentum and mass conservations equation for the shallow water system read

$$\frac{\partial \mathbf{u}}{\partial t} + \mathbf{u} \cdot \nabla \mathbf{u} + \mathbf{f} \times \mathbf{u} = -g\nabla\eta + \tau, \tag{34}$$

$$\frac{\partial \eta}{\partial t} + \nabla \cdot [(h+\eta) \cdot \mathbf{u}] = 0. \tag{35}$$

In the presence of a periodic forcing such as tides, the response of the system can be analyzed by partitioning the vertically-averaged current velocities (u, v) and the free surface elevation η into a time-independent ($\overline{\mathbf{u}}$, $\bar{\eta}$) and a tidal perturbation component ($\hat{\mathbf{u}}$, $\hat{\eta}$), as done previously in section 2. In turn, the time-evolving component can be harmonically expanded as a linear sum of periodic components with frequencies corresponding to that of the known tidal signals, such that

$$\eta = \bar{\eta} + \frac{1}{2}\sum_{-N}^{N} \hat{\eta}_n \exp(i\omega_n t), \tag{36}$$

$$\mathbf{u} = \overline{\mathbf{u}} + \frac{1}{2}\sum_{-N}^{N} \hat{\mathbf{u}}_n \exp(i\omega_n t) \tag{37}$$

with ω_n, the given tidal frequency and $\hat{\eta}_n$ and $\hat{\mathbf{u}}_n$ the amplitude of each component. Separation of the different harmonics in the momentum and mass conservation equation is performed by substituting these expansions into (35) and eliminating all products of orthogonal terms[16]. Doing so, the following system of equations is obtained for each harmonic component, n:

$$(i\omega_n + \tau_n)\hat{\mathbf{u}}_n + \mathbf{f} \times \hat{\mathbf{u}}_\mathrm{n} + \mathrm{g}\nabla\hat{\eta}_\mathrm{n} = g\mathbf{T_n}, \tag{38}$$

$$i\omega_n\hat{\eta}_n + \nabla \cdot (H\hat{\mathbf{u}}_n) = -\frac{1}{2}\sum_{i,j} \nabla \cdot (\hat{\eta}_i\hat{\mathbf{u}}_j). \tag{39}$$

In this form, the momentum and mass conservation equations highlight contributions to tidal forcing from additional sources terms arising from non-linear interactions. The divergence of the wave transport on the right hand side of the mass conservation equation (39) is due to the non-orthogonality of tidal free surface height and current velocity signals (Walters, 1986) and it is non-zero only for $\omega_i + \omega_j = \omega_n$. τ_n is associated to the expansion of the drag term and hence depends on the specific drag parameterization employed. If the approximation of $\eta << h$ is made in the shallow water equation and if a quadratic drag formulation such as the one in equation (8) is employed for the bottom and ice shelf base drag, the expansion of τ_n takes the form

$$\tau_n = \frac{C_d}{h}\lambda + \frac{C_d}{8H\lambda}\sum_{i,j,k}[(\hat{\mathbf{u}}_i \cdot \hat{\mathbf{u}}_j)\hat{\mathbf{u}}_k]$$

where $\lambda = \frac{1}{2}(\sum_n 4\overline{\mathbf{u}}^2 + \hat{\mathbf{u}}_n \cdot \hat{\mathbf{u}}_{-n})^{\frac{1}{2}}$, $i \neq j$ and $\omega_i + \omega_j + \omega_k = \omega_n$ (Walters, 1986, 1987). In the formulation of the shallow water harmonic expansion by Walters 1986; 1987; 1991, the highest order (second) term in the equation of τ_n above is encapsulated into the following expression for $\mathbf{T_n}$:

$$\mathbf{T_n} = -\frac{1}{2g}\sum_{i,j}\hat{\mathbf{u}}_i \cdot \nabla\hat{\mathbf{u}}_j - \frac{C_d}{4gh\lambda}(\sum_{i,j,k}[\hat{\mathbf{u_i}} \cdot \hat{\mathbf{u_j}}]\hat{\mathbf{u_k}})$$

[16] by multiplying by the complex conjugate of $\hat{\eta}$ and $\hat{\mathbf{u}}$ respectively and integrating over time

with $i \neq -j$ and $\omega_i + \omega_j = \omega_n$ and which also includes non-linear terms associated with advection.

In the present case, the model is forced with mono-periodical tidal currents of frequency ω and therefore, $\omega_i = \omega_j = \omega_k = \omega$. Hence, from the harmonics expansion of the shallow water system above, one can expect non-linear contributions from divergence of wave transport (mass balance) and advection at frequencies

$$\omega_n = \omega_i + \omega_j = 2n\ \omega,$$

and from frictional drag at frequencies

$$\omega_n = \omega_i + \omega_j + \omega_k = 3n\ \omega.$$

In turn, interactions between these higher frequency perturbations can generate signals at the $\frac{5}{T}$, $\frac{7}{T}$, etc. frequencies. In particular, contributions from friction are expected to be significant in the present model, since drag applies at both the top (ice interface) and bottom (bedrock) of the water column and strong currents in the mixed layer underneath the ice shelf are likely to enhance frictional dissipation at the ice shelf base.

In the velocity-dependent formulations of Jenkins (1991) and Holland and Jenkins (1999), melt rates are a linear function of ocean current velocities. Thus melting itself is not a source term. However, in such parameterization, ablation rates are directly coupled to the dynamical part of the model through the formulation of the friction velocity (equation 8). In a velocity-dependent ice-shelf ocean model, variability in the melt rates is therefore expected at the frequency of the prescribed tidal current forcing as well as at frequencies of perturbations in $\hat{\mathbf{u}}$ generated by both the advection and the drag terms. Fourier analysis of hourly melt rate outputs from 30 days-long velocity-dependent simulations confirms this (see figure 43a). High amplitude signals actually coincide with frequencies of $\frac{n}{24\ \text{hrs}}$, with $n = 1, 2, 3, 4, ...$ The amplitude in area-averaged and maximum melt rates peaks at the frequency of the prescribed tidal forcing and decreases with ω for $\omega = \frac{2}{24\ \text{hrs}}$, $\frac{3}{24\ \text{hrs}}$ and $\frac{4}{24\ \text{hrs}}$. For higher frequencies, it oscillates only slightly. Comparing Fourier decompositions of time series of the mixed layer velocity (not shown) and melt rates in experiments forced with tidal currents of 0.02 m/s (figure 43a), 0.2 m/s (figure 43b) and 0.4 m/s (figure 43c) in amplitude shows that signals at the actual forcing frequency and at higher harmonics are strongest for the fastest tidal currents.

As melt rates are not explicitly a function of ocean current velocities in the velocity-independent model, variability arising from dynamical non-linearities will likely be weaker than in the velocity-dependent case. However velocity-independent melt rates are still linear functions of temperature and salt gradients that are set by heat and freshwater *fluxes* . Hence in a dynamics-thermodynamics coupled model, some variability at multiples of the tidal forcing frequency is expected. The presence of well-defined peaks on the periodograms of the thermal forcing (not shown) and of the mean and maximum velocity-independent melt rates time series (figures 43d, 43e and 43f) supports this idea. As expected, these calculations show that the velocity-independent melt rate signals at higher frequencies are much weaker than that of the velocity-dependent melt rates. The decrease in amplitude of the signals with increasing frequency is also faster.

Because of the direct coupling between ocean currents and melting at the ice shelf base, the variability in melt rates due to tidal forcing is significantly larger in the velocity-dependent than in the velocity-independent experiments. Comparison of panels in figure 41 shows that while the amplitude of the variations in thermal forcing and mixed layer velocities are comparable between the two cases, the variations are more than three times larger for the velocity-dependent than for the velocity-independent melt rates, for the same tidal forcing. This is consistent with the results of Jenkins et al. (2010b), who noticed that models responding only to temperature variations produce ablation rates with much reduced variability associated with tidal cycles compared to models including both temperature and frictional forcings at the ice-ocean interface.

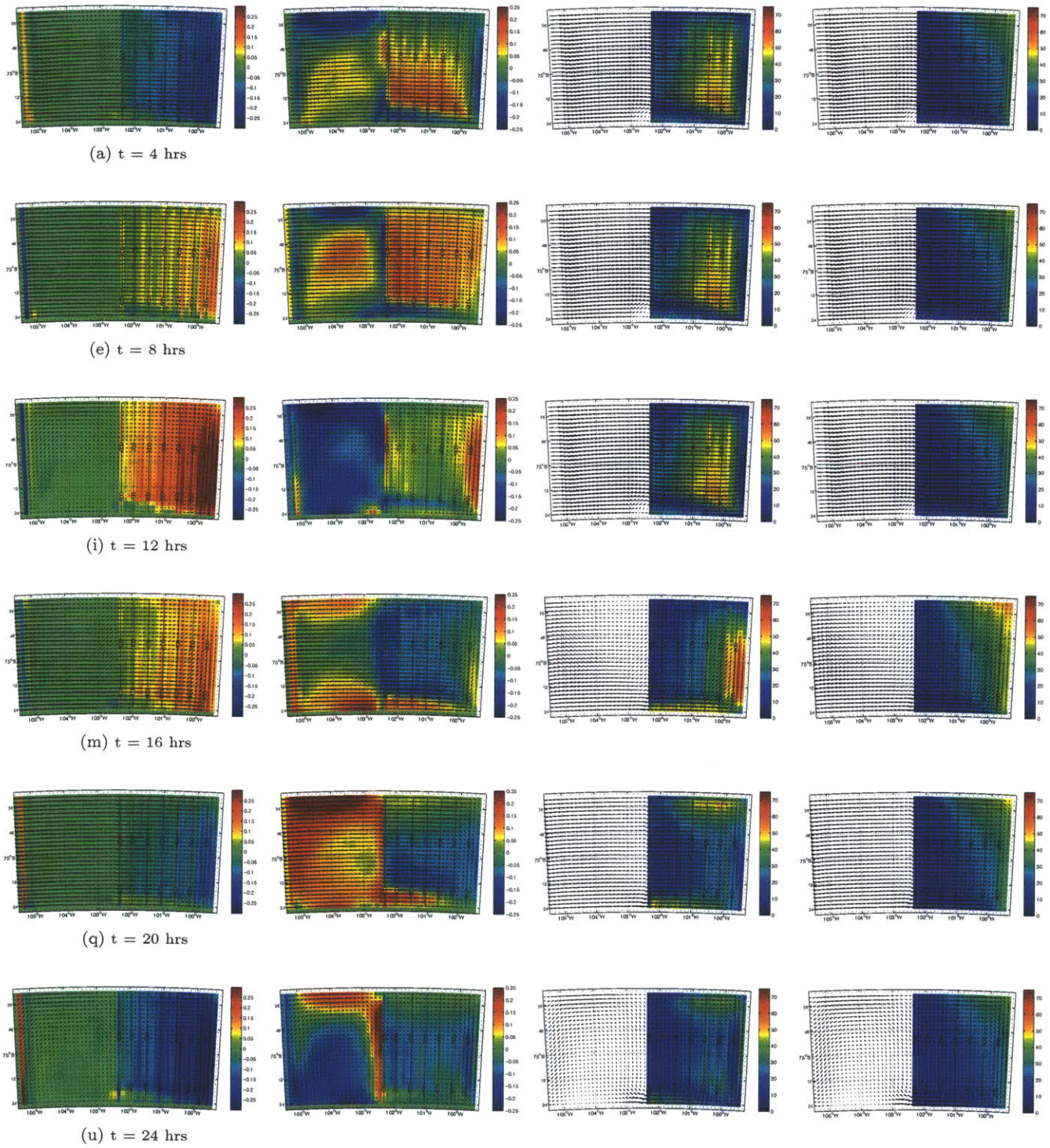

Figure 42: 4-hourly snapshots of the perturbed thermal forcing (first column), perturbed mixed layer velocity (second column), instantaneous velocity-dependent melt rates (third column) and instantaneous velocity-independent melt rates (fourth column) simulated with the idealized model forced with diurnal tides of 0.20 m/s in amplitude. The vectors superimposed on the perturbed field (first and second columns) indicate the direction and relative magnitude of the perturbed depth-integrated volume transport. The vectors superimposed on the melt rate fields (third and fourth columns) indicate the direction and relative magnitude of the time-averaged depth-integrated barotropic volume transport. Perturbed quantities are obtained by subtracting a 1-period average of a given field from its individual snapshots. Black contours on each panel show the distribution of water column thickness (m).

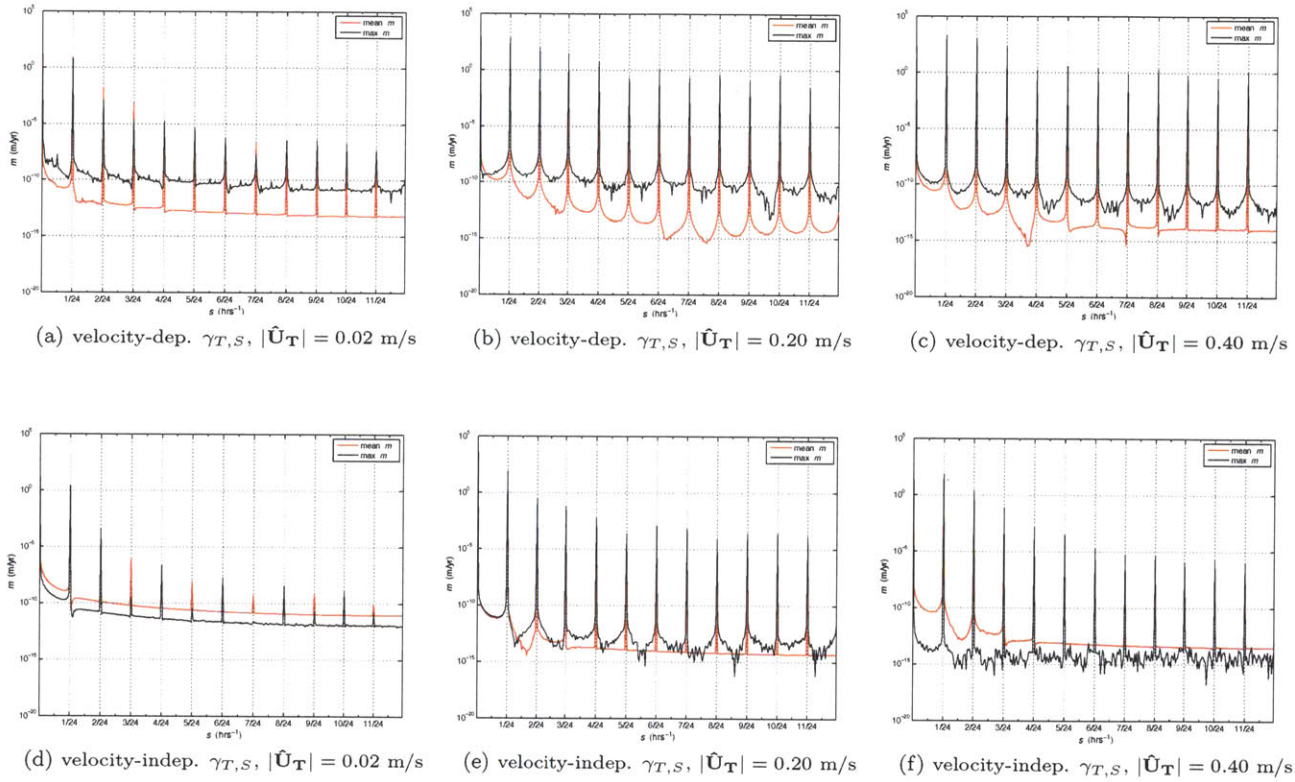

(a) velocity-dep. $\gamma_{T,S}$, $|\hat{\mathbf{U}}_\mathbf{T}| = 0.02$ m/s (b) velocity-dep. $\gamma_{T,S}$, $|\hat{\mathbf{U}}_\mathbf{T}| = 0.20$ m/s (c) velocity-dep. $\gamma_{T,S}$, $|\hat{\mathbf{U}}_\mathbf{T}| = 0.40$ m/s

(d) velocity-indep. $\gamma_{T,S}$, $|\hat{\mathbf{U}}_\mathbf{T}| = 0.02$ m/s (e) velocity-indep. $\gamma_{T,S}$, $|\hat{\mathbf{U}}_\mathbf{T}| = 0.20$ m/s (f) velocity-indep. $\gamma_{T,S}$, $|\hat{\mathbf{U}}_\mathbf{T}| = 0.40$ m/s

Figure 43: Periodogram of the area-averaged (red curve) and maximum (black curve) melt rates simulated in an idealized cavity forced with a pure diurnal tidal signal of three different amplitudes: (a, d) $|\hat{\mathbf{U}}_\mathbf{T}| = 0.02$ m/s, (b, e) $|\hat{\mathbf{U}}_\mathbf{T}| = 0.20$ m/s and (c, f) $|\hat{\mathbf{U}}_\mathbf{T}| = 0.40$ m/s. The upper panels show results from velocity-dependent simulations and the lower panels, that of velocity-independent simulations.

Realistic experiments

In this set of experiments, the realistic PIIS model is forced with mono-periodic diurnal and semi-diurnal tidal currents. As mentioned in section 3, the amplitude of these tidal signals was estimated by summing the four principal semi-diurnal and diurnal zonal tidal components simulated by the CATS02.01 model at 74.8°S, 102.375°W[17]. The difference in the maximum and minimum currents over one cycle (see figure 6e) was used as the signal's amplitude. Linear interactions between the four tidal constituents with slightly different frequencies results in periodic constructive and destructive interferences over longer time periods. Spring-neap modulations of the current amplitude are seen at the $\sim$ 14.7 days period for the diurnal and at the $\sim$ 13.7 days period for the semi-diurnal tides. The estimates (0.74 cm/s for the diurnal and 0.61cm/s for the semi-diurnal tides) obtained here are representative of constructive interference and hence are in the high range of tidal currents at this specific location. In the following, we assess the maximal response of the cavity model to tidal forcing. The constructed diurnal and semi-diurnal signals are assigned a zero phase and an exact period of 24.00 and 12.00 hours respectively. Tidal currents are zero at the first model time step (t = 0 hours). The sum of the time-independent profile of zonal ocean velocity given in figure 6a (solid line) and of the barotropic, meridionally-homogeneous, time-dependent zonal tidal currents are prescribed at the open western boundary. As the value of drag coefficient required to match velocity-independent and dependent melt rates in the realistic simulations is much higher than most values previously suggested in modeling studies and no physical argument points out to another specific value of C_d, the default drag coefficient is used here. Test simulations using higher values of C_d are also performed for comparison purposes.

The 'total' ocean current forcing over a period of 2.5 days is shown in figure 41 along with the area-averaged thermal forcing, mixed layer velocity, melt rate and maximum melt rate simulated by the velocity-dependent (upper panels) and velocity-independent (lower panels) models forced with the semi-diurnal (left panels) and diurnal (right panels) tidal currents. One important difference with respect to the idealized cases discussed previously is that here, the time series of simulated mixed layer currents and thermal forcing differ between the velocity-dependent and velocity-independent experiments. In the later case, thermal forcing is an almost pure sine. The mixed layer velocity signal shows some wave steepening but only one maxima and minima over one period. On the other hand, in the velocity-dependent experiments, the mixed layer velocity signal shows two maxima per cycle. This was also observed in the idealized velocity-dependent experiments, however, the timing of the absolute and second maximum are inverted in the present realistic case such that the highest mixed layer velocity is timed with the moment of maximum outflow currents and a second weaker maximum occurs at the timing of maximum inflow currents. A slight asymmetry is also present in the thermal forcing signal which was not observed in previous idealized experiments. The discrepancies between the two types of simulations is perhaps explained by the fact that the structure of the cavity circulation differs between the velocity-dependent and velocity-independent simulations, as discussed in section 4.1. As melt rates patterns also differ largely between the two cases, buoyancy fluxes are expected to induce different circulations at smaller scales and hence, to promote discrepancies in the distributions of water properties in the cavity. This could result in different responses of the cavity dynamics to tidal forcing. Also, non-linear interactions between the buoyancy-induced and topographically-constrained circulations in the realistic cases are expected to be amplified because of the more complex bathymetry and ice shelf base topography. All these factors likely contribute to the observed differences between the response of the two models to tidal forcing.

[17]This is the coordinate of the mid-point along the open ocean part of the western model boundary.

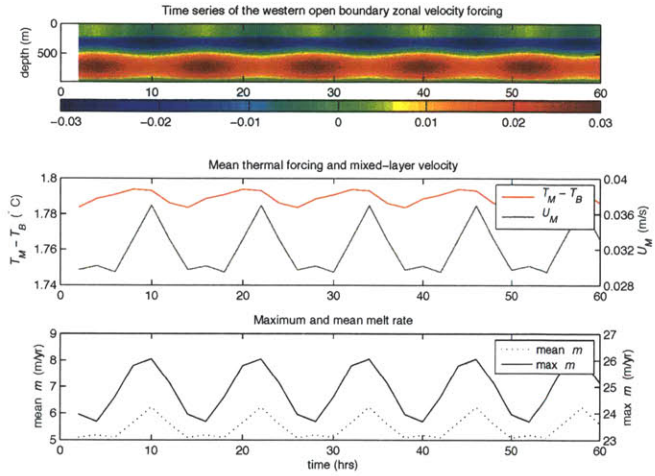

(a) velocity-dependent $\gamma_{T,S}$, 12 hrs tides

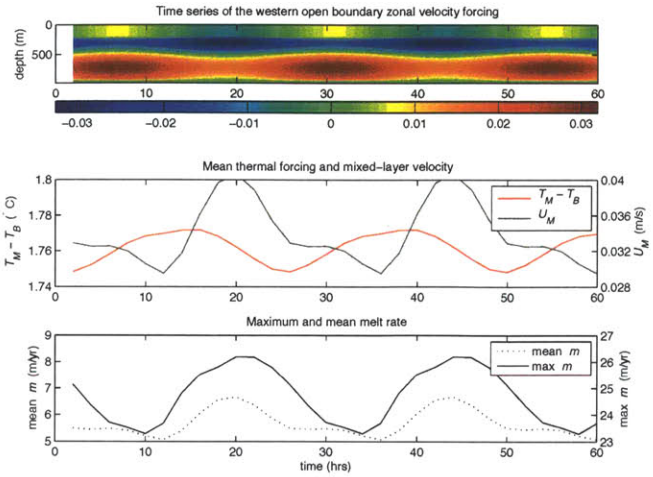

(b) velocity-dependent $\gamma_{T,S}$, 24 hrs tides

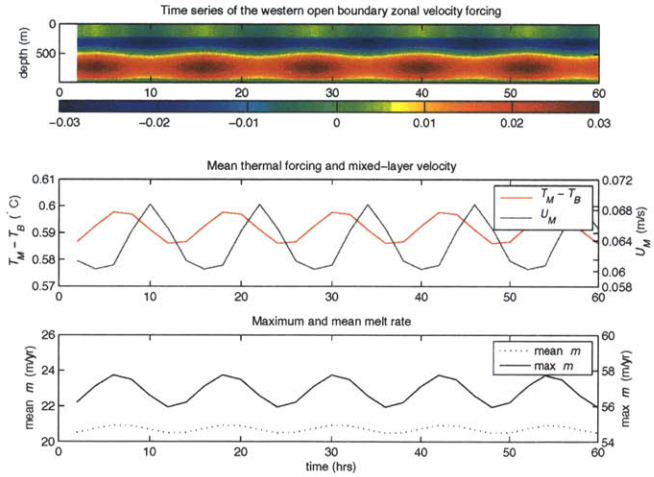

(c) velocity-independent $\gamma_{T,S}$, 12 hrs tides

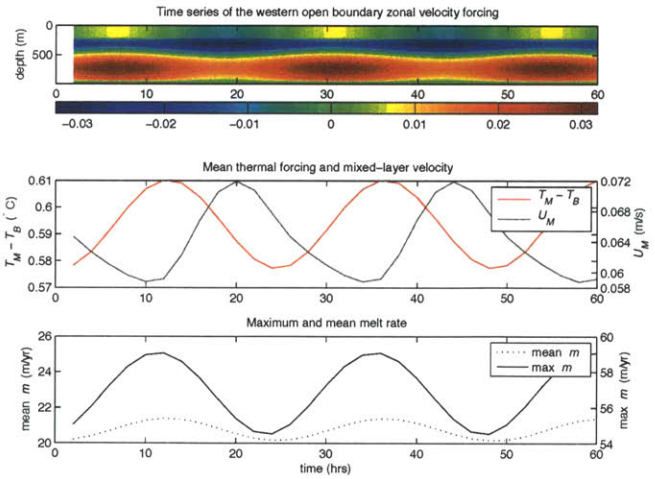

(d) velocity-independent $\gamma_{T,S}$, 24 hrs tides

Figure 44: Evolution of the zonal current forcing profile (m/s) prescribed at the open boundary (upper subplots), of the area-averaged thermal forcing (red curve) and mixed layer velocity (gray curve, middle subplots) and of the area-averaged (dotted curve) and maximum (solid curve) melt rates (lower subplots) over a period of 2.5 days following the 3-years model spinup. Panels (a) and (b) show the results of the velocity-dependent PIIS simulations forced with semi-diurnal and diurnal tides of realistic amplitude (0.61 cm/s and 0.74 cm/s respectively). Panels (c) and (d) show the results of the velocity-independent PIIS simulations forced respectively with semi-diurnal and diurnal tides of the same amplitude.

Despite these small discrepancies, which cause some differences in the amplitude of local features, the overall evolution of the thermal and ocean current forcings on the ablation rates is similar in the velocity-dependent and independent experiments. Here, the evolution of the melt rates in both cases is described in terms of the distribution of mixed layer velocity and temperature gradient at the base of the realistic PIIS ice shelf. Figure 45 compares 4-hourly snapshots of the tidal component[18] of $T_M - T_B$ and U_M (first two columns) and the corresponding instantaneous velocity-dependent and velocity-independent melt rate distribution (third and fourth columns respectively). In each figure of the two first columns, vectors indicate the direction and relative magnitude of the instantaneous depth-averaged tidal currents. In the figures of the two right columns, vectors of the time and depth-averaged ocean currents in the cavity are shown. The particular case represented here is that of the PIIS cavity forced with realistic diurnal tides. Semi-diurnal tides simulations show a very similar behavior.

Here, the tidal cycle starts with the half period of inflowing tidal currents that intensify the warm inflow at depth ($t = 4$ hours). As in the idealized cases, the eastward pressure gradient that is induced by the convergence of mass underneath the ice shelf drives inflow currents in the cavity. At this stage, tidal currents are strong in the southeastward branch of the large cyclonic circulation that characterizes the depth-integrated volume transport of PIIS proper in both the velocity-dependent and velocity-independent experiments (see figure 28). This intensified inflow following the 200 meters isobath northeast of the sill induces a local maximum in mixed layer velocity there. Over the northern portion of the cavity, another maximum in U_M is also concentrated along a strong inflowing current. In the velocity-dependent simulations, these features are accompanied by local maxima in melt rates. Over the following $\sim$ 3 hours, the inflowing tidal currents increase towards a maximum. Mixed layer velocities further increase northeast of the sill and over the northern part of the cavity and so does the velocity-dependent melt rates. This induces the weak maxima in U_M around $t = 8$ hours that coincides with maximum inflow currents at depth.

During the first quarter of the cycle ($t = 0 - 6$ hours, see $t = 4$ hours) thermal forcing is relatively low over most parts of the cavity. The velocity-independent simulation places the highest melt rates along the deepest reaches of the grounding line and over the inflowing branch of the cyclonic circulation extending from there. Over the whole half cycle of inflowing tidal currents, thermal forcing increases over most parts of the cavity. It reaches a maximum intensity around $t = 12$ hours, which is the timing of reversal of the tidal currents. Melt rates in the velocity-independent experiments are highest at this time. As tidal currents are zero at this point, mixed layer velocities are small, therefore velocity-dependent melt rates are at a relative minimum.

As the outflowing tidal currents strengthen over the next four hours, an outward pressure gradient is set up and divergence of mass out of the cavity drives outflowing tidal currents that intensify plume flows. The resulting strong mixed layer velocities increase the velocity-dependent melt rates, which reach a maximum around $t = 18$ hours. With the outflowing tidal currents, the cold meltwaters spread at the base of the ice shelf and thermal forcing decreases until the tidal flow reverses from outflowing to inflowing around $t = 24$ hours. At this time, velocity-independent melt rates reach their minimum. Between $t = 18$ and $t = 24$ hours, the prescribed outflowing currents decrease in intensity and so does the mixed layer velocities. The velocity-dependent melt rates therefore decrease as well towards a minimum at $t = 24$ hours.

[18] anomaly with respect to a 1-period average

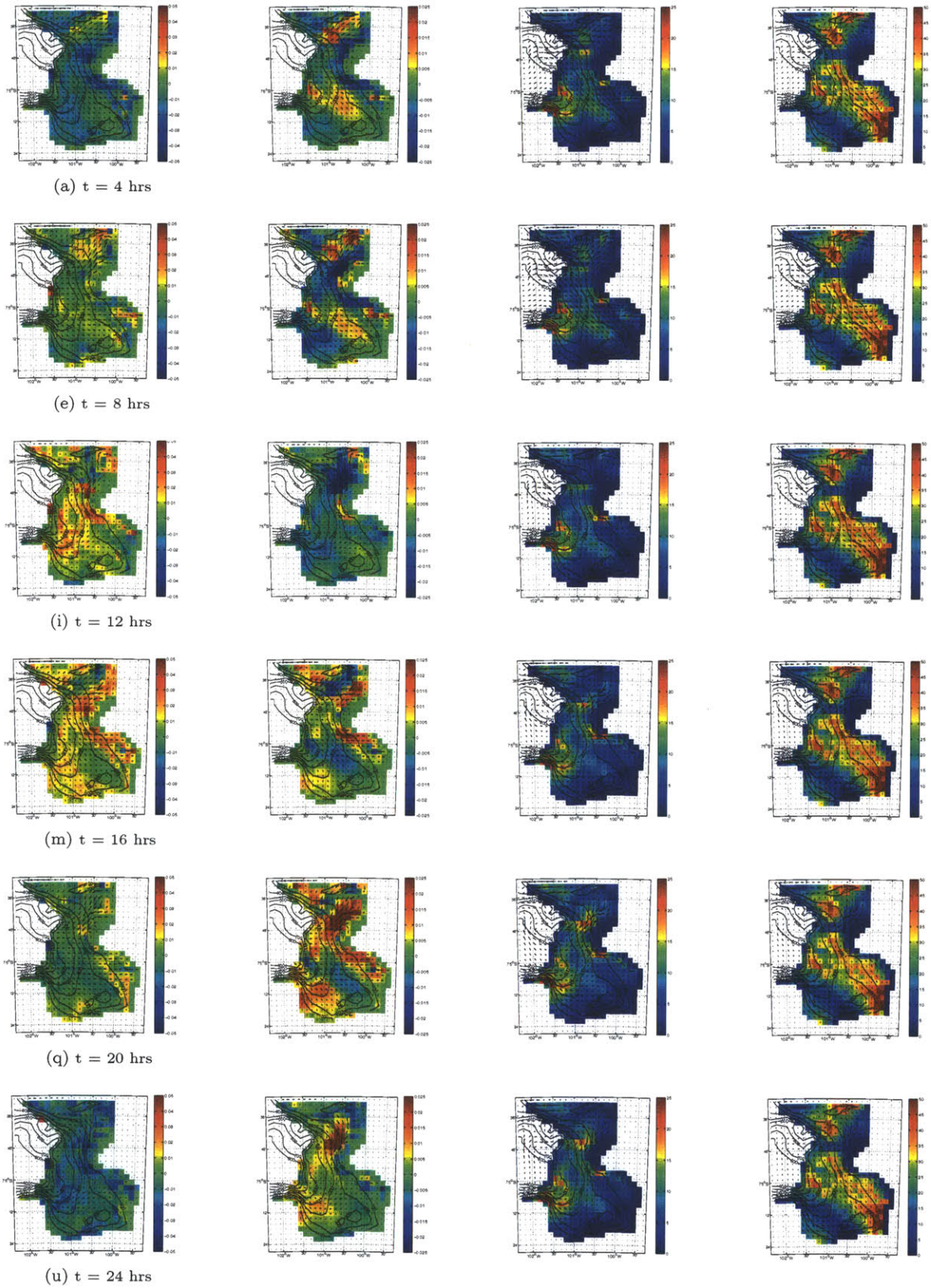

(a) t = 4 hrs

(e) t = 8 hrs

(i) t = 12 hrs

(m) t = 16 hrs

(q) t = 20 hrs

(u) t = 24 hrs

Figure 45: 4-hourly snapshots of the perturbed thermal forcing (first column), perturbed mixed layer velocity (second column), instantaneous velocity-dependent melt rates (third column) and instantaneous velocity-independent melt rates (fourth column) simulated with the realistic PIIS model forced with diurnal tides. The vectors superimposed on the perturbed field (first and second columns) indicate the direction and relative magnitude perturbed depth-integrated volume transport. The vectors superimposed on the melt rate fields (third and fourth columns) indicate the direction and relative magnitude of the time-averaged depth-integrated volume transport. Perturbed quantities are obtained by subtracting a 1-period average of a given field from its individual snapshots. Black contours on every panels show the distribution of water column thickness (m).

As in the idealized experiments, distortion of the melt rate signal and occurrence of multiple maxima in current velocity is predictable from the harmonic expansion of the momentum and mass balances. Frictional drag at both the ocean bottom and ice shelf base is still likely to be an important source of higher-frequency variability. A Fourier decomposition of the area-averaged and maximum melt rate signals shows peaks in melt rate amplitudes at frequencies of $\frac{n}{12\text{hours}}$ and $\frac{n}{24\text{hours}}$ with $n = 1, 2, 3, ...$ respectively for the semi-diurnal and diurnal tides experiments (see figure 46). Also as in the idealized experiments, because of the direct coupling with mixed layer velocities, the amplitude of the melt rate signals are overall higher in the velocity-dependent than in the velocity-independent experiments and decrease less rapidly with increasing frequency. Obviously, in a more realistic simulation including all eight dominant tidal components under PIIS, interactions between semi-diurnal and diurnal tidal signals with slightly different frequencies are expected to generate variability over a much wider range of frequencies. Moreover, interactions between the barotropic tidal currents and the steep ice shelf base and complex bedrock bathymetry are likely to general internal tides. Topographic Rossby waves and other rotational waves are also expected. However, analysis of time series of melt rates and tidal current sampled on intervals of much less than one hour would however be necessary to detect such high frequency waves and is beyond the scope of the present work.

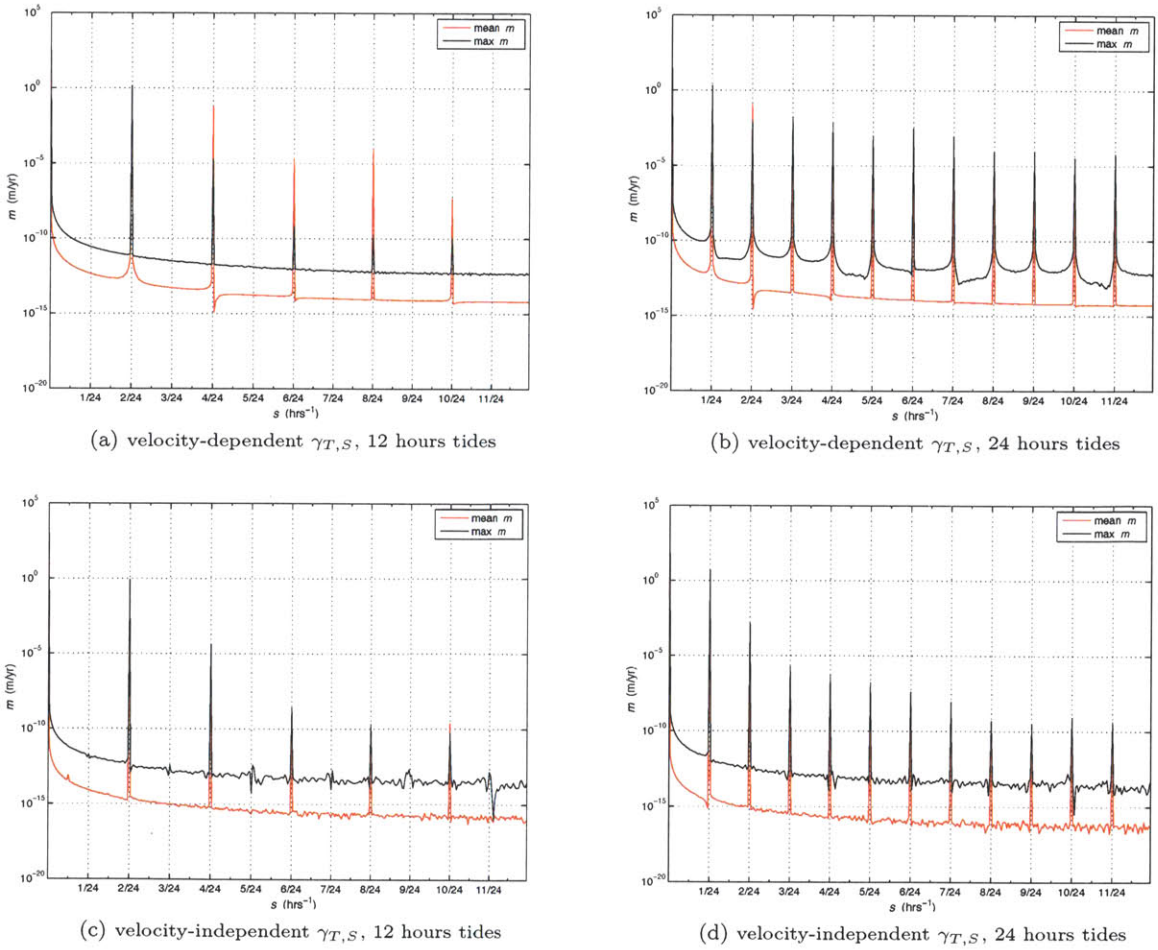

(a) velocity-dependent $\gamma_{T,S}$, 12 hours tides

(b) velocity-dependent $\gamma_{T,S}$, 24 hours tides

(c) velocity-independent $\gamma_{T,S}$, 12 hours tides

(d) velocity-independent $\gamma_{T,S}$, 24 hours tides

Figure 46: Periodogram of area-averaged (red curve) and maximum (black curve) melt rate time series in realistic simulations forced with a pure diurnal tidal current signal with amplitude of (a, d) 0.02 m/s (b, e) 0.2 m/s and (c, f) 0.4 m/s. The upper panels show results from velocity-dependent simulations and the lower panels, that of velocity-independent simulations.

The evolution of the melt rate, mixed layer velocity and thermal forcing suggests that the behavior of the velocity-dependent and velocity-independent models is overall consistent between the idealized and realistic setups. Most importantly, melt rate variability in the velocity-dependent simulations seems to be controlled by the evolution of mixed layer currents in both cases. In the velocity-independent experiments, the variability of melt rates mimics that of the thermal forcing. Velocity-dependent melt rates reach maximum values at the timing of maximum inflowing and outflowing tidal currents, while the velocity-independent melt rates are maximum and minimum at the end of the half period of inflowing and outflowing currents respectively. Fourier analysis of melt rate time series shows that the melt rate variability associated with the tidal forcing frequency is higher for the velocity-dependent formulation than for the velocity-independent formulation, in the idealized experiments. On the other hand, from the 2.5 days melt rate time series presented in figure 44 for the realistic simulations, it is not clear wether the velocity-dependent or the velocity-independent model shows the highest variability in melt rates. However, it is important to note that, as shown in section 4.2, the velocity-dependent model was identified to produce significantly lower melt rates than the velocity-independent model in the realistic PIIS setup when employing the default value of drag coefficient. Therefore, direct comparisons of the temporal variability of the melt rates between the velocity-dependent and velocity-independent realistic experiments is not straightforward. Nonetheless, it is clear in both the idealized and realistic experiments that the velocity-dependence induces a larger response of the melt rates to the generation of tidal power at higher frequencies by non-linear processes such as frictional drag and advection. It is therefore reasonable to expect velocity-dependent melt rates to respond more strongly to tidal forcing at its intrinsic frequency than velocity-independent melt rates in a realistic model that would be properly tuned with respect to the drag coefficient.

4.4.2 Modulating effects on the spatial distribution of the melt rates and the cavity circulation

In this section, we focus on the modulation of the time-independent melt rates and cavity circulation by tidal forcing. We start by identifying such modulations in both the idealized and realistic PIIS cavity setups and then try to associate them to processes by which tides are known to interact with the time-averaged cavity dynamics.

Idealized experiments

Comparison of forced and unforced simulations in the idealized setup indicates that tidal forcing does not alter the overall structure of the distribution of melting characteristic to the velocity-dependent and velocity-independent experiments, that is, maximum velocity-independent ablation rates over the northeastern corner of the cavity where warm inflow currents first reach the grounding line and high velocity-dependent ablation rates along the grounding line, path of the outflowing plume and over the southeastern interior portion of the cavity. Percentage differences in melting between forced and unforced simulations calculated as

$$\% = \frac{m_{tides} - m_{\ no\ tides}}{m_{\ no\ tides}} \cdot 100$$

however indicate a localized increase in melt rates at the ice shelf front (see figure 47), where melt rates are relatively low in the unforced simulations. In the velocity-dependent case, the increase is of about 50% (3-4 m/yr) for weak tidal currents ($|\hat{\mathbf{U}}_T| = 0.02$ m/s) and of more than 100% (> 10 m/yr) for strong tidal forcing ($|\hat{\mathbf{U}}_T| = 0.20$ m/s). In the velocity-independent case, the increase is smaller. It is of about 20% (1-2 m/yr) for $|\hat{\mathbf{U}}_T| = 0.02$ m/s and between 60% and 80% (5-10 m/yr) for $|\hat{\mathbf{U}}_T| = 0.20$ m/s. Another very concentrated region of increased melting is observed along the grounding line, where melt rates are relatively high in both the velocity-dependent and velocity-independent experiments.

In the velocity-dependent simulations, important accelerations in melting are also observed along the northern cavity wall. The increase is up to 50% (up to 2 m/yr) for $|\hat{\mathbf{U}}_T| = 0.02$ m/s and to 300% (20 to 40 m/yr) for $|\hat{\mathbf{U}}_T| = 0.20$ m/s. Moreover, the relative difference calculation also places a strong increase in melt rates over the northwestern corner of the cavity. However, observation of the actual melt rates over this region in the unforced simulations (figure 47a) indicates near-zero melting there and therefore suggests that it is an artifact of this type of calculation.

The idealized velocity-dependent experiments indicate that tidal forcing of realistic amplitude (0.02 m/s and 0.2 m/s) does not increase the maximum melt rates underneath the ice shelf. It does however increase the area-averaged melt rate and hence suggest an overall 'spreading' of intense melting areas underneath the ice shelf with the addition of tides. In the velocity-independent cases, no significant increase in both the maximum or average melt rate occurs. The localized increases in melt rates in these simulations are compensated for by a small decrease over most of the cavity interior. The response of the depth-integrated volume transport to tidal forcing is consistent with this behavior of the melt rates (figure 48). The increase in mean buoyancy fluxes with the amplitude of the tidal forcing in the velocity-dependent experiments strengthens the barotropic transport in the cavity. In the velocity-independent experiments, no significant increase in transport occurs. In both the velocity-dependent and velocity-independent cases however, the circulation on the cavity side of the ice shelf front becomes more meridional as tidal forcing is increased. Everywhere else in the cavity, the structure of the circulation is unaffected by the inclusion of tides. Figures 47 and 48 show only the outputs of simulations forced with diurnal tides, but the results are similar, both in amplitude and spatial distribution, in the case of semi-diurnal tides.

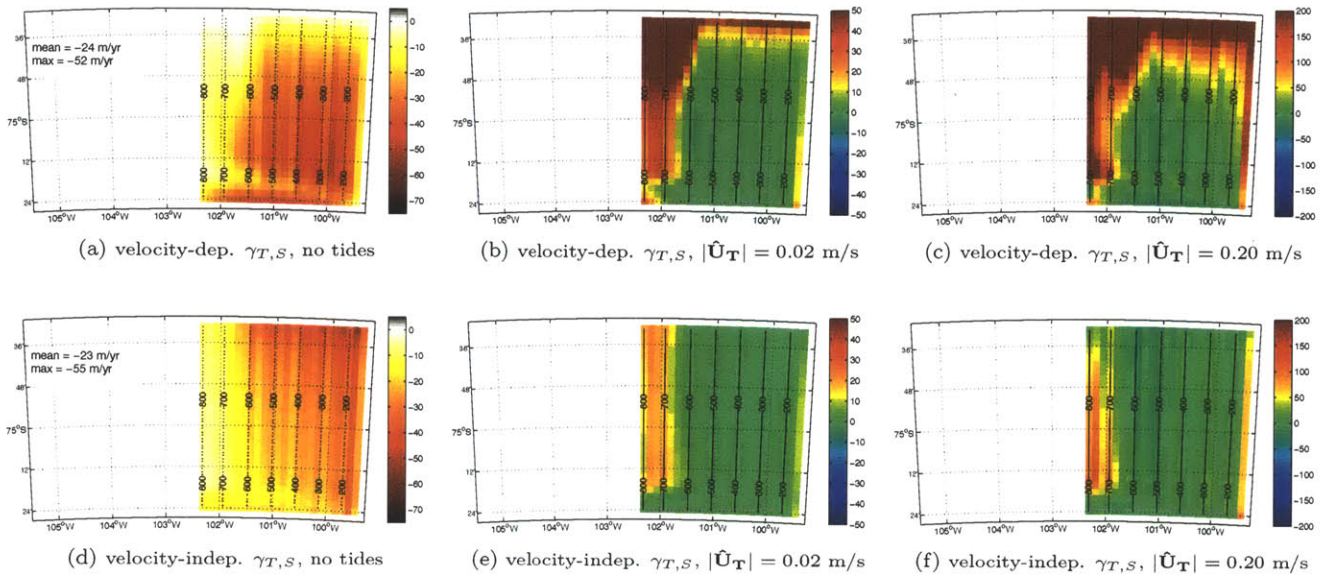

(a) velocity-dep. $\gamma_{T,S}$, no tides (b) velocity-dep. $\gamma_{T,S}$, $|\hat{\mathbf{U}}_\mathbf{T}| = 0.02$ m/s (c) velocity-dep. $\gamma_{T,S}$, $|\hat{\mathbf{U}}_\mathbf{T}| = 0.20$ m/s

(d) velocity-indep. $\gamma_{T,S}$, no tides (e) velocity-indep. $\gamma_{T,S}$, $|\hat{\mathbf{U}}_\mathbf{T}| = 0.02$ m/s (f) velocity-indep. $\gamma_{T,S}$, $|\hat{\mathbf{U}}_\mathbf{T}| = 0.20$ m/s

Figure 47: a, d : Melt rates (m/yr) simulated with the idealized (a) velocity-dependent and (d) the velocity-independent model without tidal forcing. The maximum and area-averaged melt rate are indicated in the top left corner of each figure. b, c, e, f : Relative difference (%) between the distribution of velocity-dependent melt rates simulated with and without tidal forcing, for tidal currents with (b) $|\hat{\mathbf{U}}_\mathbf{T}| = 0.02$ m/s and (c) $|\hat{\mathbf{U}}_\mathbf{T}| = 0.20$ m/s. Relative difference (%) between the distribution of velocity-independent melt rates simulated with and without tidal forcing, for tidal currents with (e) $|\hat{\mathbf{U}}_\mathbf{T}| = 0.02$ m/s and (f) $|\hat{\mathbf{U}}_\mathbf{T}| = 0.20$ m/s.

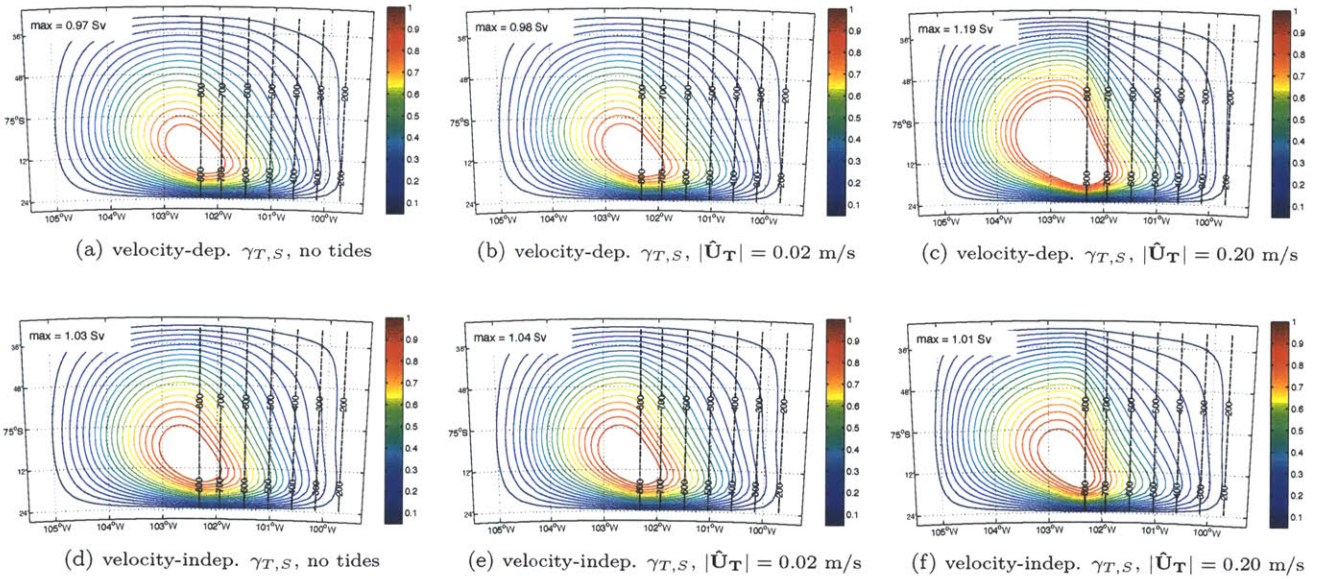

(a) velocity-dep. $\gamma_{T,S}$, no tides (b) velocity-dep. $\gamma_{T,S}$, $|\hat{\mathbf{U}}_\mathbf{T}| = 0.02$ m/s (c) velocity-dep. $\gamma_{T,S}$, $|\hat{\mathbf{U}}_\mathbf{T}| = 0.20$ m/s

(d) velocity-indep. $\gamma_{T,S}$, no tides (e) velocity-indep. $\gamma_{T,S}$, $|\hat{\mathbf{U}}_\mathbf{T}| = 0.02$ m/s (f) velocity-indep. $\gamma_{T,S}$, $|\hat{\mathbf{U}}_\mathbf{T}| = 0.20$ m/s

Figure 48: a, b, c: Barotropic streamfunction of the vertically integrated volume transport (Sv) for idealized velocity-dependent simulations using (a) no tidal forcing, (b) tidal current forcing with $|\hat{\mathbf{U}}_\mathbf{T}| = 0.02$ m/s, (c) tidal current forcing with $|\hat{\mathbf{U}}_\mathbf{T}| = 0.20$ m/s. d, e, f: Barotropic streamfunction of the vertically integrated volume transport (Sv) for idealized velocity-independent simulations using (a) no tidal forcing, (b) tidal current forcing with $|\hat{\mathbf{U}}_\mathbf{T}| = 0.02$ m/s, (c) tidal current forcing with $|\hat{\mathbf{U}}_\mathbf{T}| = 0.20$ m/s. Dashed contours show the distribution of water column thickness (m) underneath the ice shelf. The maximum value of barotropic transport is indicated in the top left corner of each figure.

Realistic experiments

As in the idealized experiments, inclusion of a tidal forcing does not change the overall spatial pattern of melting, which is characterized by local maxima over fast outflow plumes in the velocity-dependent simulations and by a broad maxima over the region of highest thermal forcing in the velocity-independent simulations. Relative differences in melt rates between the forced and unforced simulations again indicate an acceleration of melting along the ice shelf front (see figure 49). For the semi-diurnal and diurnal tidal signals, the acceleration reaches 100% there, which corresponds to an augmentation of 2 to 6 m/yr. The increase is comparably not as important in the velocity-independent experiments. Another area of strong velocity-dependent melt rate increase is seen over the northeastern shallow portion of the cavity. This increase does not occur in the velocity-independent experiments.

Other strong, localized relative melt rate increases are seen in all experiments over the shallow northwestern portion of the cavity, over very restricted regions along the grounding lines and over a small plateau at the southern end of the cavity where water column thickness diminishes to 50 meters. However, actual melt rates over most of these areas are very small in both the unforced and forced simulations. The strong melt rate increase signals there do not contribute significantly to the cavity-averaged ablation rates and should be treated with care as they could be artifacts of the relative difference calculation.

The increase in area-averaged melt rates associated with the introduction of tides is very small. Hence, the localized strong accelerations in melting are almost compensated for over broader regions of weak decrease in ablation rates. The increase in melt rates is of about 1 m/yr in both the velocity-dependent and the velocity-independent experiments. Hence it is relatively much weaker in the velocity-independent cases, since unforced mean melt rates are about four times stronger in these simulations than in the unforced velocity-dependent simulations (see figures 49a and 49c). As in the idealized experiments, the melt rate therefore seems to respond more strongly to tidal forcing in the velocity-dependent than in the velocity-independent model. In terms of overall structure and magnitudes of melt rates, our results are consistent with a recent modeling study by Makinson et al. (2011). They noticed that while the pattern of melting remained relatively unchanged, the magnitude of ablation rates increased when including tides in their realistic model of FRIS. The increases in melt rate magnitude we simulate for PIIS are not nearly as strong as those obtained by Makinson et al. (2011) for FRIS however. This is probably due to the fact that tidal currents under PIIS are comparatively much weaker than that under FRIS.

The most prominent change in barotropic volume transport in both the velocity-dependent and velocity-independent cases occurs along the ice shelf front. There, the cyclonic gyre that dominates the cavity circulation under PIIS proper stretches northward along the ice shelf edge, such that streamlines that cross the ice shelf front in the unforced experiments run parallel to it when tidal forcing is included in the model. This is likely to isolate the circulation in the cavity and limit its sensitivity to changes in open ocean properties over the continental shelf. Also, the anticyclonic circulation covering the northern part of the open ocean in front of the ice shelf shrinks as the cyclonic gyre extends northward. Over the major part of the cavity, the circulation seems unaffected in both structure and intensity by the inclusion of a tidal forcing in the model.

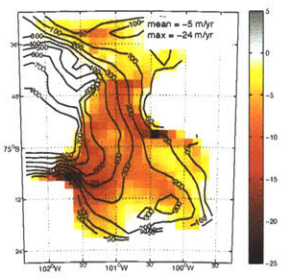

(a) velocity-dep. $\gamma_{T,S}$, no tides

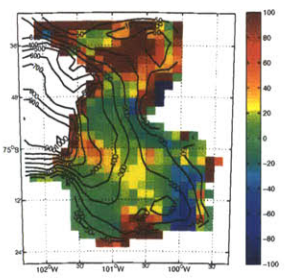

(b) velocity-dep. $\gamma_{T,S}$, 12 hrs tides

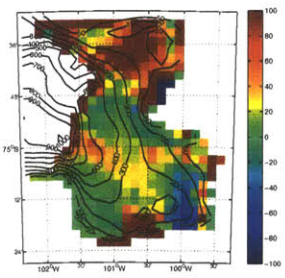

(c) velocity-dep. $\gamma_{T,S}$, 24 hrs tides

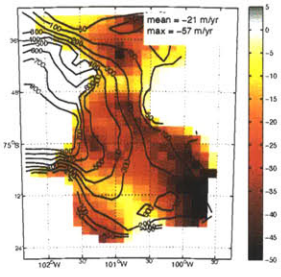

(d) velocity-indep. $\gamma_{T,S}$, no tides

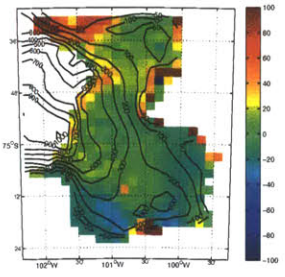

(e) velocity-indep. $\gamma_{T,S}$, 12 hrs tides

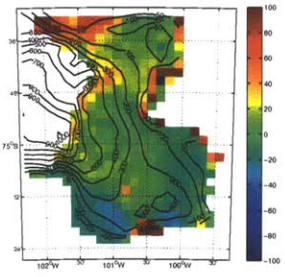

(f) velocity-indep. $\gamma_{T,S}$, 24 hrs tides

Figure 49: a, d : Melt rates (m/yr) simulated with the the realistic PIIS (a) velocity-dependent and (d) velocity-independent models without tidal forcing. b, c, e, f : Relative difference (%) between the distribution of velocity-dependent melt rates simulated with and without tidal forcing, for (b) semi-diurnal and (c) diurnal tidal currents. Relative difference (%) between the distribution of velocity-independent melt rates calculated with and without tidal forcing, for (e) semi-diurnal and (f) diurnal tidal currents.

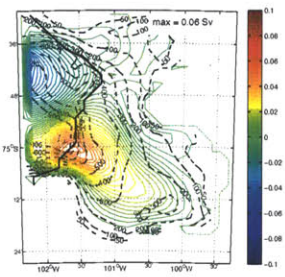

(a) velocity-dep. $\gamma_{T,S}$, no tides

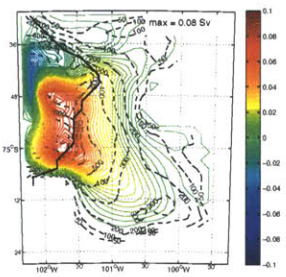

(b) velocity-dep. $\gamma_{T,S}$, 12 hrs tides

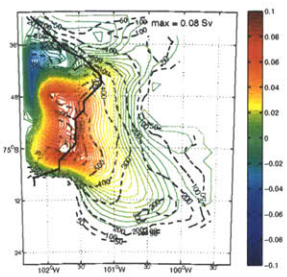

(c) velocity-dep. $\gamma_{T,S}$, 24 hrs tides

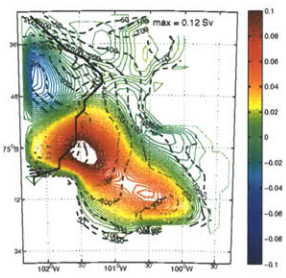

(d) velocity-indep. $\gamma_{T,S}$, no tides

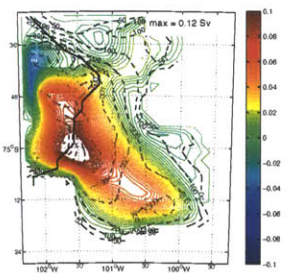

(e) velocity-indep. $\gamma_{T,S}$, 12 hrs tides

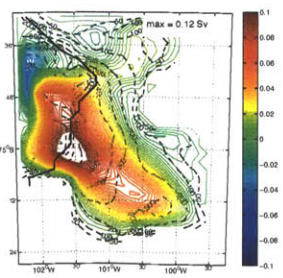

(f) velocity-indep. $\gamma_{T,S}$, 24 hrs tides

Figure 50: a, b, c: Barotropic streamfunction of the vertically integrated volume transport (Sv) for idealized velocity-dependent simulations using (a) no tidal forcing, (b) semi-diurnal and (c) diurnal tidal forcing. d, e, f: Similar barotropic streamfunction of the vertically integrated volume transport (Sv) for idealized velocity-independent simulations. Dashed contours show the distribution of water column thickness (m) underneath the ice shelf and the plain black contour, the location of the ice shelf front.

The next two sections describe further the processes by which tides may interact with the time-independent components of the barotropic and thermohaline circulation under PIIS and cause the changes in circulation and ablation rates we identified above. The strengthening in both circulation and melt rates at the ice shelf front points to the generation of tidally rectified currents there. The increased melting over shallow areas and along the cavity edges and the grounding is likely attributable to strong mixing induced by the oscillating tidal currents. In the following, we elaborate on the possibility of the occurrence of such processes, particularly under PIIS, but also under 'warm' ice shelves with similar hydrographic and tidal forcing conditions.

4.4.3 Tidal rectification

Because of the sharp jump in water column thickness, ice shelf fronts are likely locations for the generation of tidally rectified flows. According to equation (23) and the barotropic model developed in the theory section, tidally rectified flows should run parallel to isobaths or water column thickness contours, with shallow depths to the left in the Southern Hemisphere. The streamfunctions in figure 48 and 50 for the depth-integrated and time-averaged horizontal volume transport already indicate that this is the case along the ice shelf edge of PIIS. Melt rates along the ice front increase significantly in response to the strengthening of the barotropic circulation in the velocity-dependent simulations. As expected, the increase is comparatively not as important in the velocity-independent experiments (see figure 49). Moreover, the circulation in the vicinity of the ice shelf edge increases much more in response to the addition of tidal forcing in the velocity-dependent than in the velocity-independent simulations. Figure 50 indicates an increase in maximum barotropic volume transport from 0.6 Sv to 0.8 Sv between the unforced and forced velocity-dependent experiments and no change in volume transport in the velocity-independent cases. This suggests that a positive feedback operates between the strengthened currents and intensified buoyancy fluxes at the ice shelf front.

According to equation (23), tidal rectification is expected over areas of strong tidal currents, shallow water column thickness and/or strong water column thickness gradients. A scan for areas under PIIS which meet one or more of these criteria points out to the northeastern corner of the cavity, where water column thickness is of about 100 meters only and tidal currents are strong (see figure 51a). A large increase in velocity-dependent melt rates is seen over this region when including tides (figure 49, upper panels). Comparison of the time-average depth-integrated flow in the unforced experiment (figure 51a) and tidally forced experiments (figure 51b) shows an amplification of the time-independent flow, but only along the eastern cavity wall. The increase in melt rate observed over the interior portion of the northern cavity must therefore be associated with another process such as mixing. Along the eastern cavity wall, vectors of the time-averaged flow indicate that the currents mostly follow contours of water column thickness, with the steep cavity wall (shallow water) to the left, consistently with tidal rectification dynamics. A similar scenario is seen over the plume outflow along the steeply sloping west cavity wall of PIIS proper[19]. It is hence likely that tidal rectification locally intensifies the time-independent flow along the very steep cavity walls of PIIS.

Another area where one could expect non-linear interactions with the oscillating flow and topography to occur underneath PIIS is around the sill in the southern portion of the cavity. Time-independent anticyclonic circulations around sills have noticed notably in the modeling study of (MacAyeal, 1984c) for Ross Ice Shelf. However, comparison of figures 51a and 51b suggests that tides do not induce an intensification of the time-independent flow around the sill of PIIS. This is likely attributable to the relatively large scale of the sill and weak tidal currents there. Zimmerman (1981) and Robinson (1981) have proposed a scaling law to estimate

[19] although the intensification in time-independent barotropic flow and the increase in melting there are relatively weak, as this is already a region of strong flows and fast melting

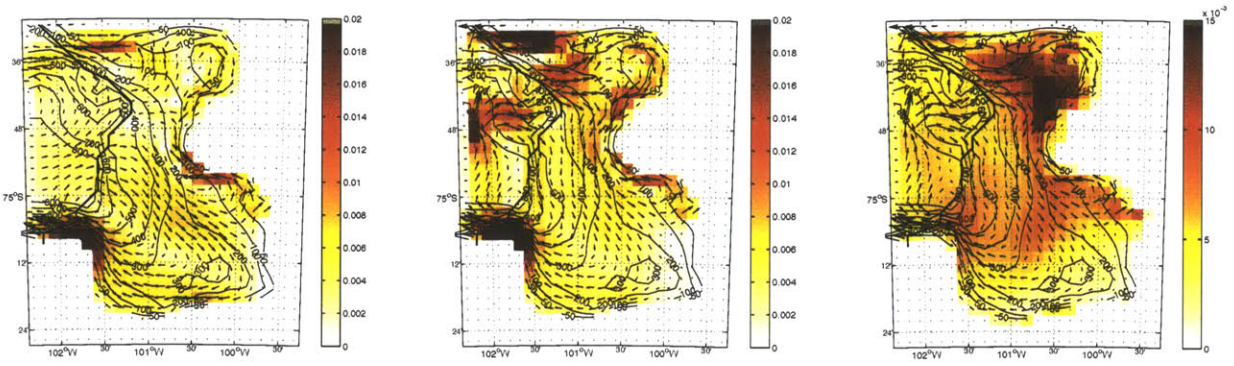

(a) t-averaged flow, no tides (b) t-averaged flow, with tides (c) tidal flow, with tides

Figure 51: Time-independent depth-integrated volume transport underneath PIIS for (a) an unforced simulation (b) a simulation forced with diurnal tides of realistic amplitude, calculated by averaging instantaneous fields over one tidal period. The shading gives the magnitude (Sv) of the time-independent transport and vectors indicate the relative magnitude and direction of the transport. (c) Time-dependent and depth-integrated volume transport calculated for the same simulation forced with diurnal tides of realistic amplitude. The shading shows the magnitude of the time-dependent transport calculated by averaging the magnitude of instantaneous transport fields and vectors indicate again the relative magnitude and direction of the time-dependent transport.

the amplitude of the tidally-rectified flow around topographic features, which compares the length of tidal excursion l, defined as

$$l = \frac{|\hat{\mathbf{U}}_\mathbf{T}|}{\omega},$$

with ω, the (actual, i.e., non-angular) frequency of the given tidal component with amplitude $|\hat{\mathbf{U}}_\mathbf{T}|$, and L, the topographic length scale (the width of the sill here). For a ratio

$$\lambda = \frac{l}{L} \tag{40}$$

that is O(1), resonance increases the efficiency of the transfer of energy from the tidal component to the time-independent component of the flow. This efficiency decreases rapidly for both larger and smaller values of λ. In the case of the sill of PIIS, λ it is at most[20]

$$\lambda \approx \frac{0.02 \text{ ms}^{-1}}{\omega \cdot 40 \cdot 10^3 \text{ m}},$$

hence of $O(10^{-2})$ for both diurnal and semi-diurnal tides. Thus a resonant response of the model to tidal currents around the sill is not expected. The actual magnitude of the tidally-rectified currents about a given topographic feature can be estimated in terms of its horizontal and vertical extent and of the tidal excursion, according to the following expression derived by Zimmerman (1978):

$$|\bar{\mathbf{U}}| = \frac{H}{h}|\hat{\mathbf{U}}_\mathbf{T}| \; g(\lambda)$$

where h is the background water column depth, H, the height of the topographic feature, and $g(\lambda)$ is a

[20]Here we approximate the local amplitude of the tidal currents under PIIS by the amplitude of the prescribed tidal forcing. As indicated in figure 51c, the amplitude of tidal currents in the vicinity of the sill of PIIS is about equal or lower than that of the forcing. Hence our calculation of λ can be considered as an upper bound estimate.

statistically-derived weighting function representative of the decay of tidally-rectified currents for both $\lambda > O(1)$ and $\lambda < O(1)$. The specific form of $g(\lambda)$ depends notably on the parameterization of the Coriolis term and ocean bottom drag. In the case of large topographic length scale ($\lambda \to \infty$), this expression predicts that the amplitude of the tidally rectified flow $|\bar{\mathbf{U}}|$ varies as

$$|\bar{\mathbf{U}}| \propto |\hat{\mathbf{U}}_\mathbf{T}|^2 \frac{H}{hL},$$

Hence, one can expect λ to increase towards $O(1)$ as the square of $|\hat{\mathbf{U}}_\mathbf{T}|$, i.e., rapidly with the amplitude of the tidal currents. However, the actual response of the model to an increase in tidal forcing in terms of the magnitude of the tidally-rectified current is not assessed straightforwardly as it depends critically on the form of the weighting function.

Zimmerman (1978) derived the function $g(\lambda)$ in the simple case of a constant density fluid and a linear drag parameterization. The derivation of $g(\lambda)$ in the case of a quadratic ice shelf base and bottom drag is complex and beyond the scope of the present work. Hence, to estimate the strength of the tidal current (i.e., the amplitude of of tidal excursion l) that would be required to support tidal rectification around the sill of PIIS, we adopt a 'detour' idealized approach which consists in placing a horizontally symmetric sill of fixed width L in the idealized cavity setup. We also add an inverted sill or 'through' downstream of the sill to represent the depression in bedrock separating the sill under PIIS from the grounding line (see figure 52). The through and sill are exactly symmetric and have a height of 300 meters and horizontal extent L of about 40 km (10 grid cells). The dimensions are chosen so that to be consistent with the height and length scales of the bathymetric features under PIIS. The amplitude of the prescribed tidal forcing is varied between $|\hat{\mathbf{U}}_\mathbf{T}| = 0.02$ m/s, which is comparable to the amplitude of tidal currents under PIIS, $|\hat{\mathbf{U}}_\mathbf{T}| = 0.20$ m/s, in the range of strong tidal forcing in ice shelf cavities (Holland and Jenkins, 1999; Holland, 2008; Mueller et al., 2012) and $|\hat{\mathbf{U}}_\mathbf{T}| = 0.40$ m/s, which should be an upper bound to this range. Figures 53 and 54 show results of simulations forced with diurnal tidal currents. Very similar results are obtained when using semi-diurnal currents, although the tidal rectification signal is slightly weaker in this case, as expected form equation 40.

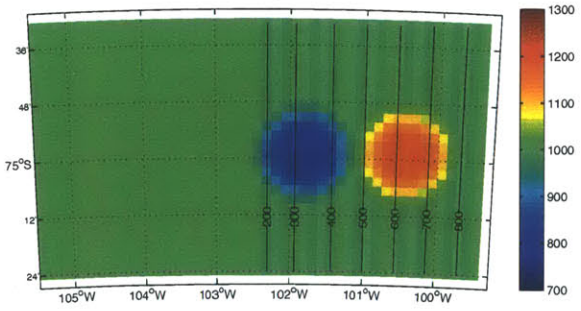

Figure 52: (a) Geometry of the idealized cavity including a sill and inverted sill. Shading indicates the depth of the ocean bottom (m) and contours, the position of the ice shelf base depth (m).

Figure 53 compares the magnitude and direction of the depth-integrated time-independent currents in unforced simulations (figure 53a) and in simulations forced with tidal currents (figure 53b, 53c, 53d). For prescribed currents on the order of magnitude of the actual depth-integrated tidal currents under PIIS ($|\hat{\mathbf{U}}_\mathbf{T}| =$ 0.02 m/s, figure 53b), no change is seen in the direction of the mean flow in the forced simulations with respect to the unforced one. Relative differences in the magnitude of the flow are of maximum 10% in the vicinity of the sill and well below 10% over most of the domain. The strength and spatial distribution of melt rates also appear

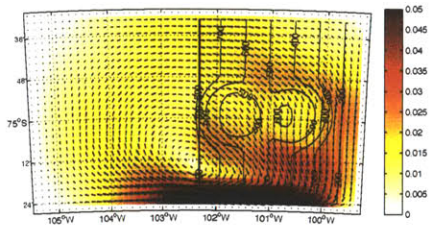

(a) no tides

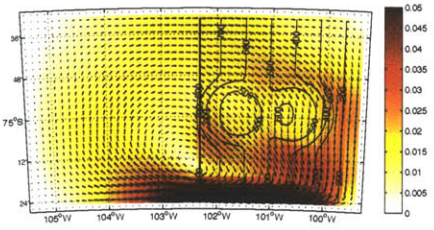

(b) $|\hat{\mathbf{U}}_\mathbf{T}| = 0.02$ m/s

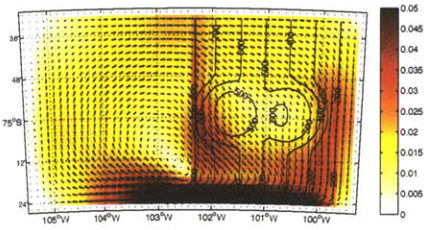

(c) $|\hat{\mathbf{U}}_\mathbf{T}| = 0.20$ m/s

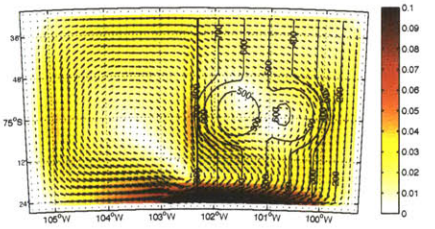

(d) $|\hat{\mathbf{U}}_\mathbf{T}| = 0.40$ m/s

Figure 53: Time-independent depth-integrated volume transport underneath PIIS for (a) an unforced simulation and simulations forced with diurnal tides with (b) $|\hat{\mathbf{U}}_\mathbf{T}| = 0.02$ m/s, (c) $|\hat{\mathbf{U}}_\mathbf{T}| = 0.20$ m/s and (d) $|\hat{\mathbf{U}}_\mathbf{T}| = 0.40$ m/s, calculated by averaging instantaneous fields over one tidal period. The shading gives the magnitude of the time-independent transport (Sv) and vectors indicate the relative magnitude and direction of the transport. Dotted black lines are contours of water column thickness. The thick solid line indicates the position of the ice shelf front.

unaffected by the introduction of tides of such amplitude (figure 54b). For forcing of one order of magnitude higher than the depth-integrated tidal signal under PIIS ($|\hat{\mathbf{U}}_\mathbf{T}| = 0.2$ m/s), λ is of order $O(10^{-1})$ for diurnal and semi-diurnal tides. The inflow doubles in front (west) of the sill, decreases by about 40% over the sill/through and increases by about 25% downstream (east) of the through (figure 53c). Along the upstream flank of the sill, the time-independent flow becomes more meridional, such that it approximately follows contours of water column thickness. The change in current orientation is however very small and so are changes in the melt rate distribution in the vicinity of the bathymetric features (figure 54c). In order to obtain closed anticyclonic and cyclonic circulations about the sill and trough expected from tidal rectification theory, tidal forcing must be more than doubled. For the case of $|\hat{\mathbf{U}}_\mathbf{T}| = 0.40$ m/s, λ is of about 0.9 and 0.45 for 24 hours and 12 hours tides respectively. For diurnal tides, merely closed ocean circulations are observed (see figure 53d), with two centers of very weak currents located approximately over the two bathymetric features. This is not yet the case for semi-diurnal tides (not shown). Under such strong thermal forcing, melt rates increase substantially over the northeastern corner of the cavity, as warm currents entering the cavity are redirected there when encountering the steep bedrock topography. This signal dominates over any other melt rate amplification signal associated with the tidally-rectified currents around the sill and trough. A much enlarged domain would be necessary for these weaker signals to be observed clearly, but from the formulation of the velocity-dependent melt rates and equation (23) for the tidaly-rectified flow, one would simply expect increases in melt rates around the bathymetric features, with the fastest melting concentrated along the steepest portion of the slopes, where time-independent currents should be the strongest. Obviously, velocity-independent melt rates do not respond to the reinforcement of the barotropic circulation around topographic features (not shown).

The idealized experiments performed here therefore suggest that area-averaged tidal currents of one order of magnitude higher than that expected beneath PIIS are necessary for tide-topography interactions to have a significant effect on the time-independent circulation and melt rates. Such high tidal currents are more typical of cold ice shelves, for instance, of Ross Ice Shelf, for which simulations by MacAyeal (1984c) actually predict

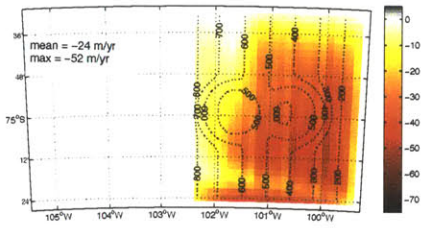

(a) no tides

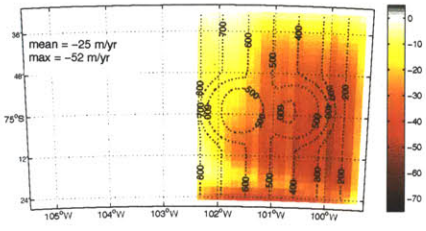

(b) $|\hat{\mathbf{U}}_\mathbf{T}| = 0.02$ m/s

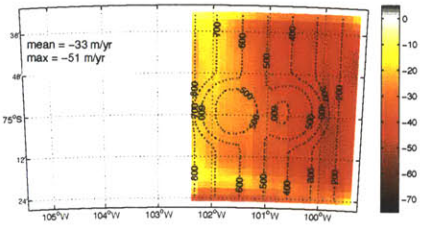

(c) $|\hat{\mathbf{U}}_\mathbf{T}| = 0.20$ m/s

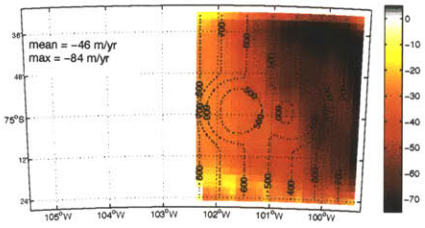

(d) $|\hat{\mathbf{U}}_\mathbf{T}| = 0.40$ m/s

Figure 54: Time-independent melt rates underneath PIIS for (a) an unforced simulation and simulations forced with diurnal tides with (b) $|\hat{\mathbf{U}}_\mathbf{T}| = 0.02$ m/s, (c) $|\hat{\mathbf{U}}_\mathbf{T}| = 0.20$ m/s and (d) $|\hat{\mathbf{U}}_\mathbf{T}| = 0.40$ m/s, calculated by averaging instantaneous ablation fields over one tidal period. Dotted black lines are contours of water column thickness. The mean and maximum melt rates are indicated in the top left corner of each figure.

the presence of tidally rectified currents along a large sill. Mean tidal current amplitudes beyond the range of area-averaged values reported for ice shelf cavities would be required for a clear signature of tidal rectification around bathymetric features with scales comparable to that of the sill of PIIS.

Conversely, another set of simulations could be added to the present analysis in which the tidal amplitude, i.e., the tidal excursion, would be fixed to the realistic values predicted for PIIS but the length L of the sill and trough would be reduced, so that to allow identifying the horizontal scale of topographic features around which one should expect the presence of tidally-rectified flows under PIIS. This is not done here. However, in the meantime, the experiments we conducted indicate that tidal rectification occurs along very steep bathymetric features under PIIS such as the ice shelf edge and portions of the grounding line and cavity walls.

4.4.4 Tidal mixing fronts

A recent study by Holland (2008) questioned the role previously attributed to tidal mixing as an important driver of the thermohaline circulation beneath ice shelves by demonstrating that the extent of the mixing associated with tidally-induced turbulence is limited under most realistic ice shelf cavity conditions. In particular, Holland (2008) hypothesized that tidal front formation should be negligible in 'warm' ice shelf cavities, because of their high melt rates and relatively low tidal currents. In the following, we verify the conjecture of Holland (2008) and evaluate the possibility of the formation of a stable tidal front, first underneath an idealized 'warm' ice shelf and second, in a more realistic PIIS cavity.

To do so, we apply the method of MacAyeal (1984a) which consists in estimating the maximum melt rate for which maintaining de-stratification is possible and comparing it to the simulated melt rate. As the present model includes an ocean stratification, the maximum or 'critical' melt rate defined in equation (30) can only be an approximation here. To verify its validity, we perform two different calculations of m_{max}. First, we use the depth integrated tidal currents and the sum of the bottom and ice shelf base coefficient for C_d in equation (30). We refer to this approach as the 'barotropic' method. Second, we calculate the turbulent tidal power as the sum of a contribution from friction underneath the ice shelf and from friction at the bedrock such that the expression for the critical melt rate becomes

$$m_{max} = \frac{2\alpha(C_{dM}|\hat{\mathbf{U}}_\mathbf{M}|\hat{\mathbf{U}}_\mathbf{M} \cdot \hat{\mathbf{U}}_\mathbf{M} + C_{dB}|\hat{\mathbf{U}}_\mathbf{B}|\hat{\mathbf{U}}_\mathbf{B} \cdot \hat{\mathbf{U}}_\mathbf{B})}{\beta S g h} \tag{41}$$

where C_{dM} is the drag coefficient at the ice shelf base, C_{dB} is the drag coefficient at the ocean bottom ($2.5 \cdot 10^{-3}$ in all simulations), $\hat{U}_M$ is the mixed-layer averaged tidal current, which contributes directly to frictional dissipation at the ice shelf base in the baroclinic model, and $\hat{U}_B$ is the tidal current in the deepest layer which is associated with frictional dissipation in the bottom boundary layer. This calculation is referred to as the 'baroclinic' method. For both methods, instantaneous tidal velocities are calculated by subtracting a one period-average to the ocean currents simulated following the three years spinup. In both methods, salinity in equations 30 and 41 is approximated by the depth-averaged salinity. Since S varies very little underneath the ice shelf, the specific value chosen here is actually not critical. The constant haline contraction coefficient β is of $8.0 \cdot 10^{-4}$ psu^{-1} and the acceleration due to gravity, g, is 9.81 ms^{-2}. h is the field of water column thickness and is the same in both methods. Following Holland (2008), the default efficiency coefficient used here is of 0.75%.

The spatial distributions of critical melt rate and actual melt rate magnitudes calculated using the barotropic and the baroclinic approaches described above are shown in figures 55 and 56 respectively. In these experiments, the cavity is forced with a pure diurnal tidal signal with amplitude of 0.2 m/s. Left panels show the results of velocity-dependent and right panels, the results of velocity-independent simulations. In all cases, local critical melt rates stay below 1 m/yr. The values of m_{max} calculated using the baroclinic approach are in good agreement with that obtained by Holland (2008) for comparable tidal current amplitude. The values calculated using the barotropic calculation are about five times lower than that obtained with the baroclinic method (note the different color scales) and therefore probably underestimate the critical melt rates. This is as expected since vertical profiles of ocean currents underneath the ice shelf show considerable shear. Notable differences also occur in the spatial distribution of m_{max} between the two calculations. The barotropic approach places the highest critical melt rates along the grounding line and indicates very low values of m_{max} everywhere else. Because C_d is larger at the ice shelf base than at the ocean bottom and $|\hat{U_M}|$ is about O(1) larger than $|\hat{U_B}|$, i.e., currents are much faster in the mixed layer underneath the ice shelf than in the bottom boundary layer,

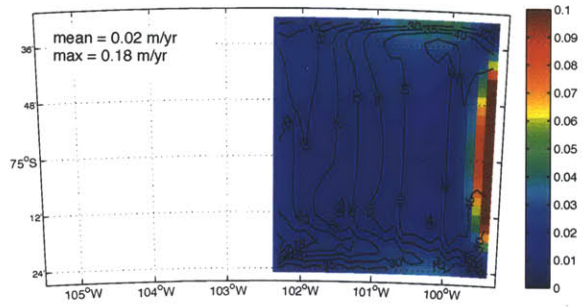

(a) velocity-dependent $\gamma_{T,S}$, $U_T = 0.2$ ms^{-1}

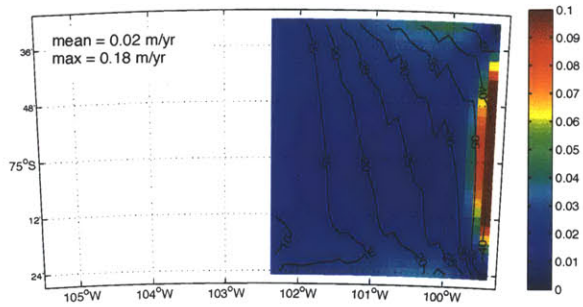

(b) velocity-independent $\gamma_{T,S}$, $U_T = 0.2$ ms^{-1}

Figure 55: Critical melt rate calculated using the barotropic approach and equation 30, underneath the idealized ice shelf in a (a) velocity-dependent and (b) velocity-independent experiment forced with diurnal tides with amplitude of $U_T = 0.2$ ms^{-1}.

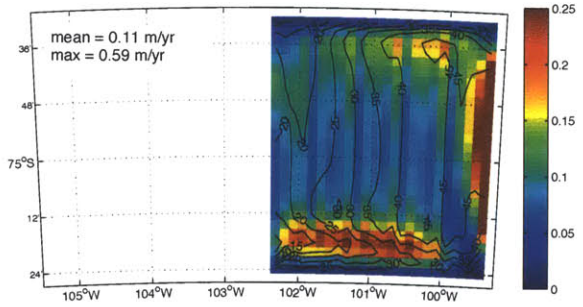

(a) velocity-dependent $\gamma_{T,S}$, $U_T = 0.2$ ms^{-1}

(b) velocity-independent $\gamma_{T,S}$, $U_T = 0.2$ ms^{-1}

Figure 56: Critical melt rate calculated using the baroclinic approach and equation 41, underneath the idealized ice shelf in a (a) velocity-dependent and (b) velocity-independent experiment forced with diurnal tides with amplitude of $U_T = 0.2$ ms^{-1}.

the spatial pattern of m_{max} obtained with the baroclinic approach mimics more closely the distribution of mixed layer velocity. A local maximum in m_{max} is associated with the strong mixed layer currents over the plume outflow region. Another is located along the northern boundary, coincidently with the inflow branch of the depth-integrated cavity circulation. The absolute maximum is observed along the grounding line, where the water column is the shallowest and mixed layer currents are fast between the region of warm inflow to the north and plume outflow to the south. Because the barotropic method is probably inappropriate in the present baroclinic model, only the baroclinic approach is used to calculate m_{max} in the following.

The differences in critical melt rate patterns between the two approaches are actually irrelevant in the present idealized simulations, as they both produce m_{max} values that are everywhere much smaller than the actual melt rates. This is true for all efficiency coefficient α in the range of values used in tidal front modeling studies (Holland, 2008). Simulations forced with pure semi-diurnal tidal signals of same amplitude produce very similar patterns of critical melt rates but even lower values of m_{max} (results not shown). Therefore, tidal front formation is not expected under this idealized 'warm' ice shelf for tidal forcing of this magnitude.

As predicted from theory (equation 41), critical melt rates increase with the amplitude of tidal currents. The theoretical dependence of m_{max} and of the actual melt rates on the magnitude of tidal currents predicts

that m_{max} increases faster than m with $|\hat{U_T}|$. However, tidal currents of 0.4 m/s, i.e., in the very high range of tidal forcing in ice shelf cavities (Holland and Jenkins, 1999; Holland, 2008), are not strong enough for m_{max} to become nearly comparable to the actual melt rates in the present simulations[21]. This is also true when varying the drag coefficient at the ice shelf base and/or at the ocean bottom. The area-averaged m_{max} increases linearly with C_d (or $C_{dM} + C_{dB}$), and as identified in section 4.2, the actual melt rate increases in a sub-linear manner with C_d. However, over the range of drag coefficients investigated here (1/16 to 16 times the 'default' value proposed by Holland and Jenkins (1999)), the increase in m_{max} is not sufficient to match the melt rates.

Both the patterns and area-averaged magnitudes of m_{max} are very similar in the velocity-dependent and independent experiments. This indicates that tidal currents are similar in both structure and strength between the two types of simulations, hence that there are no significant feedbacks on tidal currents induced by the velocity-dependence of the melt rate, as expected for the short time scale of the tidal forcing. This similarity in the distribution of m_{max} is particularly interesting, since actual melt rate patterns differ largely between the two melt rate formulations. For 'cold' ice shelves that support tidal fronts, one can therefore expect important differences in the distribution of tidal mixing when employing a velocity-dependent vs a velocity-independent parameterization of the ablation rates. In the velocity-dependent experiments, high melt rates are collocated with areas of strong mixed layer flow along the grounding line and over the plume outflow. Therefore, even if these regions are also the location of local maxima in critical melt rates, the production of large volumes of meltwater there is likely to keep the water column stratified. This parameterization however does not place high melt rates over the inflow region along the northern boundary. As critical melt rates are relatively high there, efficient tidal mixing could support a stable tidal front. On the other hand, the velocity-independent parameterization does place high melt rates over the warm inflowing branch of the cavity circulation, but not over the plume area. Tidal mixing underneath the ice shelf in velocity-independent model is therefore expected at the location of strong outflow plumes. The very different locations of tidal mixing between the velocity-dependent and velocity-independent models could lead to large difference in the simulated distribution of melt rates and in the structure of the circulation in the cavity. This hypothesis can not be verified from the present 'warm' ice shelf experiments however. Another set of simulations forced with typical 'cold' ice shelf hydrographic and tidal forcing conditions would be necessary to do so.

Figure 57 shows the difference between the critical melt rate calculated using the baroclinic approach and the actual velocity-dependent melt rates under PIIS for simulations forced with a diurnal tidal signal of realistic amplitude. In this case, the barotropic (not shown) and baroclinic calculations produce overall similar distributions of m_{max}, to the exception of local maxima over strong plume outflows that are not captured by the barotropic approach. There are also no significant difference between simulations forced with semi-diurnal and diurnal tides.

In the velocity-independent experiments, the critical melt rates are less than the simulated melt rates everywhere underneath PIIS and that, for all values of efficiency coefficient α over the range [0.05% - 1.5%] (see figure 57a). This is also the case in the velocity-dependent experiments when the default value of drag coefficient is used (see figure 57b). The sensitivity experiments described in section 4.2 however suggest that the default C_d underestimates the melt rates underneath PIIS (Payne et al., 2007). Therefore we verify here if the formation of a tidal front is possible when employing a value of C_d such that the melting/refreezing rates are more representative of that observed under PIIS. A four-fold increase of the drag coefficient indicates that m_{max} becomes slightly larger than the actual melt rates over very restricted areas along the grounding line that are characterized by shallow waters and very small melt or refreezing rates, in particular over a

[21]This is the case for all efficiency and drag coefficients over the range of values investigated here.

shallow plateau at the southern edge of the cavity where we identified an important increase in melt rates when introducing tides. For a 16-fold increase, which is necessary to approximately match velocity-dependent and velocity-independent melt rates, m_{max} exceeds the melt rates over the interior of the shallow northeastern portion of the cavity also, suggesting that the formation of a tidal front could be possible there.

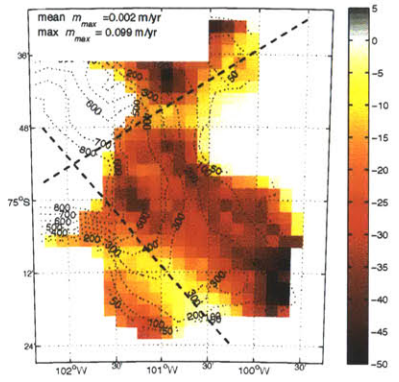

(a) velocity-independent $\gamma_{T,S}$

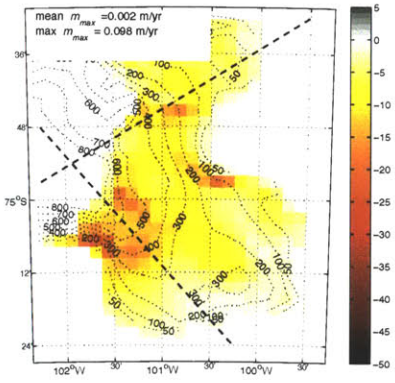

(b) vel-dep. $\gamma_{T,S}$, default C_d

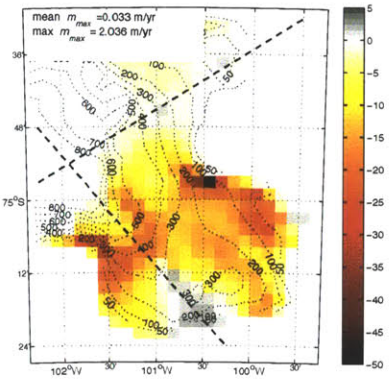

(c) vel-dep. $\gamma_{T,S}$, 4 × default C_d

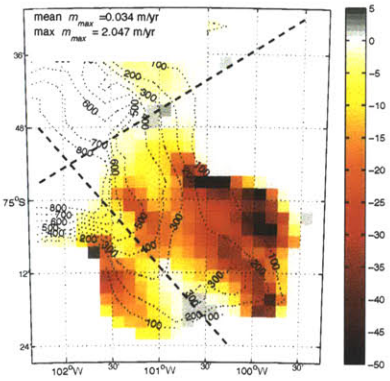

(d) vel-dep. $\gamma_{T,S}$, 16 × default C_d

Figure 57: Difference between the critical melt rate and the actual melt rate calculated in an idealized PIIS setup with (a) the velocity-independent model, (b) the velocity-dependent model and default drag coefficient, (c) the velocity-dependent model and C_d = 4 × default, (d) the velocity-dependent model and C_d = 16 × default. Domain-averaged and maximum calculated critical melt rates are indicated in the upper right corner of each graph. Dotted contours show the spatial distribution of water column thickness (m). The efficiency coefficient in all simulation is of 0.75%.

To verify if well mixed conditions do occur, we examine the hydrographic properties along two cross-sections indicated by the dashed lines on figure 57, which transects the areas over which m_{max} seems to exceed the melt rate in the simulation using C_d = 16 × default. Figures 58a, 58b and 58c show the potential temperature, salinity and potential density along the southern section that intercepts the shallow plateau at the southern edge of PIIS. All three fields indicate stably stratified conditions. Positive values in the difference m_{max} - m must therefore be attributed to the fact that melt rates are near-zero and even slightly negative over a few grid cells there. The brine rejection associated with this very slow refreezing might not be sufficient to overturn the water column. Figures 58d, 58e and 58f show the same hydrographic properties along the section that transects the shallow northeastern portion of the cavity and indicate a weak but stable stratification. We thus consider that the formation of a tidal front there is also unlikely. Hence the strong increase in melt rates observed over this mostly stagnant region (see figure 49) when including tides must be simply due to the fact that melt rates

are near-zero there in the unforced experiments, and slightly above zero in the tidally forced experiments. We therefore conclude that tidal front formation is likely not supported under PIIS because of its fast ablation rates which insure the maintenance of a stable stratification, in particular by promoting the formation of a thick film of light freshwater at the base of the ice shelf.

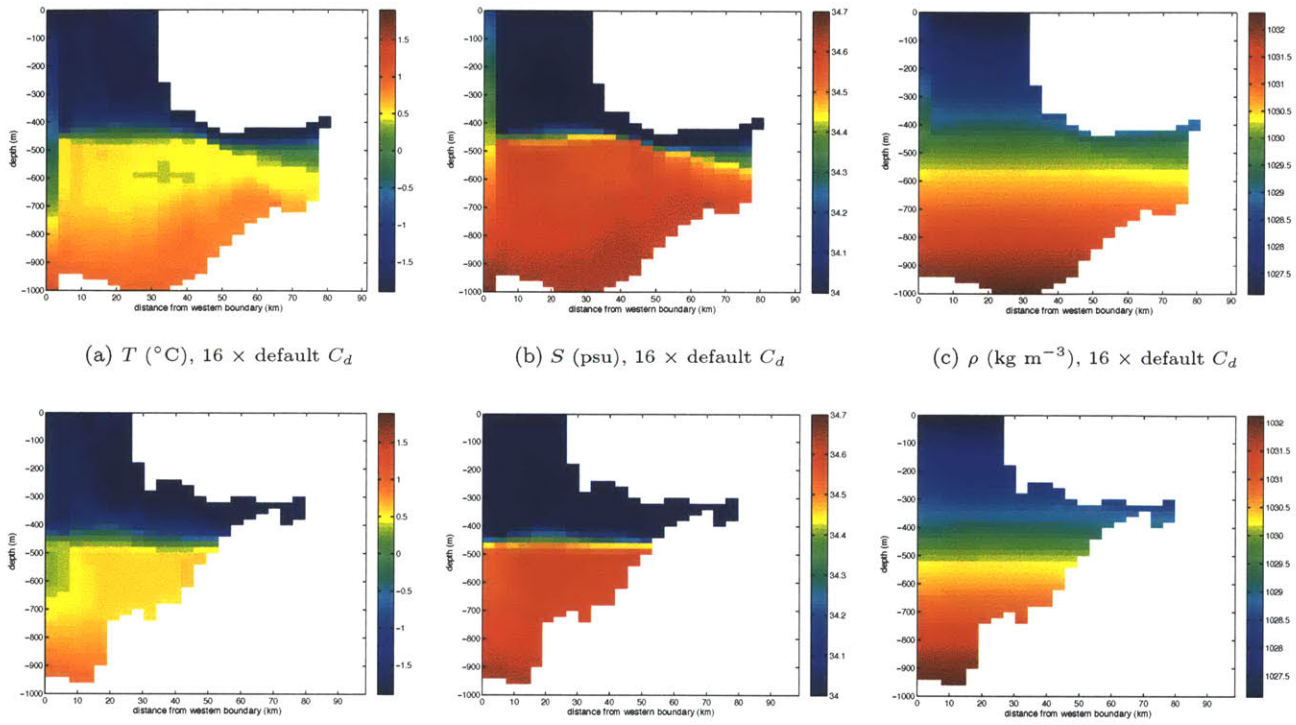

(a) T (°C), 16 × default C_d (b) S (psu), 16 × default C_d (c) ρ (kg m^{-3}), 16 × default C_d

(d) T (°C), 16 × default C_d (e) S (psu), 16 × default C_d (f) ρ (kg m^{-3}), 16 × default C_d

Figure 58: (a, d) Potential Temperature (b, e) salinity and (c, f) potential density simulated with the realistic velocity-dependent PIIS model using 16 × the default value of C_d and forced with diurnal tides. Upper panels show the hydrographic properties along the southern cross-section and lower panels, properties along the northern cross-section identified by the dashed black lines on figure 57.

At this point, one result is left unexplained by both tidal rectification and tidal mixing: it is the strong increase in melt rates along the northern wall of the idealized cavity and over a very thin band along the grounding line. Our earlier comparison of the critical melt rates and actual melt rates identified this area as the most likely location of tidal front formation under 'cold' ice shelf conditions, as velocity-dependent melt rates are relatively weak there. In the present 'warm' setup however, melt rates are well above critical melt rates over this region. A potential density cross-section along the northern cavity wall confirms that the water column is indeed well stratified (see figure 59f). However, the temperature profile is nearly homogeneous over a large region extending outward from the base of the ice shelf (figure 59d). Stable stratification is therefore ensured by the presence of a thin film of cold and fresh meltwater at the ice shelf base (see figure 59e). Another cross-section along the meridional mid-point of the cavity indicates similar but less extensive conditions close to the grounding line (figures 59a, 59b, 59c). These hydrographic profiles point to the mixed layer temperature averaging as the most probable cause of the important melt rate acceleration there. As temperature is much higher in the grid cell just below the one in direct contact with the ice shelf base, vertical averaging over a fixed-depth mixed layer allows to pick up the warm signal and artificially increase the temperature gradient across the boundary layer (i.e., $T_M - T_B$). This result therefore highlights the importance for a high vertical

resolution to accurately represent the mixed and boundary layers in presence of near-homogenization of the temperature below the ice shelf.

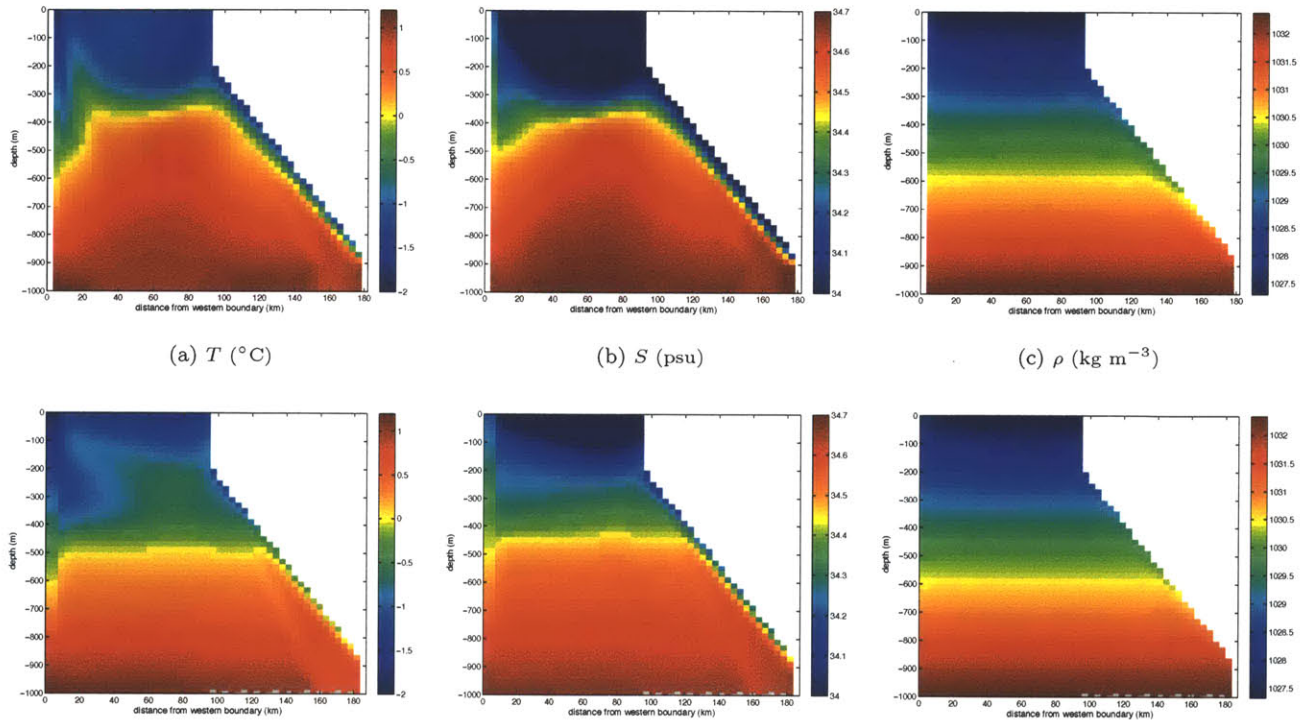

(a) T (°C) (b) S (psu) (c) ρ (kg m^{-3})

(d) T (°C) (e) S (psu) (f) ρ (kg m^{-3})

Figure 59: (a, d) Potential Temperature (b, e) salinity and (c, f) potential density simulated with the idealized velocity-dependent model forced with diurnal tides with amplitude $U_T = 0.2$ ms^{-1}. Upper panels show the hydrographic properties along a zonal cross-section at 75.0°S (mid-latitude of the cavity) and lower panels, properties along the northern cavity wall (at 74.55°S).

5 Conclusions

In this work, we have compared the melt rates and circulation simulated by a z-coordinates sub-ice shelf cavity model implemented in the MIT ocean general circulation model when using two different parameterizations of the turbulent heat and salt transfers at the ice shelf base. The first of these parameterizations is based on the work of Hellmer and Olbers (1989). It assigns constants values to the turbulent exchange velocities, $\gamma_{T,S}$, and hence implies constant ocean current speeds underneath the ice shelf. The second explicitly accounts for the turbulence generated by ocean currents at the ice interface and couples the turbulent exchange velocities with the mixed layer flow.

We first investigated the modulating impact of the introduction of the velocity-dependence on the melt rates and cavity circulation by comparing simulations using both the velocity-independent and velocity-dependent parameterizations of $\gamma_{T,S}$. In these simulations, no external tidal forcing was used and the model was forced at its open boundary by prescribed profiles of temperature, salinity and zonal currents typical of 'warm' ice shelves such as PIIS. Both an idealized ice shelf geometry and a realistic PIIS cavity were used. In a second time, we varied the drag coefficient over a wide range of values and examined the effect on melt rates and transports in both the idealized and realistic ice shelf cavities. In a third time, we varied the ice shelf base slope and the shape of the seabed independently in idealized simulations in order to observe and contrast the response of both the velocity-dependent and velocity-independent models to changes in cavity geometry. Finally, we investigated the temporal variability of the model's solution and the modulations of the time-independent cavity circulation and melt rates associated with the inclusion of prescribed time-varying tidal currents at the mouth of the cavity. In the idealized experiments, the behavior of the model's solution was compared between simulations using different amplitudes of tidal forcing at the diurnal and semi-diurnal frequencies. In the realistic cases, diurnal and semi-diurnal tidal forcings of amplitude representative of that under PIIS were used. In particular, the possibility for occurrence of tidal rectification and formation of a stable mixing front under PIIS was investigated. Table 2 summarizes the characteristics of all simulations performed. The main conclusions drawn from these experiments are the following :

- In our velocity-independent simulations, the circulation and melt rate distribution are in good agreement with the results of previous velocity-independent modeling studies, which place the fastest melting at the deepest reaches of the grounding line, where thermal forcing is highest.

- Our velocity-dependent simulations results are however very different from that of previous ice shelf-ocean modeling studies using a velocity-independent parameterization for the melt rates. The experiments performed here suggest that, under conditions of current velocities and thermal forcing typical of PIIS or 'warm' ice shelves, the turbulence induced by the proximity of a moving ocean to the fixed ice interface dominates over temperature gradients in setting the diffusive heat flux through the ice-ocean boundary layer and hence, the magnitude of ablation rates. In our velocity-dependent experiments, the regions of fastest melting coincide with strong outflow plumes and, to a lesser extent, to regions of strong inflowing currents. This is true over the whole range of values of drag coefficient used here ($\frac{1}{16}$ to 16 $\times$ the default value of $1.5 \cdot 10^{-3}$ proposed by Holland and Jenkins (1999)).

- Sensitivity experiments in which the drag coefficient is varied over a wide range of values indicate that the melt rate increases with C_d in a sub-linear manner. This behavior is observed in both the idealized and realistic PIIS experiments. In either case, no 'optimal' value of C_d is found beyond which melt rates decrease with increasing drag coefficient because of the deceleration of mixed layer currents by strengthened frictional drag at the ice shelf base. This could be explained by the presence of strong

buoyancy fluxes in our 'warm' ice shelf simulations, which dominate over frictional drag in setting mixed layer velocities when increasing C_d.

- The sensitivity experiments on the drag coefficient allow identifying two important feedbacks on the increase in ablation rates with C_d, in both the idealized and realistic PIIS ice shelf cavities. The simulations indicate a negative feedback due to the production of larger volumes of cold meltwater that spreads at the ice shelf base and insulates the ice interface from the warmer water below. This feedback is consistent with the results of previous observational studies (eg., Jacobs et al., 2011). We also observe a positive feedback associated with the acceleration of geostrophic mixed layer currents by increased buoyancy fluxes-induced density gradients underneath the ice shelf (Little et al., 2008) and with the strengthening of outflow plumes with the enhanced meltwater production. This second feedback will not be explicitly accounted for in velocity-independent ice shelf models.

- Comparison of velocity-independent simulations and velocity-dependent simulations in which the drag coefficient is varied indicates that a change in regime occurs when coupling the ablation rates to the velocity of ocean currents. In velocity-independent experiments, relatively fast mixed layer currents and low thermal forcing are simulated in the cavity. In velocity-dependent experiments, relatively slow mixed layer currents and high thermal forcing are obtained. Determining which regime is more representative of the conditions under PIIS and warm ice shelves in general would require comparisons of our model outputs with mixed layer velocities and thermal forcing estimates from observations.

- Idealized simulations in which the slope of the ice shelf base is varied suggest that steeper ice shelves support larger ablation rates and, because of the amplification of buoyancy-induced density gradients, stronger barotropic volume transports. This is in agreement with the results of previous studies Determann and Gerdes (1994); Grosfeld and Gerdes (1997); Holland et al. (2008); Little et al. (2008). Another set of idealized experiments in which the slope of the seabed is varied confirms the findings of Little et al. (2008) that it is not a dominant control of the depth-integrated volume transport in the cavity.

- No appreciable difference is observed between the response of the velocity-dependent and independent models to the variations of either the ice shelf base or bedrock slope in the present 'warm' cavity setup. More drastic changes in cavity geometry would perhaps be necessary to detect differences in the behavior of the two models. However, the simulation of such differences in models is complicated in the case of 'warm' relative to 'cold' ice shelf cavities because of the stronger stratification in ocean temperature, because a modification in the cavity geometry implies a change in water volume and so, of heat content in the cavity.

- When introducing a tidal forcing in the idealized and realistic experiments, the overall spatial distribution of melting remains relatively unchanged. In the idealized experiments, the magnitude of melt rates however increases when including tides, in agreement with the recent modeling work of Makinson et al. (2011). The increase in melt rates is noticeable for tidal forcing about one order of magnitude larger than that predicted for PIIS. In the realistic experiments, area-averaged melt rates do not increase significantly with the introduction of tides, since tidal currents are relatively weak under PIIS. Nonetheless, in both the idealized and realistic experiments, we observe large local increases of melt rates between the unforced and tidally forced simulations. The most important acceleration in melting is seen along the ice shelf front and is consistent with the generation of tidally-rectified currents there.

- The temporal variability of melt rates associated to tidal forcing is greater in the velocity-dependent than in the velocity-independent experiments. Velocity-independent melt rates vary in phase with thermal

forcing, which is highest at the end of the half period of inflow tides, i.e., of enhanced warm inflow at depth, and lowest at the end of the half period of outflow tides, i.e., of strongest outflow currents at the surface. Area-averaged velocity-dependent melt rates on the other hand vary approximately in phase with mixed layer currents, which are maximum both at the timing of maximum inflow and outflow tides. The response of thermal forcing, mixed layer velocity and melt rates are similar for both the diurnal and semi-diurnal tides and are also consistent between the idealized and realistic PIIS experiments.

- The velocity-independent melt rate varies approximately as a mono-periodic signal, consistently with the variability in thermal forcing. The velocity-dependent melt rates on the other hand show variability at higher frequencies, notably at half the tidal period. This is consistent with the generation of higher-harmonic tidal power by non-linear interactions such as advection and frictional drag. In the velocity-dependent model, ablation rates can respond directly to these higher frequency tidal currents because of the direct coupling of the mixed layer velocity and turbulent exchange coefficients. Fourier analysis of the area-averaged and maximum melt rates signals confirms this by indicating peak melt rates at multiples of the tidal forcing frequency. As the thermodynamics and dynamics components of the model are fully coupled, velocity-independent melt rates also respond to generation of tidal power at higher frequencies. However, the velocity-independent melt rate signals are much lower and decrease faster for higher harmonics compared to the velocity-dependent case. This is consistent with the idea that the variability of the model is increased when using a velocity-dependent instead of a velocity-independent melt rate parameterization (Jenkins et al., 2010b).

- Because tidal currents under PIIS are relatively weak, the displacement of individual water columns under tidal forcing (i.e., tidal excursion) is small and tidal rectification is expected only along topographic features with very short horizontal scales. Comparison of the distribution and strength of time-independent cavity currents obtained for unforced and tidally forced simulations indeed suggests that tidal rectification occurs along the ice shelf front of PIIS and perhaps locally along steep portions of the grounding line or cavity walls, but nowhere else in the cavity. In particular, tidal-rectification at the shelf front of PIIS induces strong along-ice edge barotropic currents that are not seen in unforced experiments. Such circulation is likely to increase the ventilation time of the cavity by inhibiting cross-ice edge flow, hence to reduce the sensitivity of melt rates under PIIS to offshore ocean warming. In the velocity-dependent experiments, these strong barotropic currents significantly increase the ablation rates at the ice shelf front and a positive feedback occurs between strengthened currents and accelerated melting. This feedback is not captured by the velocity-independent melt rate formulation.

- Estimations of the maximum melt rate for which tidally-induced turbulence can efficiently mix the water column suggest that the formation of a stable tidal front underneath PIIS is unlikely. Some homogenization of the ocean temperature in the cavity is observed when forcing the model with moderate to high tidal currents ($U_T = 0.2$ ms^{-1}). However, the water column is maintained stably stratified by the presence of a thin layer of freshwater at the ice shelf base, which is ensured by the relatively strong melting triggered by the high simulated thermal forcings. Hence, the present experiments support the hypothesis of Holland (2008) that tidal mixing should not be significant under 'warm' ice shelves.

In brief, the experiments performed allowed identifying important differences between the sensitivity of the velocity-dependent and velocity-independent ice shelf models which suggest that coupling the ablation rates directly to the ocean currents beneath the ice shelf critically impacts the distribution of melting and the structure and strength of the cavity circulation. Our results show that tides more strongly impact the cavity

dynamics and the time-variability of melt rates under warm ice shelves such as PIIS when a velocity-dependent formulation is used for the ablation rates.

Despite its higher level of complexity compared to the velocity-independent melt rate parameterization, the velocity-dependent formulation used here might still overlook important physical processes within 'warm' ice shelf cavities. In particular, parameterizing the stabilizing/destabilizing effect of the melting/refreezing-induced buoyancy fluxes on the boundary layer underneath the ice shelf could significantly impact the simulated melt rates. Holland and Jenkins (1999) compared melt rates computed with their parameterization of $\gamma_{T,S}$ when taking into account the effects of stabilizing/destabilizing buoyancy fluxes and when neglecting these effects by setting the stability parameter η_* to 1 in equation (16). As mentioned in section 3, they found that calculating η_* according to equation (16) changed the melt rates by less than 10% under 'moderate' conditions of friction velocity and thermal driving (see equation 33), which they identified as $u_* > 0.001$ ms^{-1} and $T_* < 0.5$°C. As indicated in figures 16b and 24b, the area-averaged friction velocity underneath both the idealized and realistic PIIS ice shelves is over 0.001 ms^{-1} for most values of drag coefficients used in this study. However, for all values of C_d employed here, the thermal driving is much larger than 0.5°C. This is probably the case also for other 'warm' ice shelves entering in contact with CDW (eg., Jacobs and Hellmer, 1996; Payne et al., 2007; Holland, 2008; Holland et al., 2008; Jenkins et al., 2010b). For these 'warm' ice shelves, refreezing is thought to be very limited (Jacobs and Hellmer, 1996). Hence setting η_* to 1 under refreezing conditions is likely to have little impact on the simulated phase change processes. However, the relatively large ablation rates and associated stabilizing buoyancy fluxes may significantly suppress mixing underneath the ice shelf and inhibit further melting. Holland and Jenkins (1999) mentioned that including the stability parameter into the formulations of the turbulent heat and salt exchange coefficients requires a computationally expensive iteration to calculate the melt rate and $\gamma_{T,S}$. However, the addition of this extra level of complexity may be necessary to allow obtaining accurate model estimates of melt rates underneath 'warm' ice shelves such as PIIS. This should be verified by comparing the present simulation results to experiments in which the parameterization of η_* would be included, in the context of both an idealized and a realistic 'warm' ice shelf cavity.

Another process that is not accounted for in the present velocity-dependent melt rate formulation is the entrainment of warm waters by the buoyant plume rising along the ice shelf base. Entrainment can impact the melt rates in at least two ways. First, as the ambient ocean is relatively warmer than the meltwater plume, entrainment raises the temperature of the plume and hence provides a heat source for melting (Holland and Feltham, 2006). Payne et al. (2007) applied the reduced gravity plume model of Holland and Feltham (2006) to a realistic PIIS cavity and showed that buoyant plumes are indeed primarily fed by entrainment of warm waters near the grounding line. Second, Holland and Feltham (2006) identified that the inclusion of entrainment decreases the relative importance of drag at the ice shelf base and therefore accelerates the plume. As the highest melt rates in our velocity-dependent model are collocated with the path of meltwater plumes, an increase in the speed of plume outflows would directly increase the maximum ablation rates. Neglecting entrainment on the other hand likely implies that our realistic simulations underestimates the melt rates under PIIS.

Many three-dimensional models applied to the study of ice shelf cavities do not parameterize entrainment (eg., Grosfeld and Gerdes, 1997; Little et al., 2008; Losch, 2008; Schodlock et al., 2012). On the other hand, reduced gravity plume models present the disadvantage of not accounting for the effects of depth-independent flows within the cavity (Holland and Feltham, 2006). Payne et al. (2007) justified their use of a plume model to simulate melt rates under PIIS by hypothesizing that the control of barotropic flows on the redistribution of melting in 'warm' ice shelf cavities might not be as important as in 'cold' and more weakly stratified cavities. The present experiments suggest however that the convergence of depth-independent currents along the steep

cavity wall sets the location of the outflow plumes under PIIS. Hence a logic continuation to the present study would be to include a parameterization of entrainment in our model. This would allow to make better assessments of the relative importance of the ocean circulation, tidal currents, thermal forcing and entrainment in determining the location and strength of melting under PIIS and to compare more efficiently the 'warm' and 'cold' ice shelf cavity regimes.

References

Adcroft, A., C. Hill, and J. Marshall, 1997: Representation of topography by shaved cells in a height coordinate ocean model. *Monthly Weather Review*, **125 (9)**.

Brink, K. H., 2011: Topographic rectification in a stratified ocean. *Journal of Marine Research*, **69**, 483–499.

CATS, 2012: CATS02.01: Circum-Antarctic Tidal Simulation, Forward Model. URL `http://www.esr.org/polar_tide_models/Model_CATS0201.html`, URL `http://www.esr.org/polar_tide_models/Model_CATS0201.html`.

Determann, J. M. and R. Gerdes, 1994: Melting and freezing beneath ice shelves: Implications from a three-dimensional ocean-circulation model. *Annals of Glaciology*, **20**, 413–419.

Eicken, H., H. Oerter, H. Miller, W. Graf, and J. Kipfstuhl, 1994: Textural characteristics and impurity content of meteoric and marine ice in the Ronne Ice Shelf, Antarctica. *Journal of Glaciology*, 386–398.

Grosfeld, K. and R. Gerdes, 1997: Thermohaline circulation and interaction between ice shelf cavities and the adjacent open ocean. *Journal of Geophysical Research*, **102 (C7)**.

Heimbach, P. and M. Losch, 2012: Ajoint sensitivities of sub-ice-shelf melt rates to ocean circulation under the Pine Island Ice Shelf, West Antarctica. *Annals of Glaciology*, **53 (60)**, doi:10.3189/2012/AoG60A025.

Hellmer, H. H. and D. J. Olbers, 1989: A two-dimensional model for the thermohaline circulation under an ice shelf. *Antarctic Science*, **1 (04)**, doi:10.1017/S095410208900490.

Holland, D. M. and A. Jenkins, 1999: Modeling thermodynamic ice-ocean interactions at the base of an ice shelf. *Journal of Physical Oceanography*, **29**.

Holland, D. M. and A. Jenkins, 2001: Adaptation of an isopycnic coordinate ocean model for the study of circulation beneath ice shelves. *Monthly Weather Review*, **129**.

Holland, P. R., 2008: A model of tidally dominated ocean processes near ice shelf grounding lines. *Journal of Geophysical Research*, **113**, doi:10.1029/2007JC004576.

Holland, P. R. and D. L. Feltham, 2006: The effects of rotation and ice shelf topography on frazil-laden ice shelf water plumes. *Journal of Physical Oceanography*, **36**.

Holland, P. R., A. Jenkins, and D. M. Holland, 2008: The response of ice shelf basal melting to variations in ocean temperature. *Journal of Climate*, doi:10.1175/2007JCLI1909.1.

Jacobs, S. S. and H. H. Hellmer, 1996: Antarctic ice sheet melting in the Southeast Pacific. *Geophysical Research Letters*, **23 (9)**, 957–960.

Jacobs, S. S., A. Jenkins, C. F. Giulivi, and P. Dutrieux, 2011: Stronger ocean circulation and increased melting under Pine Island Glacier ice shelf. *Nature*, **4**, doi:DOI:10.1038/NGEO1188.

Jenkins, A., 1991: A one-dimensional model of ice shelf-ocean interaction. *Journal of Geophysical Research*, **96**, 20 671–20 677.

Jenkins, A., P. Dutrieux, S. S. Jacobs, S. D. McPhail, J. R. Perrett, A. T. Webb, and D. White, 2010a: Observations beneath Pine Island Glacier in West Antarctica and implications for its retreat. *Nature Geoscience*, **3**, doi:10.1038/NGE0890.

Jenkins, A., K. W. Nicholls, and H. Corr, 2010b: Observation and parameterization of ablation at the base of Ronne Ice Shelf, Antarctica. *Journal of Physical Oceanography*, **40**, doi:10.1175/2010JPO4317.1.

Joughin, I., B. E. Smith, and D. M. Holland, 2010: Sensitivity of 21st century sea level to ocean-induced thinning of Pine Island Glacier, Antarctica. *Geophysical Research Letters*, **37**, doi:10.1029/2010GL044819.

King, M. A., L. Padman, K. Nicholls, P. J. Clarke, G. H. Gudmundsson, B. Kulessa, and A. Shepherd, 2011: Ocean tides in the Weddell Sea: New observations on the Filchner-Ronne and Larsen C ice shelves and model validation. *Journal of Geophysical Research*, **116**, doi:10.1029/2011JC006949.

Little, C. M., A. Gnanadesikan, and R. Hallberg, 2008: Large-scale oceanographic constraints on the distribution of melting and freezing under ice shelves. *Journal of Physical Oceanography*, **38**, doi:10.1175/2008JPO3928.1.

Losch, M., 2008: Modeling ice shelf cavities in a z coordinate ocean general circulation model. *Journal of Geophysical Research*, **113 (C08043)**, doi:10.1029/2007JC004368.

MacAyeal, D. R., 1984a: Numerical simulation of the Ross Sea tides. *Journal of Geophysical Research*, **89 (C1)**.

MacAyeal, D. R., 1984b: Thermohaline circulation below the Ross Ice Shelf: A consequence of tidally induced vertical mixing and basal melting. *Journal of Geophysical Research*, **89 (C1)**.

MacAyeal, D. R., 1984c: Tidal rectification below the Ross Ice Shelf, Antarctica. *Oceanology of the Antarctic continental shelf.*

MacAyeal, D. R., 1985: Evolution of tidally triggered meltwater plumes below ice shelves. *Oceanology of the Antarctic continental shelf.*

Makinson, K., P. R. Holland, A. Jenkins, and K. W. Nicholls, 2011: Influence of tides on melting and freezing beneath Filchner-Ronne Ice Shelf, Antarctica. *Geophysical Research Letters*, **38**, doi:10.1029/2010GL046462.

Makinson, K., M. A. King, K. W. Nicholls, and G. H. Gudmundsson, 2012: Diurnal and semidiurnal tide-induced lateral movement of Ronne Ice Shelf, Antarctica. *Geophysical Research Letters*, **39**, doi:10.1029/2012GL051636.

Marshall, J. A., A. Adcroft, C. Hill, L. Perelman, and C. Heisey, 1997: A finite-volume, incompressible Navier-Stokes model for studies of the ocean on parallel computers. *Journal of Geophysical Research*, **102 (C3)**.

McPhee, K. C., M. G. and J. H. Morison, 1999: Ocean heat flux in the central Weddell Sea during winter. *Journal of Physical Ooceanography*, **29**.

McPhee, M. G., 1981: An analytical similarity theory for the planetary boundary layer stabilized surface buoyancy. *Boundary-Layer Meteorology*, **21**.

McPhee, M. G., 1992: Turbulent heat flux in the upper ocean under sea ice. *Journal of Geophysical Research*, **97**, 5365–5379.

McPhee, M. G., G. A. Maykut, and J. H. Morison, 1987: Dynamics and thermodynamics of the ice/upper ocean system in the marginal ice zone of the Greenland Sea. *Journal of Geophysical Research*, **92**.

Mueller, R. D., L. Padman, M. S. Dinniman, S. Y. Erofeeva, H. A. Fricker, and M. A. King, 2012: Impact of tide-topography interactions on basal melting of Larsen C Ice Shelf, Antarctica. *Journal of Geophysical Research*, **117**, doi:10.1019/2011JC007263.

Padman, L., H. A. Fricker, R. Coleman, S. Howard, and L. Erofeeva, 2002: A new tide model for the Antarctic ice shelves and seas. *Annals of Glaciology*, **34**, 247–254.

Payne, A. J., P. R. Holland, A. P. Shepherd, I. C. Rutt, A. Jenkins, and I. Joughin, 2007: Numerical modeling of ocean-ice interactions under Pine Island Bay's ice shelf. *Journal of Geophysical Research*, **112**, doi:10.1019/2006JC003733.

Pritchard, H. D., S. R. M. Ligtenberg, H. A. Fricker, D. G. Vaughan, M. R. van den Broeke, and L. Padman, 2012: Antarctic ice-sheet loss driven by basal melting of ice shelves. *Letters to Nature*, **484 (502)**.

Ramming, H. G. and Z. Kowalik, 1980: Numerical modeling of marine hydrodynamics. *Applications to dynamics physical processes, Oceanographic series*, Vol. 26, Elsevier ed.

Rignot, E. and S. J. Stanley, 2002: Rapid bottom melting widespread near Antarctic Ice Sheet grounding lines. *Science*, **296**, doi:10.1126/science.1070942.

Robinson, I. S., 1981: Tidal vorticity and residual circulation. *Deep Sea Research*, **28A (3)**, 195–212.

Schodlock, M. P., D. Menemenlis, E. Rignot, and M. Studinger, 2012: Sensitivity of the ice-shelf/ocean system to the sub-ice-shelf cavity shape measured by NASA IceBridge in Pine Island Glacier, West Antarctica. *Annals of Glaciology*, **53 (60)**, doi:10.3189/2012AoG60A073.

Thoma, M., A. Jenkins, D. Holland, and S. Jacobs, 2008: Modelling Circumpolar Deep Water intrusions on the Amundsen Sea continental shelf, Antarctica. *Geophysical Research Letters*, **35**, doi:10.1029/2008GL034949.

Timmermann, R., et al., 2010: A consistent data set of Antarctic ice sheet topography, cavity geometry and global bathymetry. *Earth System Science Data*, **2**, doi:10.5194/essd-2-262-2010.

Walker, R. T. and D. M. Holland, 2007: A two-dimensional coupled model for ice shelf-ocean interaction. *Ocean Modelling*, **17**, 123–139.

Walters, R. A., 1986: A finite element model for tidal and residual circulation. *Communications in Applied Numerical Methods*, **2**, 393–398.

Walters, R. A., 1987: A model for tides and currents in the English Channel and southern North Sea. *Advanced Water Resources*, **10**, doi:0309-1708/87/030138-11.

Walters, R. A. and F. E. Werner, 1991: Nonlinear generation of overrides, compound tides, and residuals. *Tidal Hydrodynamics*, John Wiley and Sons, Bruce B. Parker ed.

Zimmerman, J. T. F., 1978: Topographic generation of residual circulation by oscillatory (tidal) currents. *Geophysical and Astrophysical Fluid Dynamics*, **11 (1)**, 35–47.

Zimmerman, J. T. F., 1981: Dynamics, diffusion and geomorphological significance of tidal residual eddies. *Nature*, **290**, 549–555.